Politecnico di Torino

POLITECNICO DI TORINO

Master's Degree in Biomedical Engineering

A.a. 2023/2024

Fiber-based triboelectric nanogenerators for energy harvesting applications

Supervisor:
Prof. Stefano Stassi

Candidate:
Mulè Alessia

SUMMARY

1 INTRODUCTION

1.1 MODERN ENERGY REQUIREMENTS

The technological progress has led to the massive spread of electronic devices such as household appliances, mobile phones, and wearable devices. These devices are powered by electricity, initially generated from fossil fuels, which have caused significant environmental consequences reflected in global warming and climate change. The need to reduce environmental impacts translates into an increased use of renewable energy sources, including solar and wind energy; however, these sources are dependent on weather variations and are characterized by intermittency. Therefore, adequate energy storage systems are needed to ensure the proper balance between supply and demand [1].

Another factor favoring the use of energy storage systems (ESS) is the high power (or voltage) demand over a short period due to the increasing functionalities of modern devices. The operating mechanism of ESS involves storing energy in forms other than electrical when production exceeds consumption, and then releasing it when necessary. This mechanism is typical of various types of commonly used batteries, such as smartphone batteries [2].

Today's easy access to the internet has led to a rapid increase in the development of the "Internet of Things (IoT)" over the last decade. This technology encompasses a wide range of applications, from smart homes to next-generation cars and everyday devices. The basic principle underlying it is that "if something can be connected to the internet, it will be connected," implying a connection between things and people. This results in increased energy consumption by these objects [3].

Another significant challenge in modern technology lies in the biomedical field; the use of sensors and wearable therapeutic devices requires a high and continuous power source to reduce or eliminate dependence on cables or charging stations. Analyzing the energy sources mentioned earlier highlights issues related to both renewable sources and battery presence. The main limitation of renewable sources in this case is the low output power generated due to their inherent intermittency; on the other hand, the implementation of rechargeable batteries faces two distinct problems. Their use is heavily dependent on the cognitive abilities of the patient and, simply put, their memory, as the device must be charged before the battery is exhausted. For the same reasons, the possibility of a replacement battery is excluded; particularly for elderly individuals, they may lack the capability or dexterity to proceed with the replacement [4].

Research attention should now focus on the development and optimization of particular devices able to collect and process different type of into electrical energy to recharge energy storage devices such as batteries or capacitors [5].

1.2 NANOGENERATORS "NGS"

The previously listed characteristics are addressed by a type of device still under development, nanogenerators "NGs", which are one of the main applications of flexible and stretchable electronics. Their small size and the choice of specific materials, characterized by good flexibility and mechanical stability, allow the creation of devices that can be modified in shape (stretched, bent) while still maintaining their electronic and structural properties [6]. In general, when we talk about an electrical generator, we refer to a device capable of generating electric charges, separating those with opposite signs, and using the potential generated by them to drive a flow of free electrons (an electrical current). The functioning of the generator is related to the use of electromagnetic, piezoelectric, pyroelectric, and electrostatic phenomena [7]. It was in 2006 that Wang's group introduced the use of NGs (nanogenerators) for the collection and conversion of mechanical energy into electrical energy by exploiting the piezoelectric properties of materials, and thus their ability to generate an electric polarization in response to external deformation in a reversible manner [8] [9].
The first definition of NG involved the use of a single ZnO nanowire activated by the tip of an atomic force microscope for the conversion of small amounts of mechanical energy into electrical energy. Over time, their definition has expanded to include any generator that, regardless of the presence of nanomaterials, uses Maxwell's displacement current as the driving force for conversion [10].

1.2.1 Operating mechanism

The structure of the NG (nanogenerator) consists of an insulating piezoelectric material placed between two electrodes, one on top and one on the bottom, which are connected to each other via an external load (Figure 1.1). The generation of a piezoelectric potential occurs in response to an external stimulus [11].

Let's consider an undisturbed state of rest. In this case, the anions and cations present on the two electrodes will be in equilibrium with each other, and there will be no flow of charges within the NG. When an external force is applied, the piezoelectric material generates the formation of electric charges of opposite signs in an amount directly proportional to the applied external pressure. The anions and cations then begin to flow and accumulate at the two ends of the material, forming electric dipoles, which in turn stimulate the formation of a piezoelectric potential. By connecting the circuit to external conductive wires, the flow of electrons in the external circuit is generated to restore the equilibrium that existed before the formation of the polarization charges. In this way, the application of force and the consequent mechanical deformation, followed by its release in a cyclic manner, allows for the generation of a steady current flow [12], [13].

1.2.2Origin of displacement current

If we consider Maxwell's equations, they are used to describe a time-invariant electromagnetic wave, as its interaction with the source remains constant. However, when discussing energy conversion phenomena, there is always an external mechanical stimulus that inevitably causes a disturbance in the shape or distribution of the dielectric medium.
The first case described is a representation of electromagnetism; the change in the dielectric, on the other hand, is due to piezoelectric and triboelectric effects, which will be analyzed in detail later and involve the presence of surface electrostatic charges.
Unlike generators based on electromagnetism, the optimization of the working conditions of an NG (nanogenerator) requires low-frequency conditions because it is characterized by high voltage and low current output [10].
A physical model to describe the behavior of nanogenerators was only associated in 2017 when the output current was linked to Maxwell's displacement current. We can define "J_D" as the displacement current density present within the dielectric medium as follows:

$$J_D = \frac{\partial D}{\partial t} = \varepsilon * \frac{\partial E}{\partial t} + \frac{\partial P_S}{\partial t} \tag{1.1}$$

Where:

$$D = \varepsilon E + P_s \tag{1.2}$$

Where D represents the displacement field; ε the permittivity of the medium; E the time-varying electric field; and P_s the polarization due to the presence of surface charges on the dielectric, caused by the piezoelectric or triboelectric effect. In detail, the first term of equation 1.1 refers to electromagnetic waves, while the contribution of the surface polarization in the second term is the very origin of nanogenerators, particularly piezoelectric ones, whose surface charge is generated following the application of mechanical deformation [14].
Usually, in an NG (nanogenerator), there is no application of an external electric field, so its contribution will be zero. As a result, the displacement current density J_D depends on the spontaneous polarization. Consequently, the output current of an NG coincides with the rate of change of the surface polarization charges [11].
The NG model is represented as a parallel-plate capacitor, and the output current is calculated as follows:

$$I_D = \int \boldsymbol{J}_D * d\boldsymbol{s} = \int \frac{\partial \boldsymbol{D}}{\partial t} * d\boldsymbol{s} = \frac{\partial}{\partial t} \int \nabla * \boldsymbol{D}\, d\boldsymbol{r} = \frac{\partial}{\partial t} \int \rho\, d\boldsymbol{r} = \frac{\partial Q}{\partial t} \tag{1.3}$$

where Q represents the total free charges on the electrode passing through the surface, J_D the displacement current density, I_D the displacement current, and ρ the charge density.
From equation 1.3 follows the prevalence of displacement current on NG's internal circuit while, on the external one, there is capacitive current contribution [10].

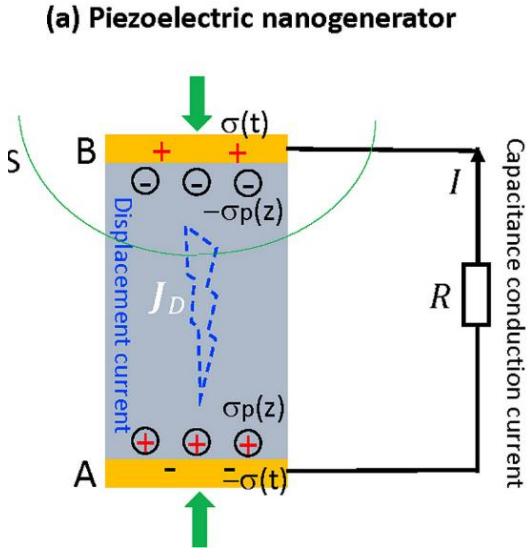

Figure 1.1 Outline of NG with a simple explanation about formation of J_D due to formation of surface charge density σ_t [10]

1.3 TRIBOELECTRIC NANOGENERATORS "TENGS"

1.3.1 Triboelectric effect

TENGs are mainly used for energy harvesting applications. The aim of these devices is to harvest mechanical energy generated from the application of a force or deformation and produce an electrical output [7].
The development and massive diffusion of TENGs in recent years has been driven by the triboelectric properties naturally present in most commonly used materials. Additionally, they are characterized by:

- Compact size
- High electrical power density
- Increased efficiency
- Low production costs
- Capability for low-frequency energy recovery

The advantages are often linked to the possibility, as mentioned earlier, of using a wide range of materials. Among these materials are flexible ones, making TENGs a good alternative as wearable devices [8].
TNEGs are characterised by a simple structure, and this makes it possible to achieve compact dimensions at low cost of production, as we can see in figure 1.2. Infact it consists of two layers of polymeric material with opposite triboelectric properties, meaning they are capable of attracting charges of opposite signs. These layers are covered on their external surfaces by dielectric metal layers and connected to an external circuit to ensure proper functioning [6]. It is important that the materials used are poorly conductive or, preferably, insulating, and that they have different nanometric surface roughness, so they can collect and retain the charges for a longer period of time [7], [15]. Moreover, a surface that is not perfectly smooth increases the friction area, allowing for the generation of a greater amount of surface charges [16].
Also for TENGs the displacement Maxwell's current has origin from the term "P_s" (equation 1.1) and, in this case, it occurs with opposite surface charge density after contact between materials.
The main way to generate electric energy is, infact, on the alternation of contact and separation of the two polymer plates, which simultaneously involves the phenomena of contact electrification and electrostatic induction (named also "triboelectricity").

In detail, we can talk about contact electrification if, after only contact between two different materials, they will no longer electrically neutral but will generate a surface charge. The development of triboelectric charge, instead, needs rubbing between this two materials. As a result, tribopairs will have opposite surface charges; the sign depends on the intrinsic properties of the materials which will be discussed later [17].
The connection between the metal electrodes and the external circuit, as shown in Figure 1.2, allows a flow of free electrons in response to the internal potential, which then results in an alternating current (AC) flow. Restoring the equilibrium, i.e., separating the two polymer plates, completes the current cycle [8].
The conversion of mechanical energy into electrical energy occurs through electrostatic induction, which in fact causes a variation in electrical potential through the application of mechanical deformation [7], [18].
Considering ε_1, ε_2 as the permittivities of the two dielectrics, and d_1, d_2 their thicknesses; with $\sigma_T\ (t)$ the triboelectric charge and $\sigma(z,t)$ the free electron density, we can define the electric field E that is generated on the surfaces of the dielectrics as follows [10]:

$$E_{z1} = -\frac{\sigma(z,t)}{\varepsilon_1} \tag{1.4}$$

$$E_{z2} = -\frac{\sigma(z,t)}{\varepsilon_2} \tag{1.5}$$

While, in the air gap between two electrodes E will be:

$$E_z = -\frac{\sigma(z,t) - \sigma_T}{\varepsilon_0} \tag{1.6}$$

Where ε_0 is permittivity of the free space, and it is egual to $8{,}854 * 10^{-12}\,\frac{F}{m}$.
The voltage between the two electrodes will be the sum of the three contributions of the electric field present, thus:

$$V = E_{z1}\,d_1 + E_{z2}\,d_2 + E_z z \tag{1.7}$$

TENGs are characterised by linear dependence between voltage, transferred charge and distance between tribocouples; define as $V - \sigma - z$ relation. For Contact-Separation mode (*C-S*) it is define as it follows:

$$V = -\sigma(z,t)\left(\frac{d_1}{\varepsilon_1} + \frac{d_2}{\varepsilon_2} + z(t)\right) + \frac{\sigma_T z}{\varepsilon_0} \tag{1.8}$$

Where $z(t)$ represents the distance between the two materials that varies with the application of an external stress.

In the operating case of TENGs, we are in short-circuit conditions, thus V=0 , and we can easily calculate the amount of charge transferred [19]:

$$\sigma(z,t) = \frac{z\sigma_T}{d_1\frac{\varepsilon_0}{\varepsilon_1}+d_2\frac{\varepsilon_0}{\varepsilon_2}+z} \tag{1.9}$$

By a simple first derivative we can obtain displacement current [14]:

$$J_D = \frac{\partial\sigma_T}{\partial t} = \sigma_T\left(\frac{dz}{dt}\right) * \frac{\left(d_1\frac{\varepsilon_0}{\varepsilon_1}+ d_2\frac{\varepsilon_0}{\varepsilon_2}\right)}{\left[d_1\frac{\varepsilon_0}{\varepsilon_1}+d_2\frac{\varepsilon_0}{\varepsilon_2}+z\right]^2} + \frac{d\sigma_T}{dt} * \frac{z}{d_1\frac{\varepsilon_0}{\varepsilon_1}+d_2\frac{\varepsilon_0}{\varepsilon_2}+z} \tag{1.10}$$

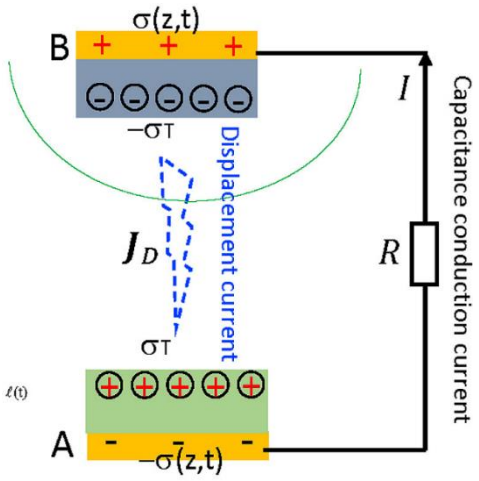

Figure 1. 2 Schematic work of contact-separation C-S TENG. It shows triboelectric opposite charge on both dielectric surfaces and induced charge on top of electrodes for formation of displacement current density J_D [10]

The actual formation of output current occurs in four distinct phases, described in figures 1.3 a and b. Due to the working mechanism of the TENG, the output consists in an alternating current J_D because of alternating contact and separation phases between two polymers.
First of all, it is necessary to distinguish between open-circuit and short-circuit conditions of the system.

In the first case, the electrons reorganize themselves to ensure a condition of equipotentiality between the electrode and its interface with the dielectric, in such a way as to have an open-circuit voltage (V_{OC}) equal to the difference between the potentials at the two interfaces, upper and lower. In the case of a short circuit, regardless of the distance at which the dielectrics are placed, there is always a flow of free charges in response to external deformation. In this case, we have zero voltage, as the two electrodes are at the same potential; in this case, we can calculate the short-circuit current (I_{SC}) as follows:

$$I_{SC} = A\frac{d\sigma}{dt} \tag{1.11}$$

A is the contact surface of triboelectric layers and $\frac{d\sigma}{dt}$ the short-circuit current density (J_{SC}) [20].

Analyzing the phases in detail, there is always an initial phase where there are no charges or electric potentials, and the two plates are at a distance z from each other (*Figure 1.3a I and Figure 1.3b I*). In open-circuit conditions (*Figure 1.3 a*), the surface charges generated at the contact zone of the two triboelectric layers, following the application of external pressure, remain confined to the surface because the materials used are dielectrics. As a result, they are on the same plane, canceling each other out, and thus unable to generate any potential difference at the interface *(Figure 1.3a II*). Once the force is released (*Figure 1.3a III*), the upper film tends to return to its initial position, leading to a gradual increase in the distance between the polymers. Assuming zero potential on the lower electrode, this creates a triboelectric potential difference on the upper electrode defined as:

$$V_{TE} = -\frac{\sigma z}{\varepsilon_0} \tag{1.12}$$

Where ε_0 is the permittivity constant of vacuum, z is the distance between the polymeric materials, and σ is the amount of induced charge deposited on the surface. As the distance between the polymers increases, there is a gradual increase in V_{OC} (*Figure 1.3a V, VI*) until it reaches its maximum value, and a gradual decrease as the distance z decreases [7], [15].

Remembering equation 1.8, this is the proof of linear dependence between voltage, transferred charges and distance between triboelectric places (*Figure 1.3a IV*) [21].

When the electrodes are in a short-circuit configuration, there is always the coexistence of potential generation associated with a charge flow to balance the system following the application of mechanical deformation (*Figure 1.3b*). The

direction of the transfer depends on the properties of the materials used, particularly their ability to attract or release electrons, expressed by what is called the 'triboelectric series,' which we will discuss later.
In the example of Figure 1.3, Kapton is placed on the upper electrode and PMMA on the lower electrode. The contact between the two materials generates a negative triboelectric charge accumulation at the upper interface and a positive charge at the lower interface *(Figure 1.3b II*). When the previously applied mechanical force is released, the materials separate, generating a potential that drives the flow of electrons from the upper electrode to the lower one, resulting in an accumulation of positive induced charges σ' on the Kapton and negative charges on the PMMA film (*Figure 1.3b III*), producing a peak of positive instantaneous current (*Figure 1.3b IV*). Equilibrium is restored when the distance between the two polymers increases to the initial value z. If the cycle is repeated, i.e., the two polymers are pressed together again, the electron flow starts in the opposite direction (*Figure 1.3 VI*). At this point, there is a gradual reduction of induced charges, generating a negative current peak (*Figure 1.3b IV*) until the initial equilibrium condition (*Figure 1.3b II*) is reached when the generator is fully released. At this point, the density of induced charge σ' will be equal to:

$$\sigma' = \frac{\sigma d' \varepsilon_K \varepsilon_P}{d_1 \varepsilon_P + d' \varepsilon_P \varepsilon_K + d_2 \varepsilon_K} \tag{1.13}$$

With σ as the triboelectric charge generated upon contact, d_1 , ε_K as the thickness and relative permittivity, respectively, of the Kapton film; d_2, ε_P as the thickness and relative permittivity of the PMMA film; and d' as the relative distance between the two materials. In Figure 1.3b VI, the moment when σ' reaches its maximum value ($d' = d_3$) is represented [15].
Current generates in external circuit generates from two different contributes:

$$I = C \frac{\partial V}{\partial t} + V \frac{\partial C}{\partial t} \tag{1.14}$$

With V as the voltage generated across the two electrodes and C as the system's capacitance. Specifically, the potential difference (the first term in equation 1.14) becomes part of the system when induced charges are generated. A variation in capacitance, on the other hand, occurs as a result of mechanical deformation. The formation of output current is ensured as long as there is a potential difference between the two electrodes, and this is generated by the triboelectric effect between the materials [7].

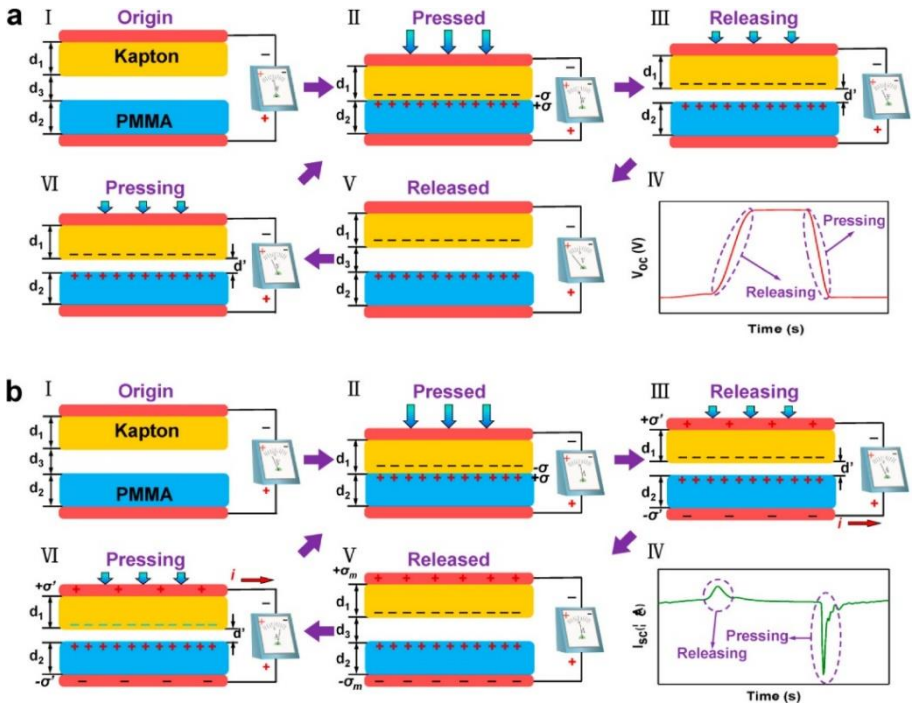

Figure 1. 3 TENG's operation cicle: (a) open circuit, (b) short circuit [15]

To better understand the origin of the triboelectric charge σ_T, from which the displacement current is generated, we need to refer to what 'triboelectricity' actually means. It basically consists of coupling of contact electrification and electrostatic induction and, as a consequence, surface charge generation [22]. For years, researchers have focused on the reasons why the triboelectric effect occurs and how, in detail, the actual formation of output current happens. The challenges in the research stem from various factors. For example, the triboelectric effect is difficult to standardize because it is present in materials in solid, liquid, and gaseous states. Another cause is the multitude of effects that come into play when two materials come into contact with each other. However, in 2012, with the invention of TENGs by Wang et al. research has sought to find answers to the four main questions which relate to the explanation of the triboelectric effect:

1. How the formation of triboelectric charge occurs
2. How this charge manage electron's flow (and Maxwell's displacement current)
3. How to quantify induced charge
4. How a TENG manages to fully harness this charge in terms of CA output

Among the various hypotheses developed over time, today the answer can be attributed to electron transfer during contact [23].
Recently, to provide a more detailed explanation of the CE effect and how the generation of opposite charges occurs on the two triboelectric surfaces, reference has been made to an electron cloud on an atomic scale. As we can see in figure 1.4, when the atoms of two materials are far apart, their electron clouds remain separate and do not overlap, with the electrons confined to their original orbits due to a strong energy barrier. When external mechanical forces push the two materials closer together, the atoms gradually approach each other until they reach a point where the electron clouds significantly overlap, greatly reducing the energy barrier between them. As a result, some electrons from material 1, which have higher energy, can easily overcome this lower barrier and transfer to material 2, allowing a new equilibrium to be reached. After the two materials separate, the transferred electrons and holes remain on the surfaces of the two materials, generating static charges on material 2 and material 1, respectively [24].

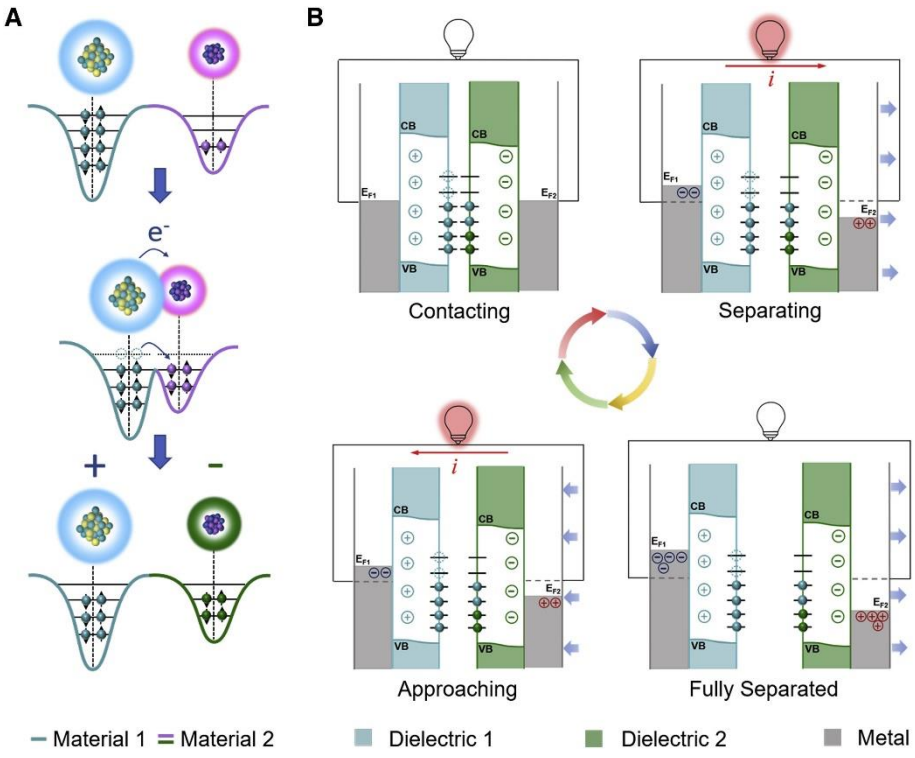

Figure 1.4 CE effect explanation. (a) at atomic level; (b) during TENG's cycle of operation [24]

1.3.2 Resistive and capacitive load connection

A standard measure of the output performance of TENGs is power ($\frac{W}{cm^2}$), the calculation of which depends on the resistive load (R) to which the TENG is connected [25]. In figure 1.5 *i* we can see the equivalent circuit of TENG connected to a resistive load. In particular, as R increases, the instantaneous power first increases and then decreases, as we can see in figure 1.5 *iii* [26].
This system is governed by Kirchhoff's law, as follows:

$$R\frac{dQ}{dt} = -\frac{1}{C_{TENG}}Q + V_{OC} \tag{1.20}$$

Through this model we can define three different TENGs "region of work" characterised by rising resistance values.
We can recognize this in figure 1.5 *ii*:

- Low R values (*Region I*) correspond to a charge transfer process similar with short circuits conditions and the maximum voltage is approximately proportional to the external resistance
- Medium range of resistences (*Region II*) presents the maximum output power value range; it matches to a reverse trend where the maximum current drops dramatically and the maximum voltage increases
- High resistence values, R higher than $1\ G\Omega$ (*Region III*) is characterized by open circuit similar conditions [18]

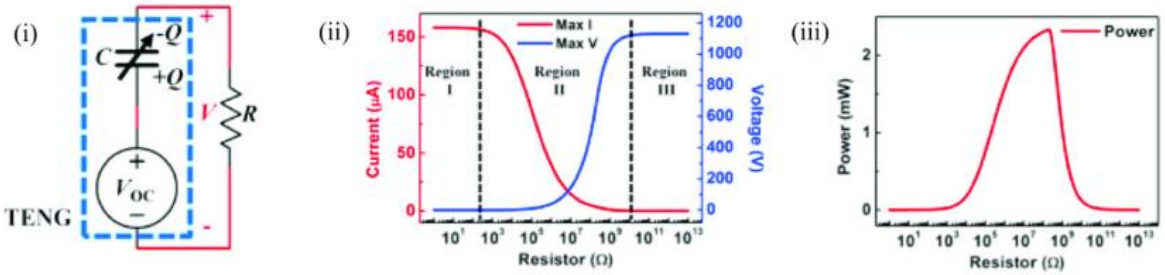

Figure 1. 5: (i) equivalent circuit of TENG with resistive load connection; (ii) TENGs "region of works" with output current and voltage values; (iii)power output [27]

In case of capacitive load connection, the equation governing the entire system is:

$$V = -\frac{Q}{C_T} + V_{oc} = \frac{1}{C_L} Q_C \tag{1.21}$$

where C_T is the internal TENG capacity and C_L the external circuit capacity.
Figure 1.6 shows equivalent circuit and output values in presence of capacity laod. As we can see in figure 1.6 *ii*, current and voltage have an opposite trend related to the three "regions of work "when they are connected to a capacitor. To identify the maximum output energy value we have to see figure 1.6 iii. The peak of energy appears when $C_T = C_L$ [27].

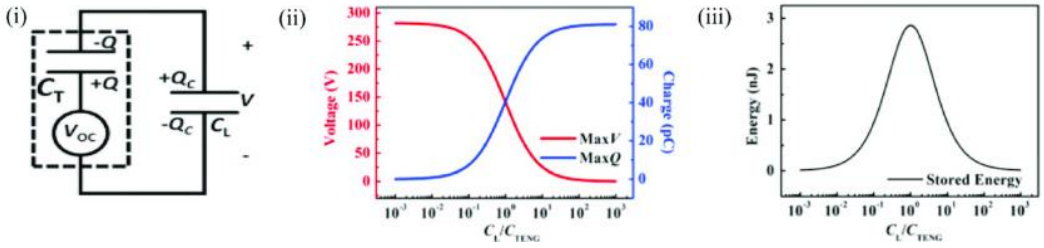

Figure 1. 6 (i) equivalent circuit of a TENG with a capacitive load connection; (ii) current and voltage output values related to the ratio between C_L and C_T; (iii) energy output values related to the same ratio [27].

1.3.3 Triboelectric series

Triboelectric effect is, probably, the most common effect in the world and also, triboelectric properties are present in a wide variety of materials, in solid, liquid, and gaseous states.
As mentioned earlier, it is important that the materials making up a TENG are different from each other. The choice of materials primarily depends on their electron affinity, which is the ability of individual materials to attract or donate electrons. This is due to the fact that the output power of the nanogenerator is proportional to the amount of charge transferred following the application of a force, but the triboelectric charges generated at the interface, in turn, depend on the difference in electron affinity between the two materials. In fact, if the materials have equal, or similar, electron affinity transferred charge will be zero

due to the absence of a potential that would lead to the generation of electron flow [24].
The ability of a material to lose or acquire electrons, at a qualitative level, is expressed in what is called the “triboelectric series” or scale. It is essentially a list of materials ranked based on their effectiveness in facilitating charge transfer and on the polarity that every material assume after contact [28].
Initially, it was introduced to minimize the negative effects of static energy accumulation (such as device failures) so in order to prefer materials with minimal static charge formation. Over the last years, after TENGs development, the triboelectric series has taken on a positive note; it has been observed that this electrostatic charge can efficiently convert mechanical energy into electrical energy. In this context, for the full maximization of output, it is beneficial to choose materials that are very far apart from each other in the triboelectric series [29].
However, what has not yet been found is a standard to measure the contact charge in a definitive way that could allows the universalization of materials ranking in the triboelectric series. The main reason is the numerous effects that influence CE, such as the type of contact, in terms of pressure and approach, the intrinsic or morphological properties of the materials, and external factors such as temperature and humidity [28]. So, in the literature we can found various triboelectric series that differ in terms of types of materials included (only polymers, metals), procedure to obtain electron affinity and, as a consequence, differences about materials ranking.
In figure 1.5 we can observe a triboelectric series based on the quantification of the triboelectric charge generated when a material comes into contact with a liquid metal. A solid material, unlike a liquid, does not guarantee reliable results for various reasons. Firstly, the surface roughness typical of solid materials does not ensure proper and repeatable adhesion at the point of contact; the properties vary from material to material, affecting the contact pressure. In this case, liquid mercury was used. As a liquid, it is not deformed upon contact, and the contact area is maximized because liquids adapt to shapes. The choice of mercury is convenient due to its "heaviness" and high surface tension, which prevents absorption when in contact with solid materials [29].
In figure 1.6 there is a collection of materials most frequently employed in the field of energy harvesting [30].

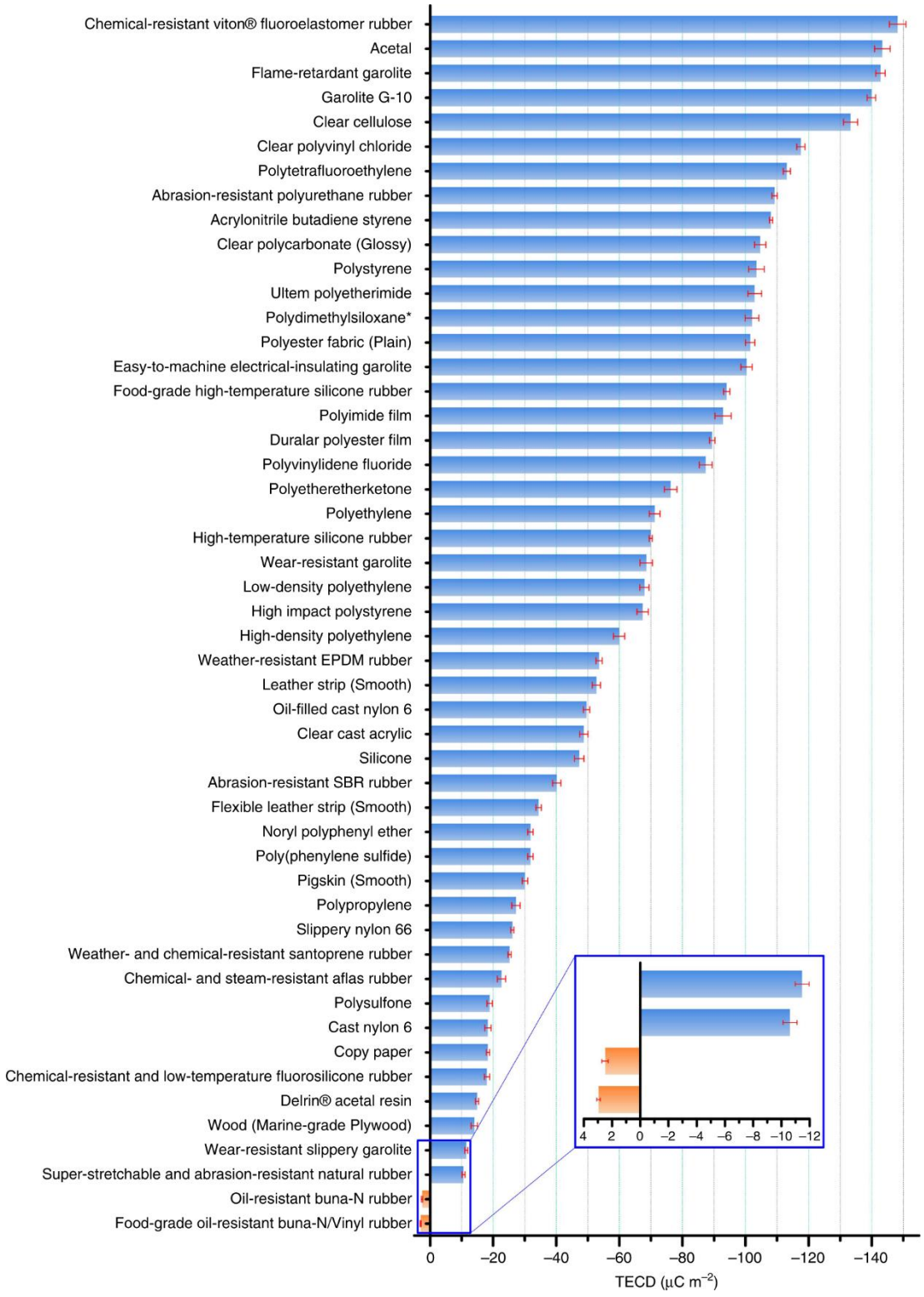

Figure 1. 5 Triboelectric series with materials ordered according to their triboelectric charge measured in TENG C-S mode relative to liquid mercury. The materials range from the most tribonegative at the top to the most tribopositive at the bottom [29]

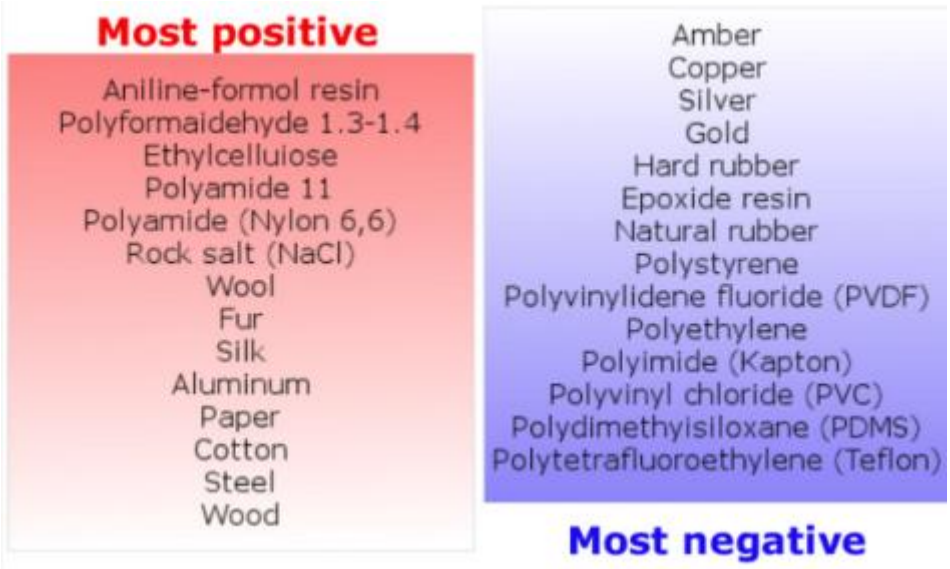

Figure 1.6 Another version of triboelectric series made by select group of materials typically most used [30]

Through triboelectric series, surface charge density (σ) is define as useful parameter in order to achieve a good optimization of output values. Other typical characteristics of materials that influence current flow generation are:

1. Friction coefficient (μ)
2. Polarization coefficient (P)

In particular, P and σ have an important role in terms of energy conversion efficiency.
Friction comes into play when materials come into contact and undergo rubbing; for this reason, it is important to keep it below a certain threshold, set at around -40, to reduce surface wear. The effect of a polarization coefficient outside the range of $0{,}05\,\frac{\mu W}{cm^2}$ to $0{,}5\,\frac{\mu W}{cm^2}$ results in a reduction of the device's short-circuit outputs [31].

The improvement of TENG output performance is closely linked to the choice of materials and the implementation of certain modifications at the nanometric scale which can be:

1. Physical
2. Chemical
3. Biological

4. Hybrid

In particular, we refer to physical modification when aiming to alter the morphology, introducing surface roughness or stimulating the formation of a higher surface charge density (for example, using laser treatment). On a chemical level, we address the material's ability to donate or accept electrons, and modifications can be made by introducing specific functional groups. Biological modification focuses on the use of biomaterials, found in the triboelectric series, and besides improving performance, it opens the door for TENG devices to be implantable biocompatible devices. Finally, hybrid modification results from a combination of the previous methods and is currently the most effective approach.

1.3.4 TENGs work modes

One of the key features of TENGs lies in their versatility of use. The output is always generated by a combination of contact electrification and electrostatic induction, but by varying the orientation of the charges and the position of the electrodes, we have the ability to harvest energy from various sources and utilize it for a wide range of applications [16].

We can list up to four different working modes, as we can see in figure 1.7:

a. Contact-separation mode (CS)
b. Lateral sliding mode (LS)
c. Single-electrode mode (SEC)
d. Freestanding triboelectric-layer mode (SFT) [8], [32]

CS mode (*figure 1.7 a*) is the first functional model of a TENG ever created, and over the years it has undergone continuous improvements in terms of friction generated upon contact and geometry. This has led to an increase in output voltage and power ($\frac{W}{cm^2}$) values, allowing for a wide range of applications, also due to its simple geometry [8], [16]. It utilizes the relative perpendicular movement to the interface for the generation of surface charges; it is during the separation phase that the actual generation of the electron flow occurs [33].
In the lateral sliding mode (*figure 1.7 b*) we have the parallel movement and it utilizes the external circuit for current generation. It also allows the harvesting of rotational energy, but the main challenges encountered with this mode of operation primarily concern the device's durability. The triboelectric pairs are in continuous contact with each other and are thus subjected to high surface friction [16][33].

The single-electrode mode is illustrated in *figure 1.7 c*. It features a lower electrode connected to the ground and a mobile layer, which can operate in both vertical contact mode and lateral sliding mode, offering greater versatility and improving the potential for TENG integration in wearable devices [8]. The cyclic movement of the mobile layer, either vertically or horizontally, induces a variation in the local distribution of the electric field; to balance this potential difference, a flow of electrons is created between the lower electrode and the ground to which it is connected [15].
A similar concept applies to the TENG in free-standing triboelectric layer mode (*Figure 1.4 d*). In this case, the structure has two electrodes that are symmetrically positioned, with a triboelectric layer placed on top but not connected to them. The charge distribution develops in the air gap between the dielectric and the two electrodes, driven by the relative movement of the triboelectric material with respect to the two electrode [34].

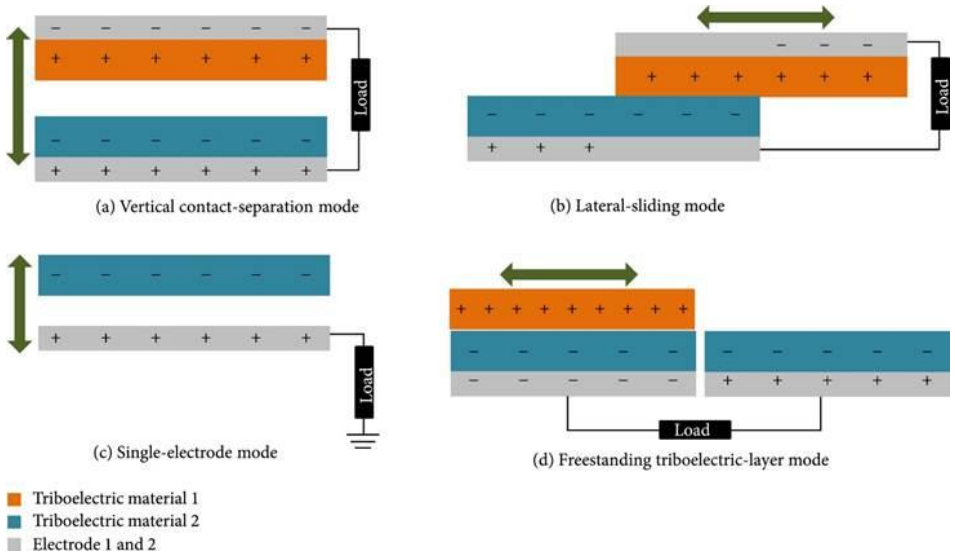

Figure 1. 7 Four operation mode of TENGs': (a) Vertical Contact-Separation mode; (b) Lateral-sliding mode; (c) single electrode mode; (d) Freestanding triboelectric-layer mode [32]

1.3.5 Figure of merits

As we can see, for the implementation and fabrication of TENGs the choice of materials, potential surface modifications to be implemented, and the selection of the configuration for materials and electrodes are key factors. To estimate how TENG performance changes based on these parameters, figures of merit (FOM_p) have been introduced :

- Structural FOM (FOM_S), that is adimensional and involves the four previously discussed modes operation and other possible hybrid combinations. It includes also the possibility of connecting the TENG to a charging circuit (FOM_C)
- Material FOM (FOM_M)

From equation 1.13, we can see that the maximum possible charge is obtained under short-circuit conditions, while the maximum voltage is achieved under open-circuit conditions. These cycles are referred to as the *'cycles for maximized energy output'* (CMEO), which correspond to the maximum stored energy, E_{max}. It is here that we can calculate the structural FOM. It is different from the E_m^C obtained from external capacitor, in particular E_{max} is the maximum absolute value of stored energy attainable.
We can calculate E_{max} as follows:

$$E_{max} = \frac{1}{2}\,\sigma_{SCmax}(V_{OCmax} + V'_{max}) \tag{1.15}$$

We can define σ_{SCmax} as the maximum charge transferred in a short circuit, V_{OCmax} the open circuit maximum voltage and V'_{max} the maximum absolute voltage achievable under short-circuit conditions.
The FOM_S turns out:

$$FOM_S = \frac{2\varepsilon_0}{\sigma^2}\frac{E_{max}}{Ax} \tag{1.16}$$

Where ε_0 is vacuum permittivity, σ charge surface density, A the area of the tribo-charged surfaces and x the maximum relative distance.
So, FOM_S is an universal standart to misure TENGs performances about structural design. To calculate a FOM value independent of the operating mode and size of the TENG, we need to introduce the performance FOM (FOM_p):

$$FOM_p = 2\varepsilon_0\frac{E_{max}}{Ax} \tag{1.17}$$

The structural FOM concerning the charging circuit can thus be expressed as:

$$FOM_C = \frac{2\varepsilon_0}{\sigma^2}\frac{E_m^C}{kAx} \tag{1.18}$$

In this case, E_m^C represents the energy stored in the external capacitor during the final cycle k.
At this point, we can define the materials FOM as:

$$FOM_M = \sigma^2 \tag{1.19}$$

because the amount of charge generated is the only term in the equation that depends on chosen materials [25], [35].
Considering A and σ equal for all possible configurations of the TENG, in figure 1.8 we can see the maximum structural FOM in descending order from left to right [25].
The CFT structure consists of two tribopairs so, trasferred charge is major than other structures and it results in the highest FOM_S. In general, a TENG operating in contact separation mode has a greater FOM_S compared to those with lateral sliding.
Minimun FOM_S appears in SEC mode due to the presence of a single electrode that inevitably leads to reduced output [36].

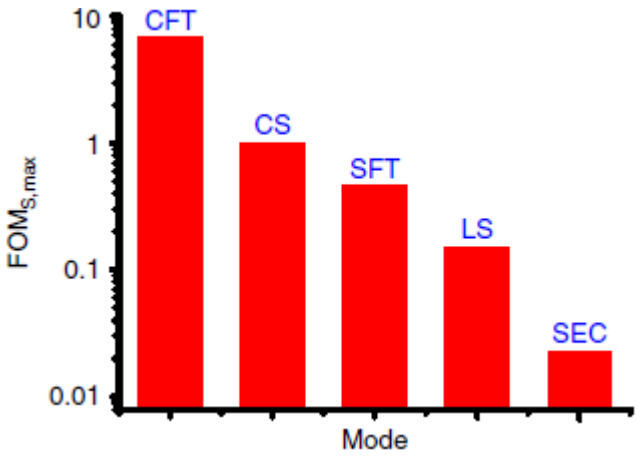

Figure 1. 8 FOM_S maximum values for different TENGs structures [25].

1.3.6 Fiber based TENG

The introduction of fibrous materials as tribo-pairs leads to an increase in the performance of the TENG in terms of higher charge density generated upon contact.
As previously mentioned, there is an improvement in output values when the surfaces of the tribo-pairs are not perfectly smooth, and potential surface modifications have indeed been identified. However, these modifications are often difficult to implement and involve high costs.
A new form of development in this direction is provided by the use of electrospinning processes, which, in a simple and economical way, allow for the production of nanofibrous membranes. Fibrous membranes, by definition, are characterized by intrinsic roughness and a high available surface area [37]. Furthermore, the presence of fibers provides an improvement in terms of flexibility, lightweight, resistance to applied force, and in wearable applications [38].
Among the materials that can be processed in fiber form, those most commonly used for TENGs are PVDF, its copolymers and PDMS.
PVDF is a particularly advantageous material because it is polymorphic and exhibits a β phase characterized by high polarizability and dielectric properties. The amount of β phase increases within the structure when PVDF is processed through electrospinning, leading to an enhancement of the piezoelectric and triboelectric properties of the material, which translates into improved TENG performance [39].
The following table (*table 1*) shows a comparison of output performance comparison of various PVDF-TENG devices with variable materials.

PVDF-	POWER ($\frac{\mu W}{cm^2}$)	VOLTAGE (V)	CURRENT(μA)	REFERENCE
COPPER	28.67	86	3.68	[40]
PA FIBERS	6.15	14.2	3.9	[41]
PAPER	0.2	1	0.2	[42]
PDMS	38.5	107	0.88	[43]
PET	18.45	44.15	8.36	[44]
PTFE	6.4	98	1	[45]

Table 1. 1 Comparison of TENG's output

2 MATERIALS AND METHODS

2.1 PVDF FIBERS

The main material exploited in this work is PVDF (*Polyvinylidene fluoride*) in form of fibers. PVDF is a non-reactive material with both dielectric and piezoelectric properties. The induced charge during the contact electrification mechanism depends on these two types of properties. A high dielectric constant value provides a better ability to retain surface charges, leading to an overall increase in output power. We also know that materials used in TENGs have their own tribopolarity; to regulate it, the intrinsic piezoelectric properties typical of certain materials are required [46].
An important characteristic of PVDF is that it is polymorphic; its structure is formed by the repetition of CH_2-CF_2 monomers, crystallized in four possible conformations called phases α, β, γ, and δ [47]. Among these, the β phase is characterized by a higher dipole moment and thus best piezoelectric properties, which also facilitates charge transfer during triboelectrification [48]. This is due to the presence of flourine and hydrogen structures, positive and negative respectively and in opposite directions [49].
Based on triboelectric series (*figure 1.6*) PVDF is a negative tribomaterial, so negative charges are transferred to PVDF fibers during the process.

2.1.1 Electrospinning technique

Electrospinning technique involves electrostatic forces in order to obtain fine fibers. In particular, through high potential electric field a polymer solution could be spun into nanometric diameter fibers (about hundreds of nanometres) with large surface areas [50].
It is a simple technique with an easy set-up (*figure 2.1*) and low costs of productions [51].
The structure consists of high-voltage power source, syringe pump with tubes or capillaries for the solution to pass through, and a conductive collector where the extruded solution will impact. The collector influences the morphology of the obtained fibers; if a rotating collector is used, the fibers will be oriented in a preferred direction; otherwise, with a flat collector, fibers will be random.
In brief, the polymer solution to be spun is driven by a syringe pump, creating a droplet of polymer at the end of the capillary. An inserted electrode permits the

application of high voltage on polymeric solution in order to generate free charges into solution. These charged ions are drawn by the electric field toward the electrode of opposite polarity, exerting tensile forces on the liquid polymer. At the capillary tip, the droplet elongates into a cone shape under the influence of the electric field. When the applied voltage reaches a critical level sufficient to overcome the liquid's surface tension, a fine jet of liquid is expelled from the cone's tip [50].

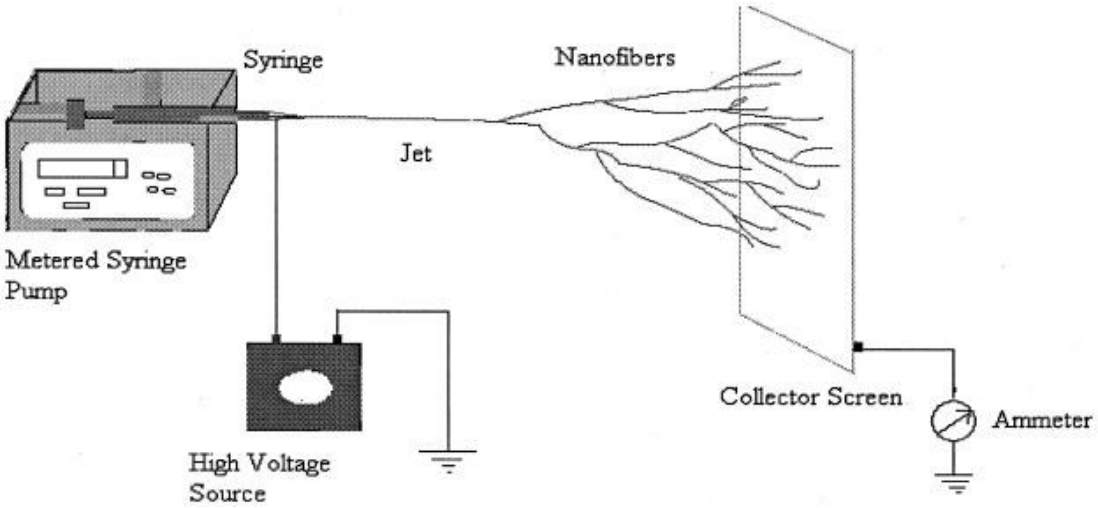

Figure 2. 1 Electrospinning set up scheme [50]

2.1.2 PVDF samples

In this work, five different samples of PVDF fibers deposited on a copper conductive collector were tested. Two of these were obtained with a rotating collector, resulting in an oriented morphology, with deposition times of 1 and 3 hours, respectively, producing the following thicknesses (micrometers) varying along the width of the fibrous membrane:

- Sample 1 (*s1*) with thickness from 30 µm to 70 µm
- Sample 2 (*s3*) thickness go from 50 µm to 120 µm

Other three samples have random orientation obtained by 1, 3 and 5 hours of deposition, respectively, with the following thickness:

- Sample 1 random (*s1_random*) from 20 μm to 50 μm
- Sample 2 random (*s3_random*) from 40 μm to 140 μm
- Sample 3 random (s5_random) about 200 μm

The first two reach maximum thickness in the middle section. As expected, there is a greater accumulation of fibers in the central area and greater inhomogeneity at the edges due to the lower intensity and nonlinearity of the electric field in those regions.

The 5 hours deposition sample has a very uneven thickness; the maximum thickness was obtained in the initial outermost region. This could be due to the saturation experienced by the collector because of the long deposition time.

The next step involves the construction of actual durable membranes for triboelectric characterization, which will be explained later. For all types of deposition listed previously, the fibers were deposited on alumium, first, and copper after, and samples with an active area of 3x3 cm^2 were prepared.

2.2 ARAMID FIBERS

Aramid fibers (AF) are characterized by a high specific surface area, high strength and good strength retention. They,also, exhibit good mechanical properties, thermal stability due to hydrogen bonds present in their structure, and structural regularity [52].

Aramid is synthesized based on a polycondensation reaction between the amine group ($-NH_2$) and the acid chloride group ($-COCl$), resulting in the formation of the amide group ($-NH-CO-$) and HCl.

We can distinguish between “meta” aramid fibers and “para” aramid fibers (also called *Kevlar*). Their chemical structure (*figure 2.2*) consists primarily of amide bonds and, to a lesser extent, aromatic rings connected on both sides of the amide bonds [53].

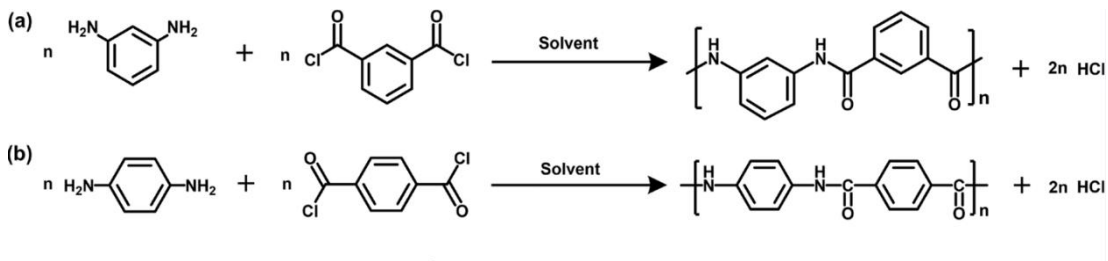

Figure 2. 2 Chemical syntesis of: (a) meta-AF; (b) para-AF [53]

An optimal solvent for aramid, in para and meta conformations, is DMSO. So, formulation of aramid nanofibers (ANF) solution involves DMSO and KOH. Both para and meta solutions were obtained with a concentration of $2\ \frac{mg}{ml}$.

In *p-ANF* we have:

- 500 mg of Kevlar fibers
- 251 ml of DMSO
- 751.37 mg of KOH

Fibers are yellow (*figure 2.3a*) and the solution color turns a sort of light red (*figure 2.3b*).

For *m-ANF* solution we use:

- 500 mg of meta fibers
- 250 ml of DMSO
- 751.23 mg of KOH

These fibers are white (*figure 2.3c)* and solution appears light yellow (*figure 2.3d*). The introduction of KOH in the formulation improve the solubility of aramid fibers and facilitate their dissolution in DMSO.

In both cases, the dissolution of the solution components occurred on a stirrer and temperature sets to 60°C for a couple of days.

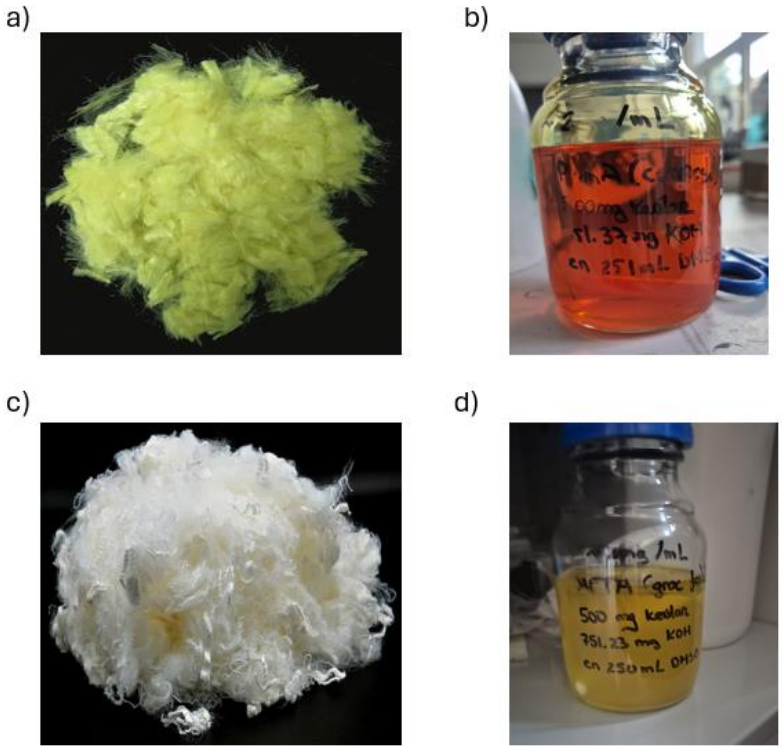

Figure 2.3 Aramid nanofibers and solutions used for triboelectric characterizations: a) p-ANF morphology; b) p-ANF solution; c) m-ANF morphology; d) m-ANF solution

2.2.1 Aramid samples

In order to test aramid triboelectric properties, three different ways of deposition were tested: dip coating, spray coating and filtration. The substrate for all the aramid samples is a thick sheet of Copper-Kapton with fibers deposition on conductive copper. The depositions were carried out under a fume hood. Considering that the triboelectric performance depends on the contact area, the aramid samples, like the PVDF ones, also have a surface area of 3x3 cm^2.

2.2.2 Dip coating

To promote the effective deposition of fibers on the sample, various approaches were attempted. First, 50 ml were separated from both meta and para aramide fibers solutions and placed in a small beaker to immerse the various samples. Several attempts were made to determine an optimal immersion time.
We start with a 1 minute of immersion for each sample. To improve and speed up DMSO evaporation samples were put on a stirrer set on 60° for about half an hour. Once the samples were dry, further immersions were carried out to allow a final comparison of the amount of fiber deposited on samples immersed 1, 2, and 3 times, respectively keeping the sample immersed in the solution for 1 minute. The same protocol has been performed with a square of micrometric aluminum grid.
Second attemp was carried out by increasing the immersion time to 5 minutes for for the two different solutions, obtaining a total of 6 samples.
And, at last, two samples were kept immersed overnight.

2.2.3 Spray coating

For ANF deposition starting from a liquid solution was used an air-brush spray coater (*figure 2.4*).

It consists of:

- A small reservoir where, through a small 1 ml capacity pipette, fibers solutions are inserted to be subsequently sprayed onto the copper sample
- Trigger on the central upper part to control the amount of liquid sprayer
- Main body where air and solution mixed up to create the spray

- Spray nozzle to produce uniform and fine flow
- Air connector that consists in a valve connected to a flexible hose in order to provide compressed air and improve solution spray

Samples are obtained with 1 and 2 ml of p-ANF and m-ANF. Before proceeding with the second coating, the samples were left to dry under a hood on a stirrer at 60°C.

Figure 2.4 Air-brush spray coater set-up

2.2.4 Filtration

In this case substrate was a micrometric membrane of PTFE metallized with thin layer of platinum.
The membrane is placed on a specific filtration apparatus under a fume hood, connected to a pump to create a vacuum. We used a WHATMAN glass vacuum filtration device (*figure 2.5*).
The total amount of meta and para solutions that were filtered to retain the fibers on the membranes is 10 ml. Before proceeding with the triboelectric characterizations, the membranes thus obtained were placed on a conductive sheet of copper-Kapton.

Figure 2.5 Filtration glass vacuum device. The white tube on the rigth allows connection to the pump to create vacuum.

In figure 2.6 we can see how aramid samples, obtained in three different ways, appear.

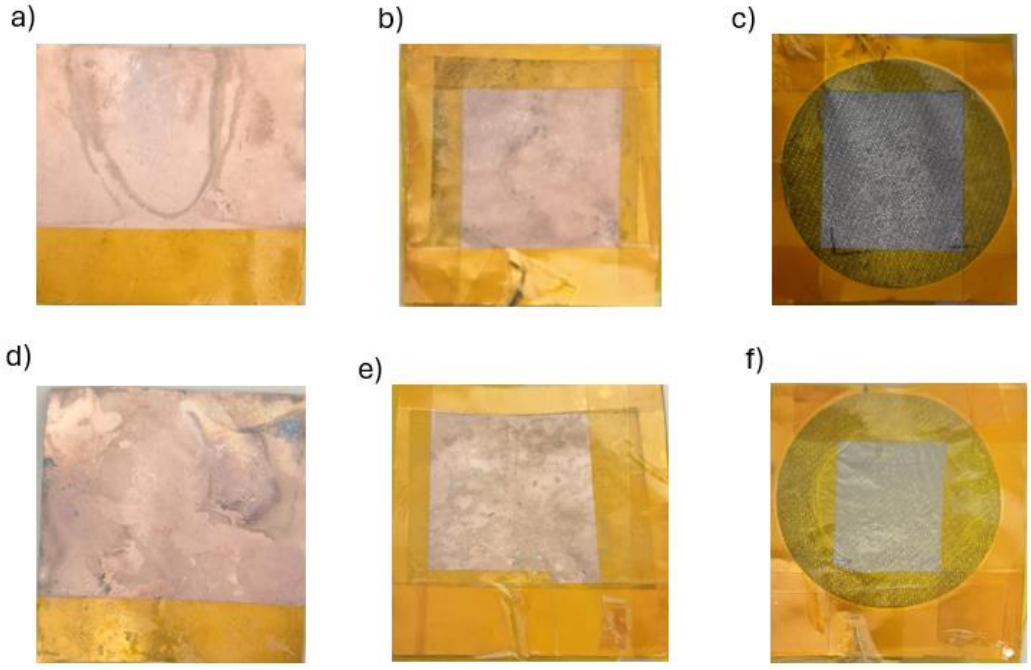

Figure 2.6 Aramid nanofibers (ANF) samples: a) meta-dip coating; b) meta-spray coating; c) meta-filtration; d) para-dip coating; e) para-spray coating; f) para-filtration

2.3 MATERIALS TESTED

As mentioned previously, most commonly used materials possess triboelectric properties and have the ability to generate electric charges due to friction. Based on this and with reference to the triboelectric series (*figure 1.5, figure 1.6*), the PVDF and aramid samples were tested with the following materials:

- Aluminium foil
- Aluminium grid
- Copper
- Kapton
- Paper sheet
- PET-ITO
- PDMS

While all the listed materials are commercially available ready-made, PDMS is supplied in liquid form. To obtain a sample, a curing agent must be added in a 1:10 ratio in weigth with respect of co-polymer. Once the solution is prepared, it was deposited on a copper electrode and allowed to thicken on a spinner at two different speeds (first step at 500 rpm and then at 100 rpm). When the PDMS appears dense, the sample is moved to an oven at 60°C for 1 hour to aid in drying.

2.4 TRIBOELECTRIC CHARACTERIZATIONS

For the produced structures, the following instruments were used:

- Electromechanical shaker. The model is the "*Vibration Test System TV 51110*", manufactured by TIRA Schwingtechnik. It operates with an electromechanical motor designed to vertically oscillate a platform located on the top of the shaker. Through a connected power amplifier and computer, it is possible to adjust the oscillation frequency f (Hz), the acceleration a (m/s^2), and the stroke of the oscillating platform (displacement, mm). These three parameters are interdependent; therefore, it is only necessary to set two of them, as the third will automatically adjust accordingly. In this case the parameters set are frequency and displacement; acceleration is calculated accordingly directly by the software. Additionally, an accelerometer is present to continuously monitor the acceleration, connected to the power amplifier and mounted on the oscillating platform. The entire system is managed via the dedicated VibrationView software.

- Support structure: It consists of a horizontal arm that can be moved vertically, using a screw mechanism along two lateral support arms. Contact and separation between the oscillating platform and the horizontal arm are achieved by adjusting the height of the latter. Figure 2.7 shows an image depicting the shaker and support structure.

- Bench electrometer: The model used is the 6517B, produced by KEITHLEY, a high-resistance electrometer capable of measuring voltage, current, charge, and surface or volume resistance. Temperature and humidity can also be measured using a dedicated thermocouple and additional probe. With a very high internal measurement impedance (200

TΩ), this model is suitable for measuring the electrical parameters of high-impedance devices such as TENGs, while maintaining high accuracy. Using the multimeter, alternating voltage and current across the TENG were measured. The voltage and current measurement ranges were set by the computer connected through a Labview-based interface; measurements were carried out in continuous mode.

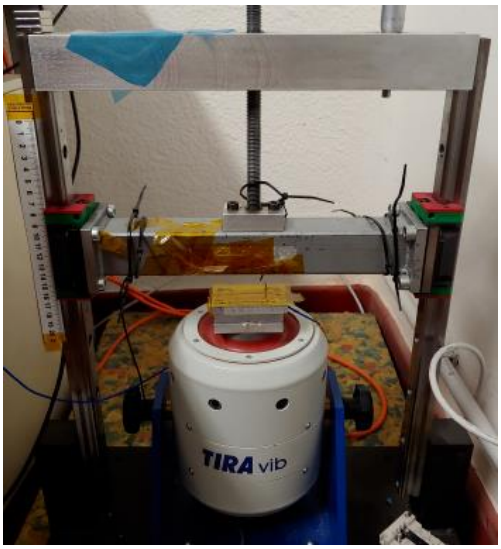

Figure 2.7 Electromechanical shaker used in laboratory with its support structure

The obtained membranes were placed on the two plates visible on the instrument; the first is on the oscillating upper part, and the second on the lower part, which remains fixed. In particular, PDVF fibers samples were put on the upper part and fixed with double-sided tape was used to maintain contact during movements. This is a standard Contact-Separation TENG work mode configuration.
To avoid electrical contact with the shaker or its support structure, the main parts of the samples that come into contact with the structure, namely the back side and the edges, are previously covered with Kapton tape, that is an insulating material. The same Kapton tape was used to fix samples on the lower plate. Samples were fixed in position so that the triboelectric surfaces were perfectly aligned during the contact phase. The horizontal arm is characterized by an adjustable height, which facilitates the assembly and disassembly of the samples.
The mechanical stress applied during the measurement phase includes the application of a force of 30 N.

The tests were conducted at variable oscillation frequencies and displacements:

OSCILLATION FREQUENCY (Hz)	DISPLACEMENT (mm)
2	10
5	10
7	7

Table 2.1 frequencies and displacement values used for triboelectric characterizations

In order to obtain the output values, the bench electrometer cables were used to create a connection with the samples. Specifically, the aim is to connect the positive clamp (red cable) to the more triboelectronegative material (PVDF in our case) and the black clamp to the other material.
The actual voltage and current measurements, obtained through LabVIEW, are started when the acceleration peak reaches approximately 40 m/s^2.

2.4.1 Power and energy output

TENGs devices are evaluated based on the amount of output power they can generate, expressed in W/cm^2. To evaluate the power curve of TENGs, different resistance values were tested in sequence:

- 10 Ω
- 100 Ω
- 1 K Ω
- 10 K Ω
- 100 K Ω
- 1 M Ω
- 10 M Ω
- 100 M Ω

The test samples were connected to a breadboard using clamps, changing resistors after each measurement. Potential measurements were performed by placing the resistors in parallel, while for the current, they were placed in series. In figure 2.7 we can see the electrical circuit (*figure 2.8 a*) and the respective cable connections on the breadboard (*figure 2.8 b*) to obtain output voltage values. While in figure 2.8 there is the parallel resistor configuration (*figure 2.9 a*) in order to obtain current output values and the corresponding breadboard configuration (*figure 2.9 b*) [54].
There are current generator in figure 2.8a and voltage generator in figure 2.9a that represent TENG device in this application.
The cables to the right of the resistors are then connected to the samples placed on the shaker plates; those on the left are connected to the generator (electrometer).

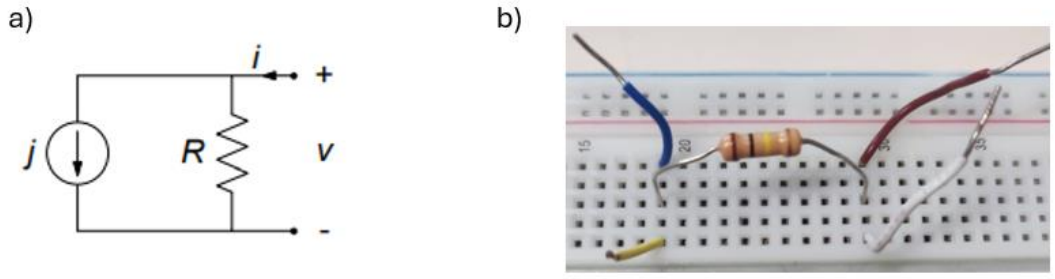

Figure 2.8 a) Electrical scheme of series resistor [54]; b) Breadboard cables connection used in laboratory

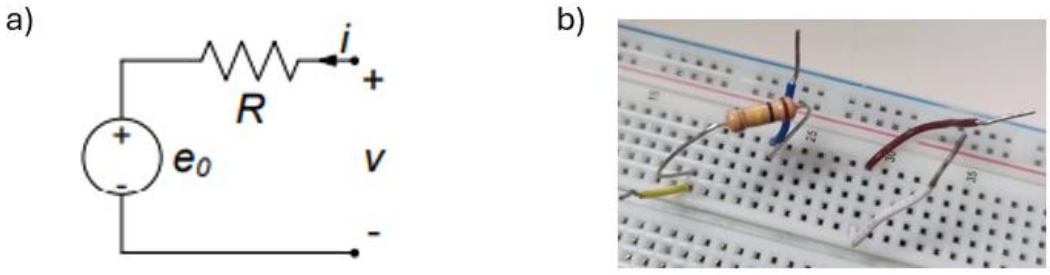

Figure 2.9 a) Electrical scheme of parallel resistor [54]; b) Breadboard cables connection

From Ohm's law we know that the voltage V across a resistor R is directly proportional to the current i flowing through the same resistor R. This could be expressed as:

$$V = iR \tag{2.1}$$

That is equal to:

$$R = \frac{V}{i} \tag{2.2}$$

When connected to resistors, we refer as short circuit condition when R is approaching zero. Open circuit means high values of R, approaching infinity.
Referring to the previous equations (2.1 and 2.2), as the tested resistance values increase, we observe an increase in voltage and a decrease in the generated current values [55].
Power is obtain in the following way [56]:

$$P = Vi = iR^2 \tag{2.3}$$

The theorical power trend is shown on figure 2.10, where the maximum power is reached matching the generator load [55].

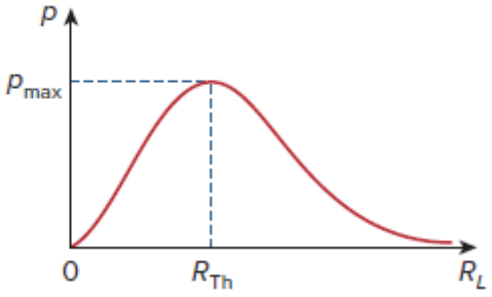

Figure 2.10 Trend of the power curve as resistance increases [55]

Another important feature of TENGs is the produced energy.

In this application, different values of both electrolytical and polyester commercial capacitors are inserted into the breadboard, which was subsequently connected to the samples placed on the shaker. The aim is to charge these capacitors.

To effectively store the energy collected through mechanical movements and use it as a power source (the main purpose of TENGs), it is necessary to convert the generated alternating current (AC) energy into direct current (DC). This conversion is essential because most electronic devices operate on direct current. Diodes can be used as rectifiers to perform this conversion: a diode bridge allows current to flow in only one direction, thus transforming AC into DC. By inserting the diodes into the breadboard, a rectifier circuit is created, making the energy produced by the TENG ready to be stored in capacitors or batteries, where it can then be used to power small electronic devices [57].

In figure 2.11 there is an example of a capacitor circuit with diode bridge connected to a TENG [58].

We can quantify the charge transferred Q and, consequently, the energy involved E through the value of capacitor and the corresponding generated voltage [59]:

$$Q = C\,V \tag{2.4}$$

$$E = \frac{1}{2} C\,V^2 \tag{2.5}$$

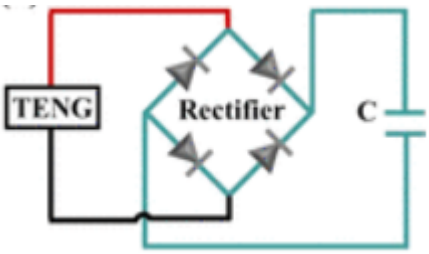

Figure 2.11 Diagram of the equivalent circuit showing the TENG charging a commercial capacitor through a bridge rectifier [58]

In this work we used four different capacitor values:

- 0.1 µF
- 1 µF
- 4.7 µF
- 10 µF
- 47 µF

3 RESULTS

3.1 MATERIALS CHARACTERIZATIONS

PVDF and aramid samples were morphologically characterized using SEM (*scanning electron microscopy*). Due to the insulating properties of PVDF, it was coated with a thin layer of platinum before being analyzed in the SEM to prevent electron repulsion with the electron beam generated by the instrument.
Figure 3.1 shows PVDF fibers SEM images. We can easily observe that in the samples obtained through oriented deposition, the fibers appear to follow a sort of main direction (*figures 3.1a and 3.1c*). This does not occur, as expected, in the samples obtained through random deposition (*figures 3.1b and 3.1d*).
The fiber diameters were also measured and shown in table 3.1:

PVDF SAMPLES	**DIAMETER (μm)**
SAMPLE 1 ORIENTED	440 ÷ 670
SAMPLE 1 RANDOM	250 ÷ 350
SAMPLE 3 ORIENTED	270 ÷ 380
SAMPLE 3 RANDOM	160 ÷240

Table 3.1 PDVF fibers diameters obtained by SEM measurements

As we can see in the table, samples with oriented fiber deposition exhibit a larger diameter. Furthermore, from these values, we can deduce that increasing the deposition time, under the same type of collector used, causes saturation on the collector, resulting in the flattening of the fibers.
Additionally, the sample obtained from one hour of oriented deposition was characterized after being tested triboelectrically and subjected to the application of a force for approximately 12 hours.
In Figure 3.2, we can see a comparison between the new sample and the used sample. The diameter and morphology of the fibers have been preserved despite the applied force. This ensures good maintenance of the triboelectric structure over time with PDVF as tribonegative material.

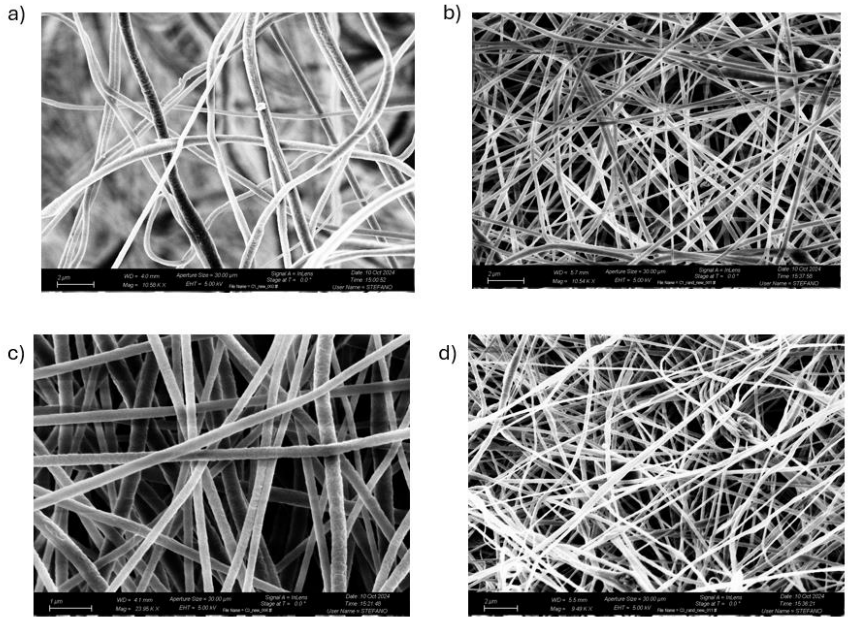

Figure 3.1 SEM images of PVDF samples: a) 1h Oriented deposition; b) 1h Random edeposition; c) 3h Oriented deposition; d) 3h Random deposition

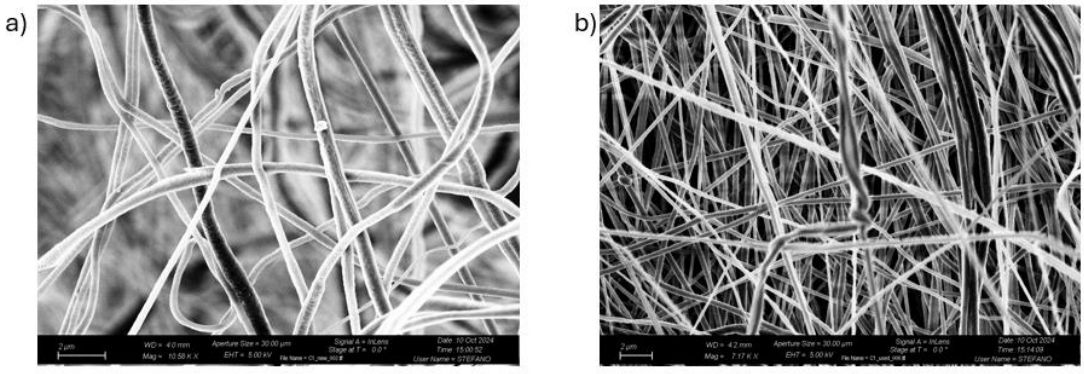

Figure 3.2 Comparison between 1h Oriented deposition PVDF fibers: a) new sample; b) tested sample

Morphological characterization was also evaluate for both meta and para aramid nanofibers samples obtained by dip coating with, respectively, 1, 2 and 3 subsequent immersions. The technique does not appear to be optimal for depositing fibers on the copper sheet, as we can see in figure 3.3. The fibers appear as agglomerates, but the distribution did not prove to be uniform.

Due to these results, dip coating ANF were not subsequently characterized at the triboelectric level.

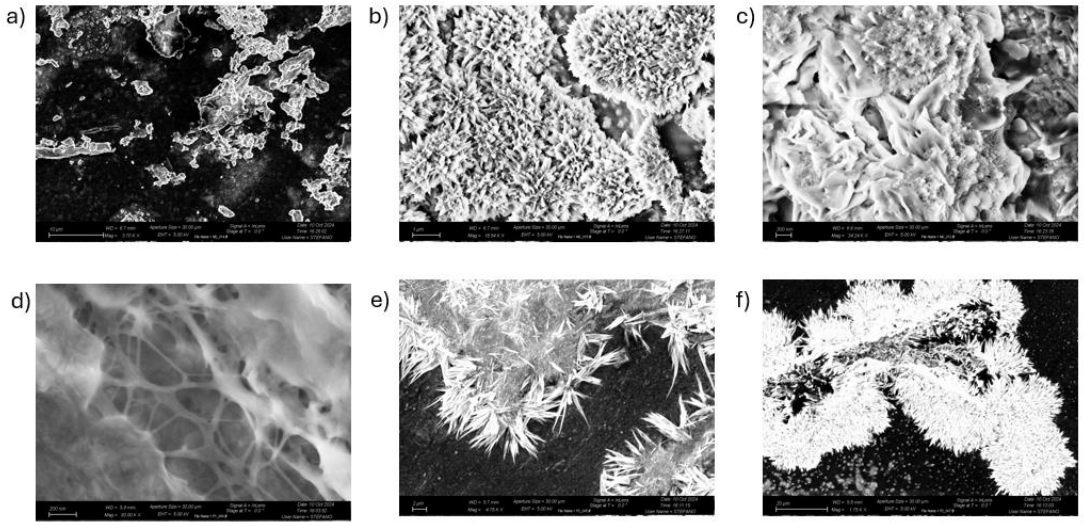

Figure 3.3 SEM aramid nanofibers: a) m-ANF with 1 immersion; b) m-ANF with 2 immersions; c) m-ANF with 3 immersions; d) p-ANF with 1 immersion; e) p-ANF with 2 immersions; f) p-ANF with 3 immersions.

3.2 TRIBOELECTRIC CHARACTERIZATIONS

3.2.1 PVDF samples

The triboelectric measurements were initially evaluated, as previously mentioned, at frequencies of 2 Hz, 5 Hz, and 7 Hz. All measurements were also conducted for a minimum of 2 minutes to achieve stability in the output results. The measurements on paper, aluminum, copper, Kapton, PDMS, and PET, conducted twice under the same conditions, showed reproducibility in the results.

Analyzing the results in terms of voltage and current obtained with the three different applied frequency values between 1h Oriented deposition PVDF fibers and all other materials, the 2 Hz frequency was excluded from further analysis because of the low output it produced.

All the voltage and current results are expressed and compared in terms of peak-to-peak values (V_{pp}, i_{pp}), referring to the range between the positive and negative peaks measured.

In figures 3.4 and 3.5 we can see the characteristic trend of these measured quantities.

To show and extract positive and negative voltage and current peaks only three seconds of signal recording are shown (*figure 3.4a and 3.4b*). Voltage measurements, unlike current measurements that stabilize to a reference value, are affected by fluctuations caused by external factors such as noise. In this case, it is necessary to remove the baseline in order to stabilize the results.

The example shown in figures 3.4 was tested on PDMS with an applied frequency of 5 Hz and PVDF *sample1*. While, figure 3.5 shows output values for PET tested with same PVDF sample but with a configured frequency of 7 Hz. In figures 3.6 and 3.7 we can see output of aluminium foil-PVDF-PDMS at 5 Hz.

The same trend, with different values, was observed in all the analyses.

Figures 3.8 and 3.9 will show differences between output values reach at different frequencies, 2 Hz, 5 Hz and 7 Hz.

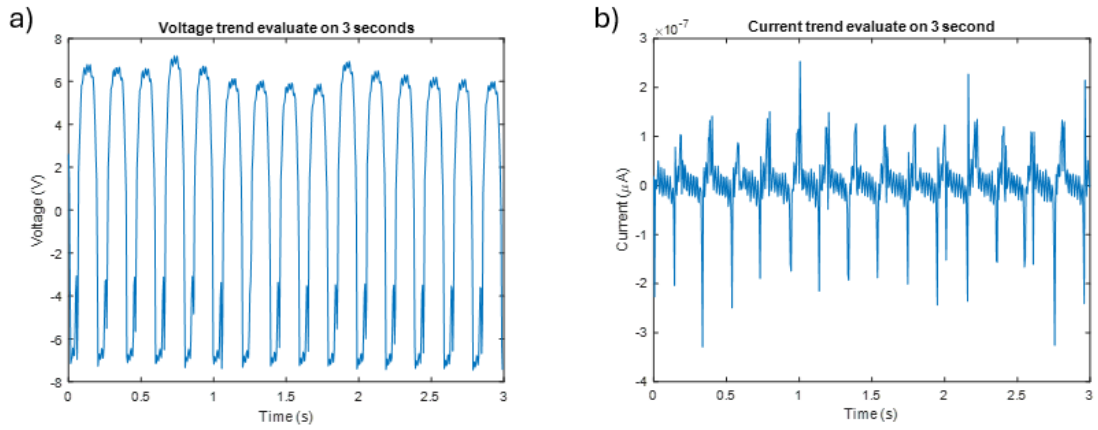

Figure 3.4 Electrical output results tested with copper-PVDF-PDMS sample at 5 Hz: a) voltage; b) current

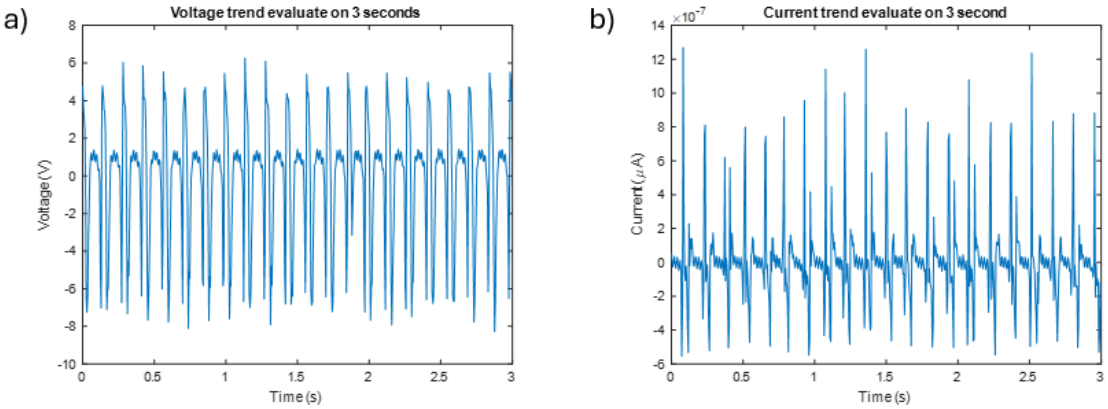

Figure 3.5 Electrical output results tested with copper- PVDF-PET sample at 7 Hz: a) voltage; b) current

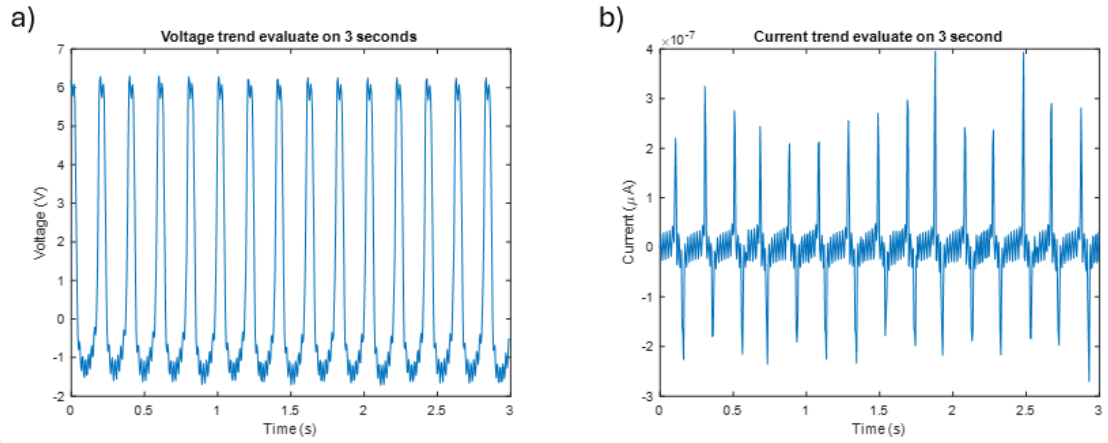

Figure 3.6 Electrical output results tested with aluminium foil-PVDF-PDMS sample at 5 Hz: a) voltage; b) current

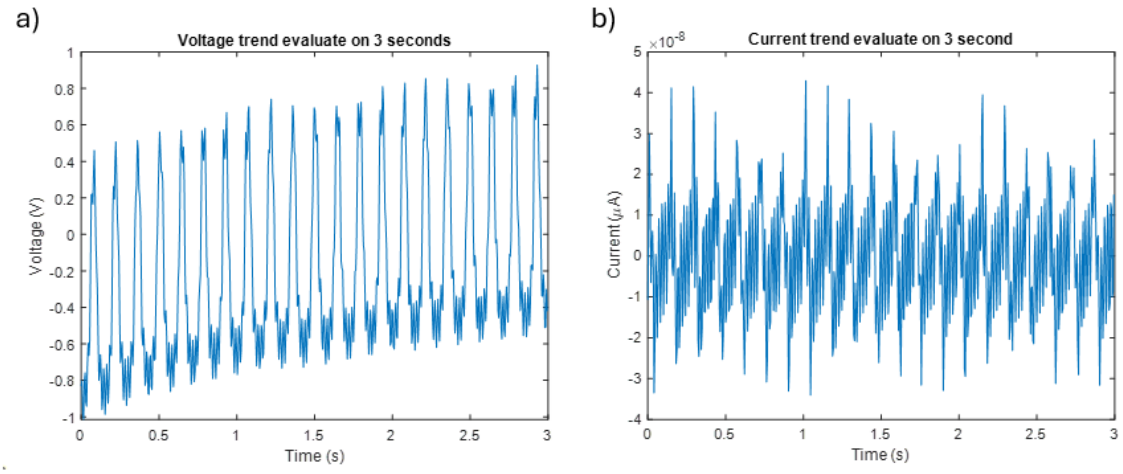

Figure 3.7 Electrical output results tested with alumium foil- PVDF-PET sample at 7 Hz: a) voltage; b) current

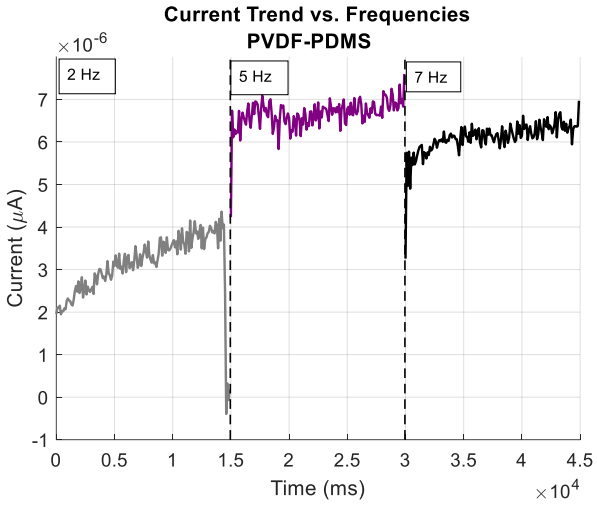

Figure 3.8 Current trend at variables frequencies: 2 Hz, 5 Hz, 7 Hz measured on PDMS sample.

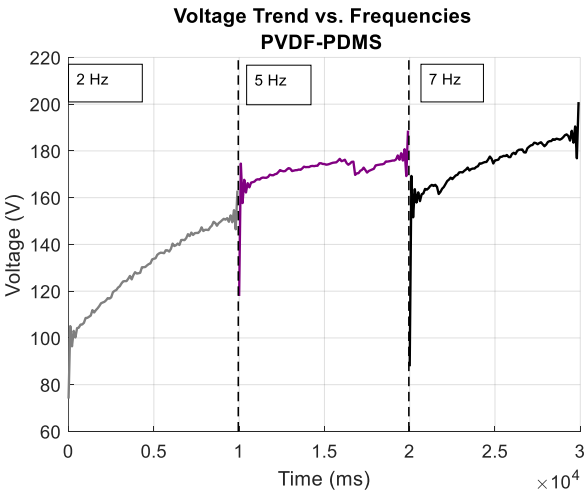

Figure 3. 9 Voltage trend at variables frequencies: 2 Hz, 5 Hz, 7 Hz measured on PDMS sample.

In general, the output values did not show a dependency on the type of material chosen as the electrode. For ease of construction and material handling, as aluminum is easily prone to bending, subsequent fiber samples were deposited on copper.

The following tables show a summary of the peak-to-peak maximum voltage (V_{pp}) and current (i_{pp}) values obtained during testing conducted at 5 Hz and 7 Hz.
In detail, we have:

Maximum V_{pp} measured at 5 Hz expressed in *Volt*

PVDF FIBERS MATERIALS	1H ORIENTED DEPOSITION	1H RANDOM DEPOSITION	3H ORIENTED DEPOSITION	3H RANDOM DEPOSITION
ALUMINIUM	6.70	31.70	9.75	15.22
AL GRID	87.70	14.3	25.76	24.85
COPPER	14.64	18.77	13.4	16.35
KAPTON	7.35	36.17	28	17.70
PAPER	19.45	69.65	28.18	16.05
PDMS	26.36	34.16	188.73	21.22
PET	17.87	28.27	19.42	38.06

Table 3.2 Voltage tribelectric output (V) for all the material tested at 5 Hz

Maximum i_{pp} measured at 5 hz expressed in *μA*

PVDF FIBERS MATERIALS	1H ORIENTED DEPOSITION	1H RANDOM DEPOSITION	3H ORIENTED DEPOSITION	3H RANDOM DEPOSITION
ALUMINIUM	0.80	3.66	1.01	1.60
AL GRID	1.31	1.35	2.12	2.20
COPPER	1.13	1.65	0.63	1.86
KAPTON	0.85	3.70	2.64	2.40
PAPER	1.43	17.8	2.10	1.87
PDMS	2.49	3.13	6.33	2.49
PET	3.97	4.62	4.01	3.53

Table 3.3 Current tribelectric output (μA) for all the material tested at 5 Hz

Maximum V_{pp} measured at 7 Hz expressed in *Volt*

PVDF FIBERS MATERIALS	1H ORIENTED DEPOSITION	1H RANDOM DEPOSITION	3H ORIENTED DEPOSITION	3H RANDOM DEPOSITION
ALUMINIUM	7.81	30.05	12.21	12.29
AL GRID	63.95	14.97	23.11	20.08
COPPER	12.30	17.24	18.84	14.44
KAPTON	8.73	38.92	30.80	19.57
PAPER	15.29	79.77	25.87	16.91
PDMS	30.11	40.05	177.76	17.48
PET	14.63	30.58	21.81	30.7

Table 3. 4 Voltage tribelectric output (V) for all the material tested at 7 Hz

Maximum i_{pp} measured at 5 hz expressed in *μA*

PVDF FIBERS MATERIALS	1H ORIENTED DEPOSITION	1H RANDOM DEPOSITION	3H ORIENTED DEPOSITION	3H RANDOM DEPOSITION
ALUMINIUM	0.96	2.30	0.73	1.34
AL GRID	5.11	1.82	1.42	1.19
COPPER	0.71	1.51	0.76	1.34
KAPTON	0.92	3.65	2.12	5.07
PAPER	1.41	20.70	2.04	2.66
PDMS	1.81	2.44	6.47	1.97
PET	2.32	3.93	8.72	4.23

Table 3.5 Current tribelectric output (μA) for all the material tested at 7 Hz

From the literature, we would expect an increasing current and voltage output with a rise in the applied frequency. In our tests, this did not occur. As we can see, some values obtained at 5 Hz are higher than those tested at 7 Hz. This could be due to the small difference between 5 and 7, as in the case of the tests at 2 Hz, where the output values were indeed lower.
The aim of this work is both to find the optimal material and to determine the best PVDF type sample that maximizes output performance. So, the next figures will display histograms that compare the peak-to-peak measurements of voltage and current. The values shown in the histogram are obtained from the average of all peak-to-peak values calculated for the individual tests, and the bar represents the standard deviation of these measurements.
We obtain standard deviation through the following formula:

$$\sigma = \sqrt{\frac{\Sigma(x_i-\mu)^2}{N}} \tag{3.1}$$

Where x_i is the value of each measurent, μ is the mean value of the total measurements and N is the element number of sample.
It involves calculating the sample mean, then for each value, calculating the difference between that value and the previously calculated mean. This difference is then squared for each value, and the sum of these squared differences is computed.
Figures 3.10 and 3.11 show output obtained by 1h Oriented deposition of PVDF fibers both for voltage and current at two different values of frequency.

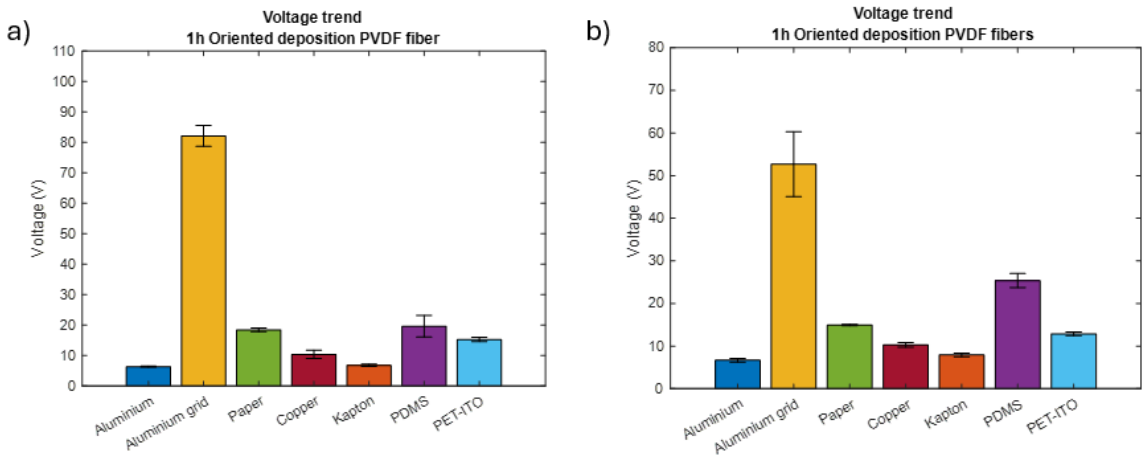

Figure 3.10 Comparison between PVDF-sample1 and all the materials tested in terms of voltage output at: a) 5 Hz; b) 7 Hz

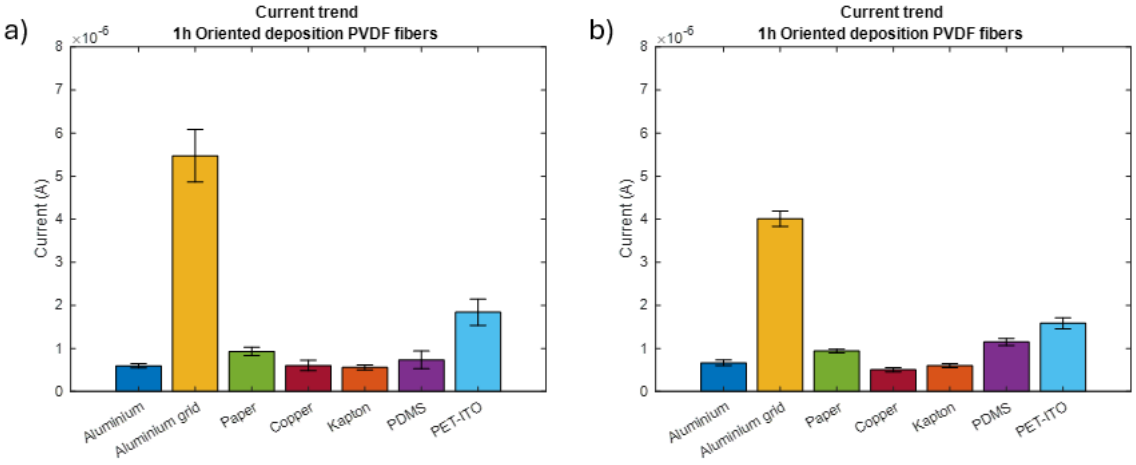

Figure 3.11 Comparison between PVDF-sample1 and all the materials tested in terms of current output at: a) 5 Hz; b) 7 Hz

Figures 3.12 and 3.13 present output voltage and current value generated between 1h Random deposition PVDF sample and other materials.

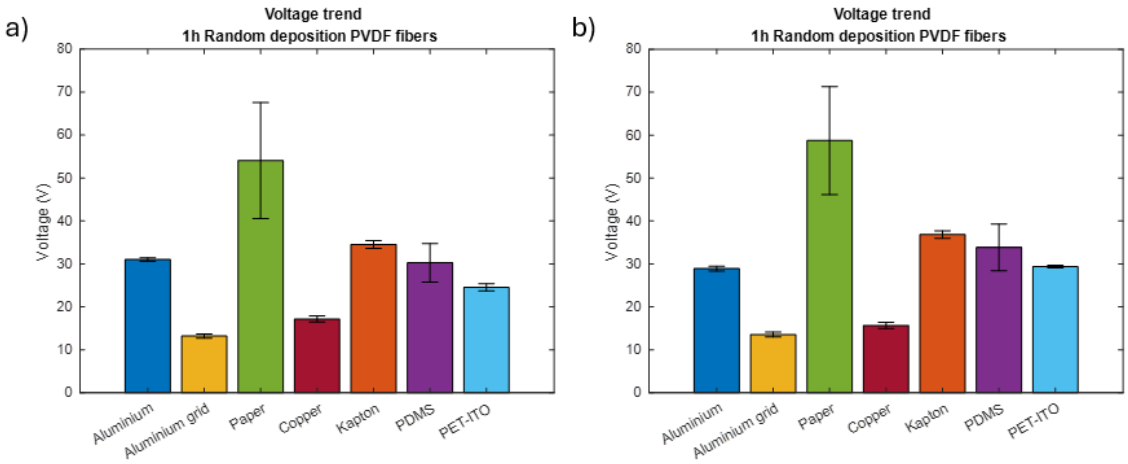

Figure 3.12 Comparison between PVDF-sample1_random and all the materials tested in terms of voltage output at: a) 5 Hz; b) 7 Hz

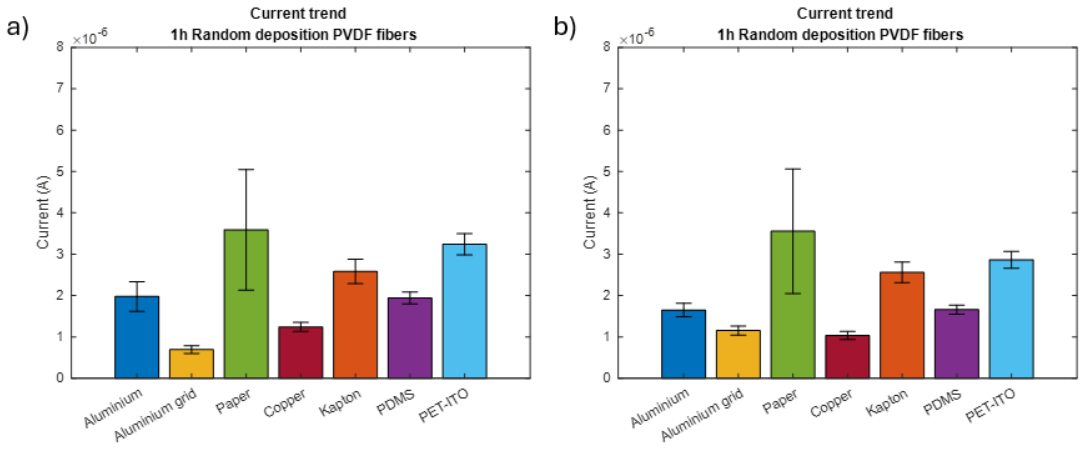

Figure 3.13 Comparison between PVDF-sample1_random and all the materials tested in terms of current output at: a) 5 Hz; b) 7 Hz

Figures 3.14 and 3.15 present 3h Oriented deposition PVDF sample output, while figures 3.16 and 3.17 contain the mean output value reached with 3h Random deposition PVDF fiber sample.

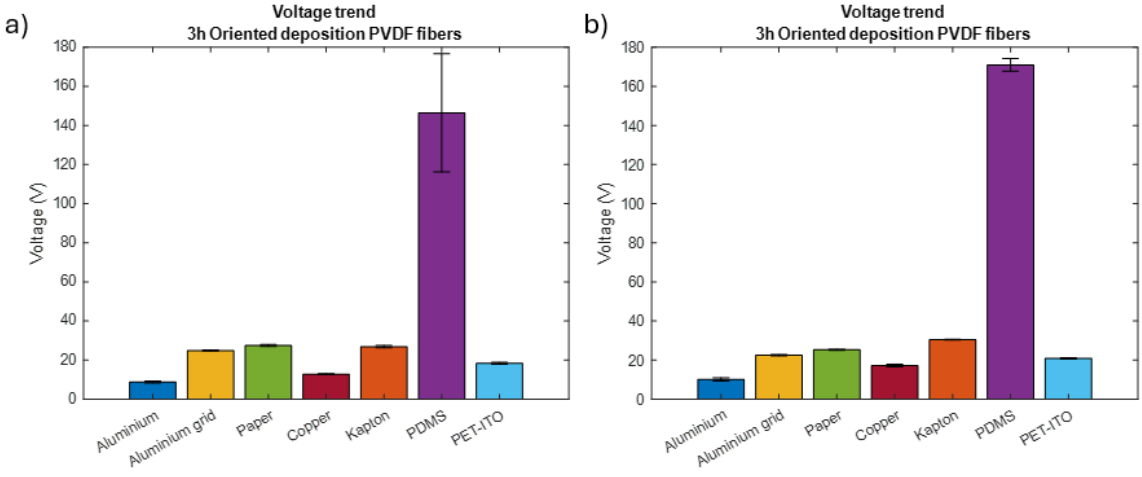

Figure 3.14 Comparison between PVDF-sample3 and all the materials tested in terms of voltage output at: a) 5 Hz; b) 7 Hz

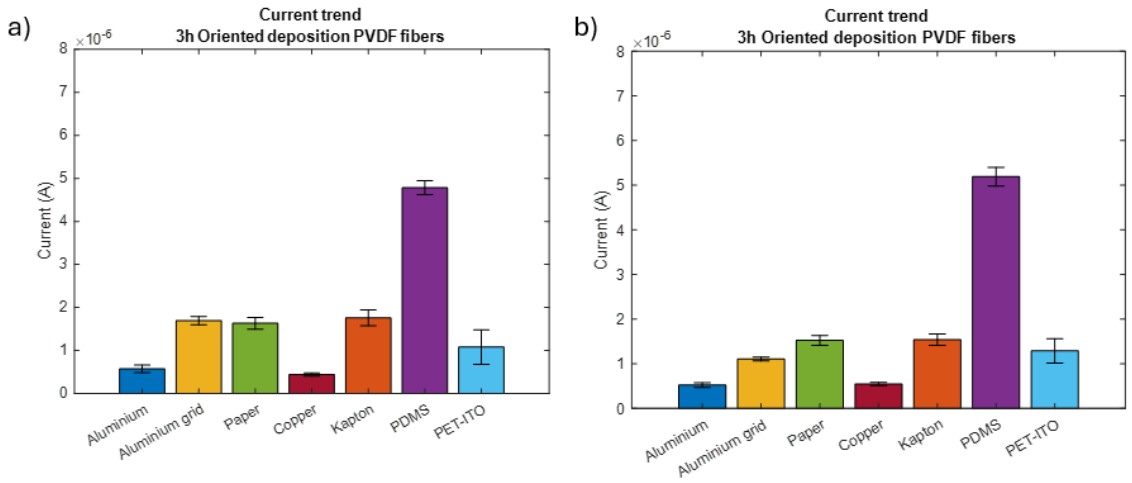

Figure 3.15 Comparison between PVDF-sample3 and all the materials tested in terms of current output at: a) 5 Hz; b) 7 Hz

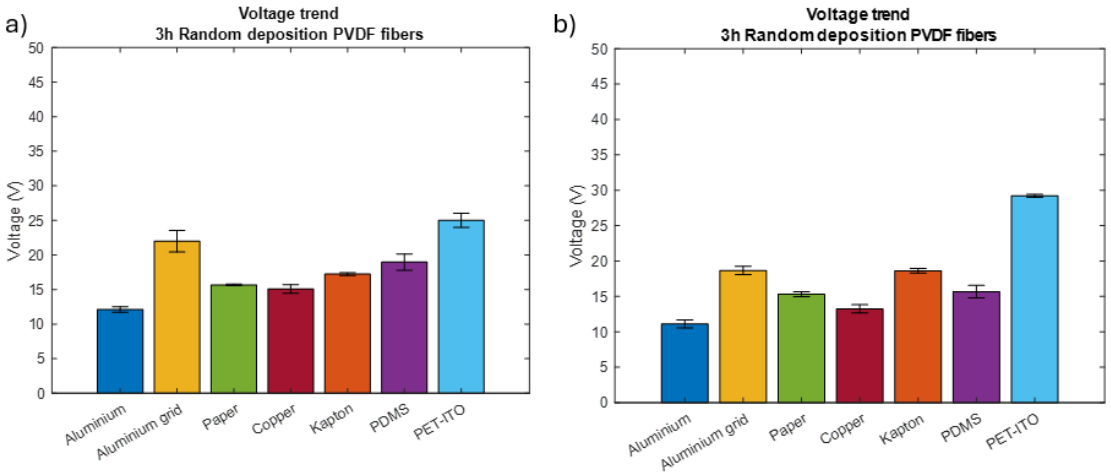

Figure 3.16 Comparison between PVDF-sample3_random and all the materials tested in terms of voltage output at: a) 5 Hz; b) 7 Hz

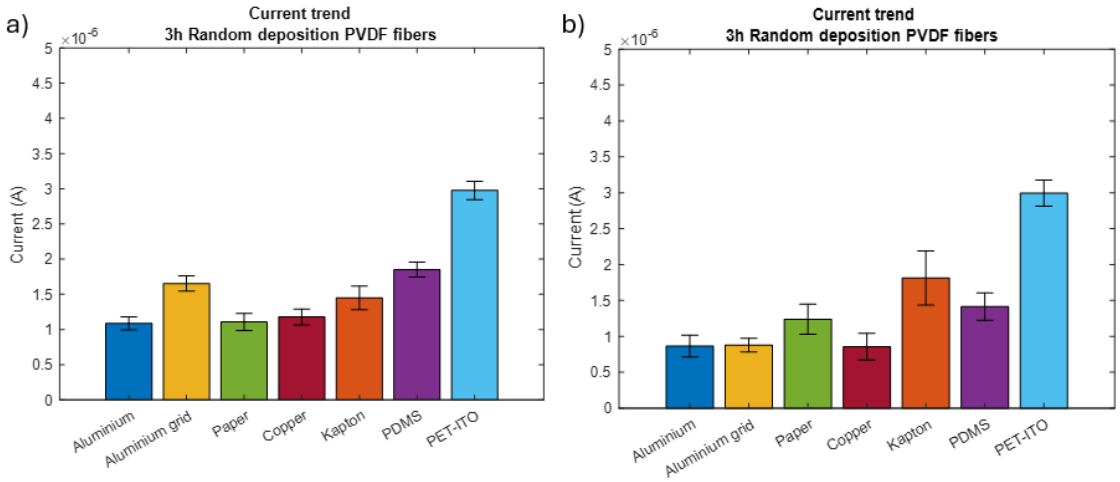

Figure 3.17 Comparison between PVDF-sample3_random and all the materials tested in terms of current output at: a) 5 Hz; b) 7 Hz

As we can see from these histograms most of the promisimg values are related to test conducted on PDMS and PET-ITO. Also tests performed on paper foil show good values but they are affected by high variability, visible from the standard deviation bar. This results in lower consistency than the PDMS and PET ones.
Therefore, as a first step, we can define PDMS and PET as the most effective materials among those tested. The next objective, as previously mentioned, is to identify the best PDVF fiber sample.
The following figures (from *figure 3.18 to figure 3.24*) will present histograms comparing the results for each previously mentioned material, showing how the output changes with different fiber morphology.
Based on the results discussed earlier, PVDF fiber sample made by 5 hours of deposition and random orientation (*sample5_random*) was tested only with PDMS and PET. Due to the high similarity between the tests conducted at 5 Hz and 7 Hz, only the results obtained at 5 Hz will be shown to avoid redundancy.

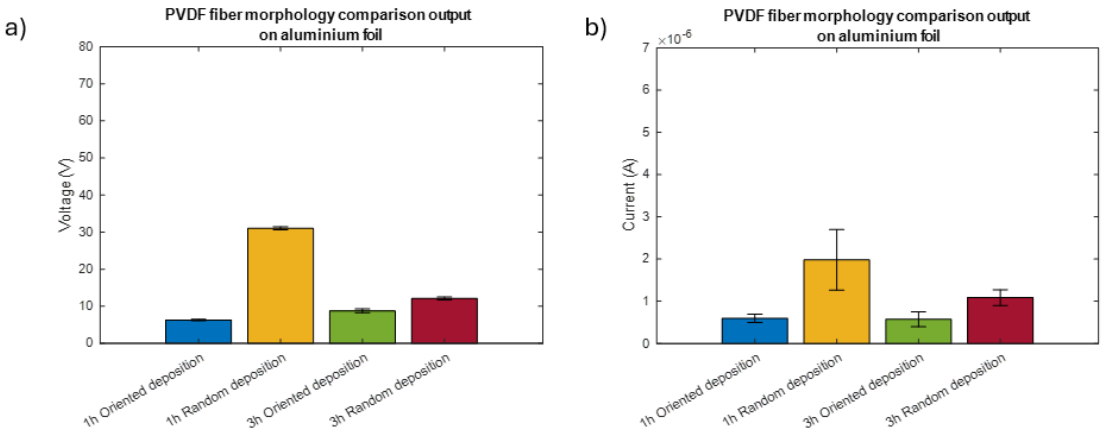

Figure 3.18 Electrical output obtained from different PDVF fiber samples and alumium foil at 5 Hz: a) voltage; b) current

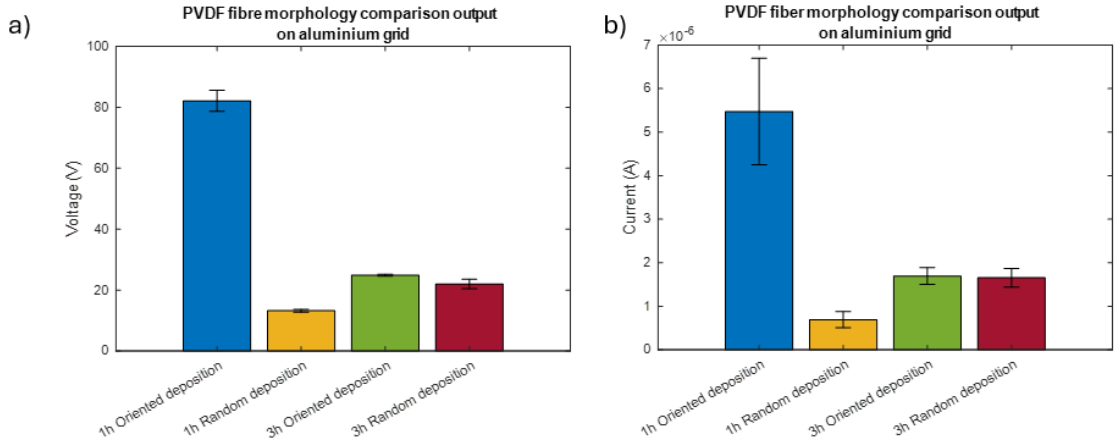

Figure 3.19 Electrical output obtained from different PDVF fiber samples and alumium nanometric grid at 5 Hz: a) voltage; b) current

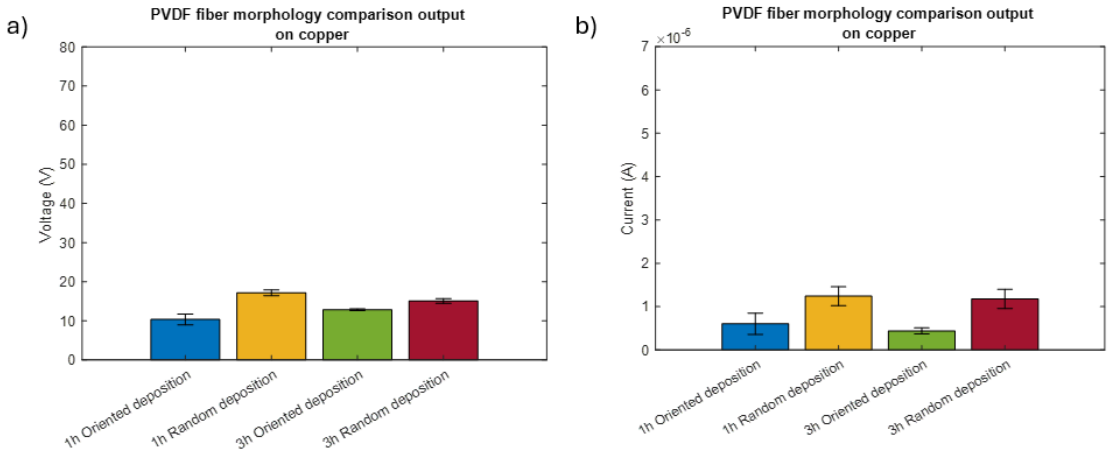

Figure 3.20 Electrical output obtained from different PDVF fiber samples and copper foil at 5 Hz: a) voltage; b) current

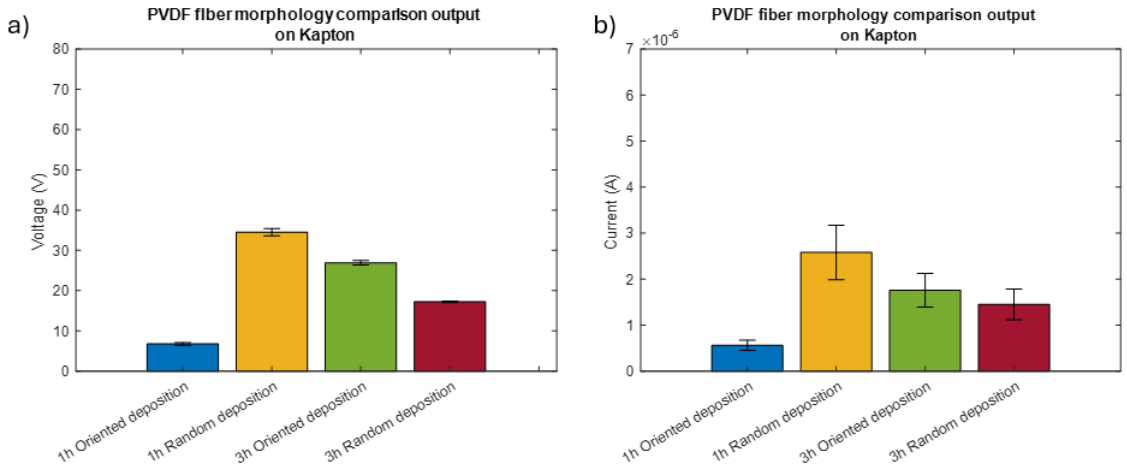

Figure 3.21 Electrical output obtained from different PDVF fiber samples and kapton foil at 5 Hz: a) voltage; b) current

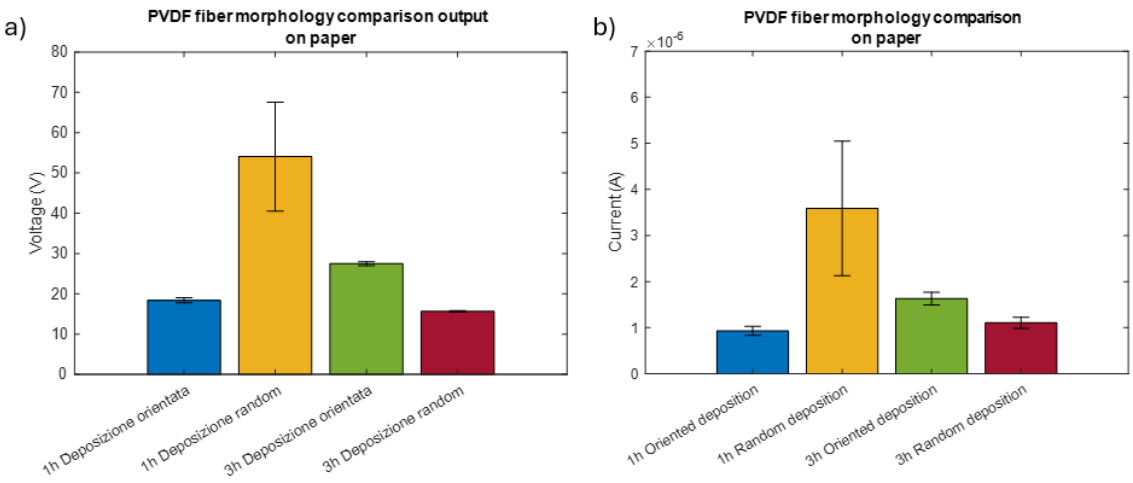

Figure 3.22 Electrical output obtained from different PDVF fiber samples and paper at 5 Hz: a) voltage; b) current

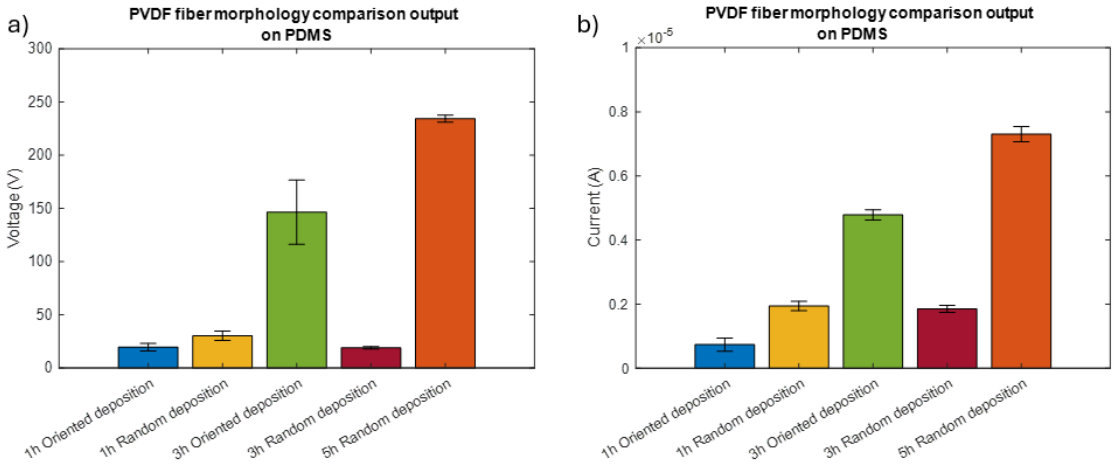

Figure 3.23 Electrical output obtained from different PDVF fiber samples and PMDS at 5 Hz: a) voltage; b) current

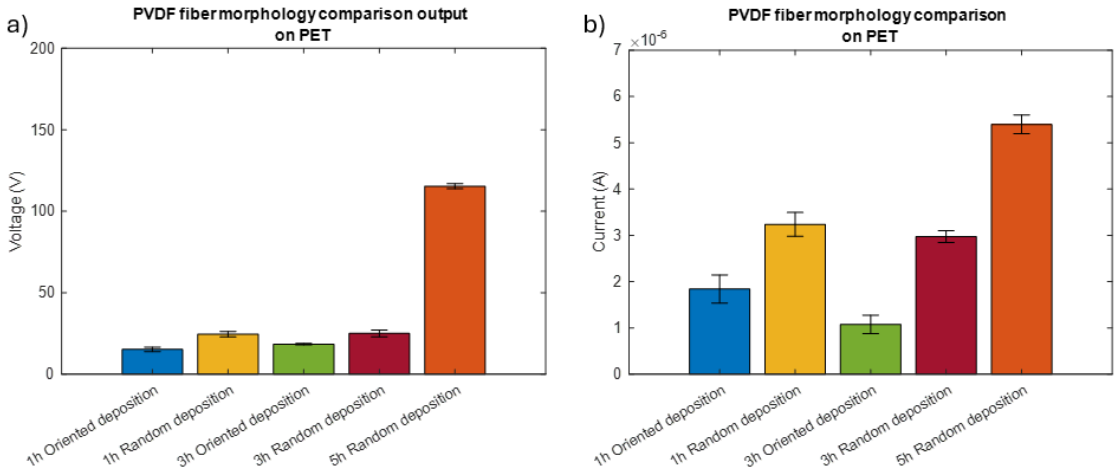

Figure 3.24 Electrical output obtained from different PDVF fiber samples and PET at 5 Hz: a) voltage; b) current

At the end of these tests we can see how *sample5_random* PVDF is characterized by the highest, for both voltage and current, output values.

3.2.2 Power output

To provide further control over the output values, the samples are connected to a resistor circuit (in series for current and in parallel for voltage) to achieve a gradual variation in the load. Increasing the value of the resistor placed in parallel causes the voltage measurement to approach the open-circuit value (measured in previous tests without a load). Similarly, when the value of the resistor placed in series is reduced, the calculated current should approach the previously measured short-circuit value.
Another evaluation parameter is the characteristic power curve, obtained by assessing the output voltage and current values as the resistance varies.
According to Ohm's law, as R increases, there will be an increase in voltage and a decrease in output current.

$$R = \frac{V}{i} \tag{3.2}$$

In next figures we can show the response of voltage and current to changes in resistance along with the associated power curve ($\frac{\mu W}{cm^2}$); in our case the active area of samples is always 3x3 cm^2.
Power is obtained by the following equation:

$$P = Vi \tag{3.3}$$

To obtain the curve the product of voltage and current is made for every resistence's value tested.
Theoretical power curve has a bell-shaped form: low for small resistance values, a peak at the medium values, and a subsequent decrease as the resistance increases further. However, the tests conducted in this study are limited to 'low' resistance values, which do not allow for visualization of the overall trend because of the samples high internal resistence .
Also, for the purpose of simplicity in representation, only the results obtained with an applied frequency of 5 Hz will be shown.
Still considering the results previously discussed, the tests with the resistors were carried out by testing the most promising materials, such as:

- Aluminium nanometric grid (*from figure 3.25 to 3.28*)
- Kapton (*from figure 3.29 to 3.32*)
- Paper foil (*from figure 3.33 to 3.36*)
- PDMS (*from figure 3.37 to 3.40*)
- PET (*from figure 3.41 to 3.44*)

Results are expressed in terms of voltage and current trend and, in another figure, power curve tested with all four PVDF samples described previously (*sample1; sample 1_random; sample3; sample3_random*).

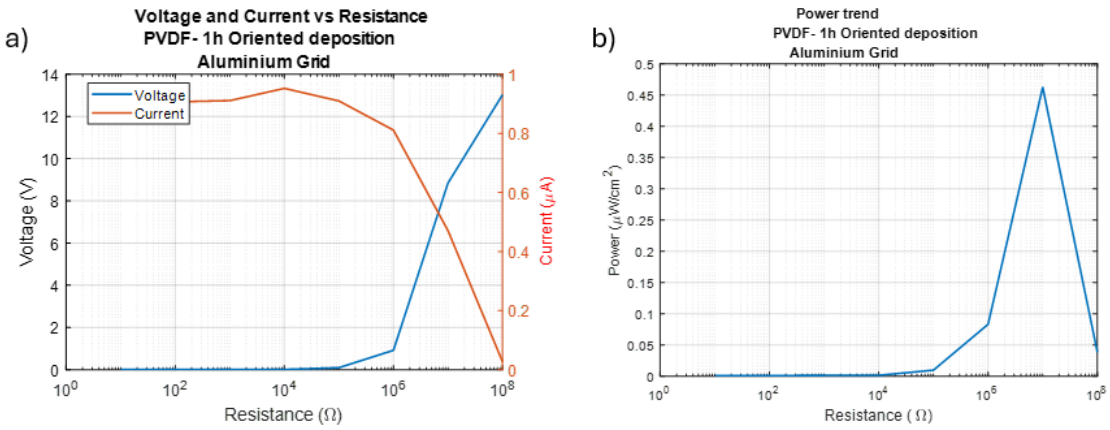

Figure 3.25 TENG output with resistors connection between aluminium grid and PVDF sample1: a) current and voltage trend; b) power curve

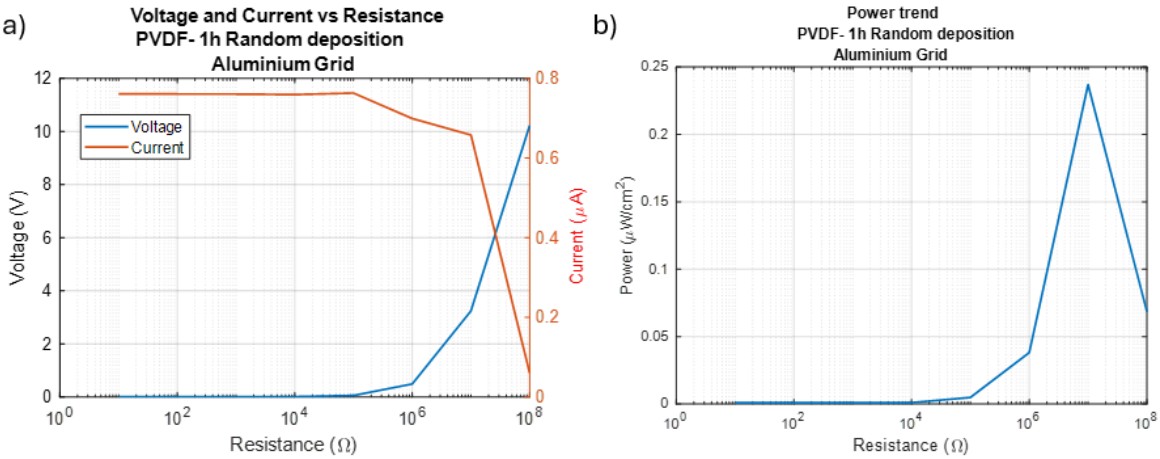

Figure 3.26 TENG output with resistors connection between aluminium grid and PVDF sample1_random: a) current and voltage trend; b) power curve

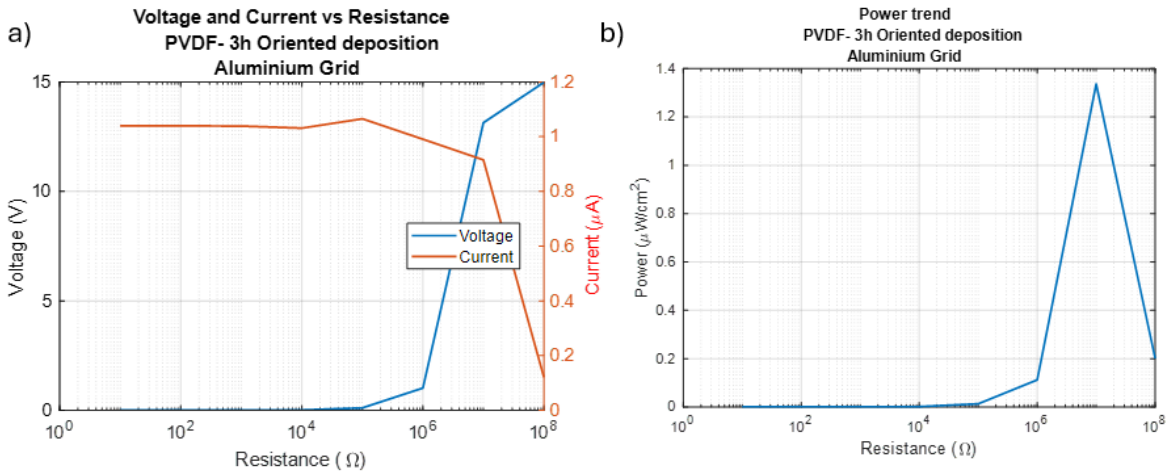

Figure 3.27 TENG output with resistors connection between aluminium grid and PVDF sample3: a) current and voltage trend; b) power curve

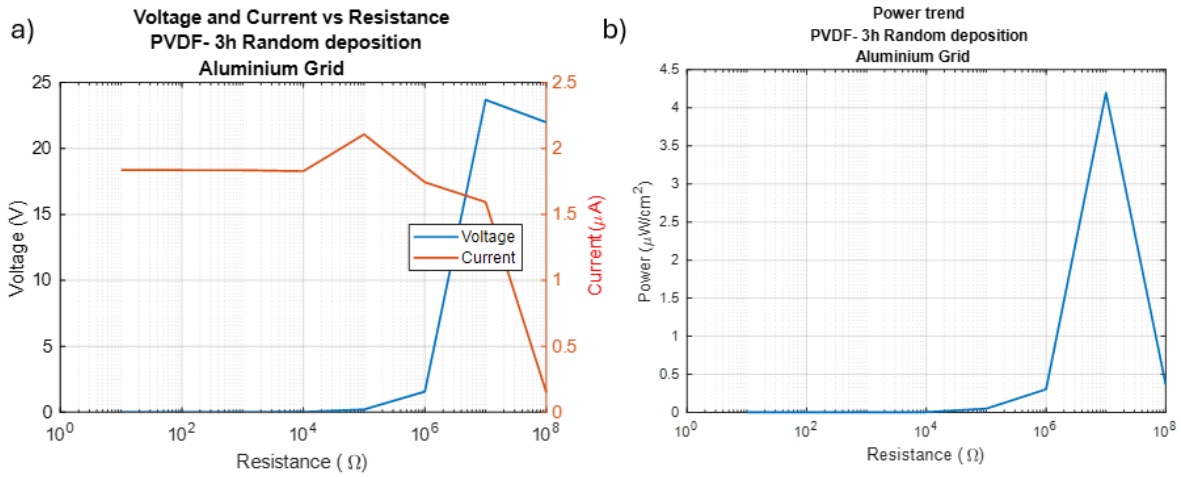

Figure 3.28 TENG output with resistors connection between aluminium grid and PVDF sample3_random: a) current and voltage trend; b) power curve

We can observe how fast, for aluminium grid, output power increase when the samples' time of deposition raises. With the same time of deposition, in this case, output is better for random deposition's sample.

Next graphs will evaluate various PVDF samples tested with kapton:

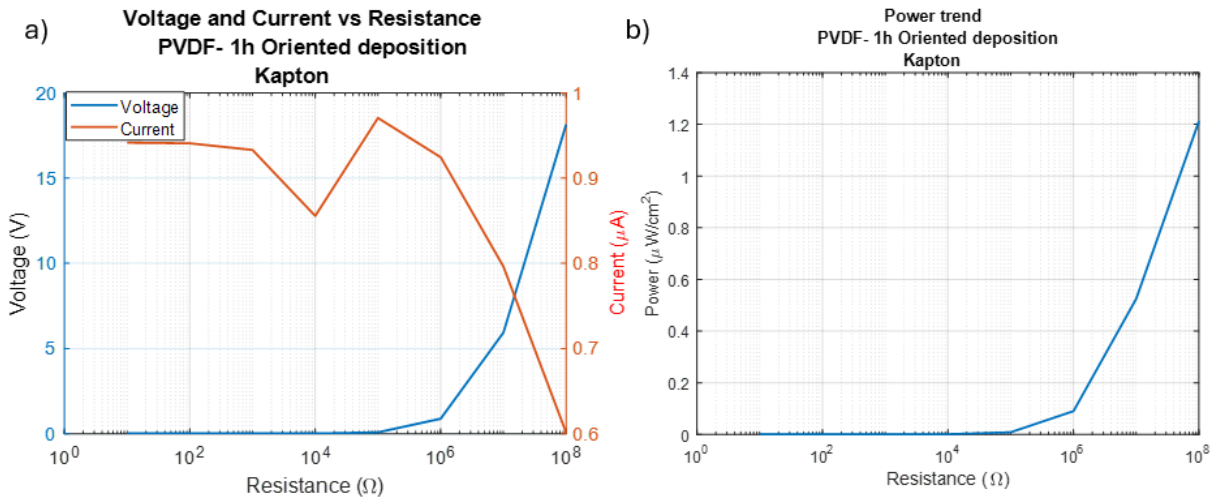

Figure 3. 29 TENG output with resistors connection between kapton and PVDF sample1: a) current and voltage trend; b) power curve

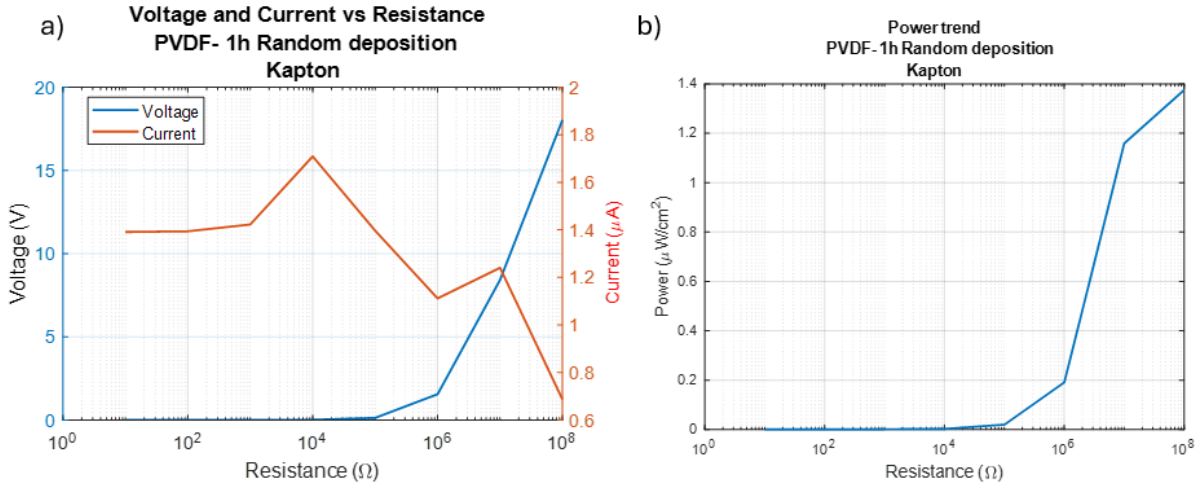

Figure 3.30 TENG output with resistors connection between kapton and PVDF sample1_random: a) current and voltage trend; b) power curve

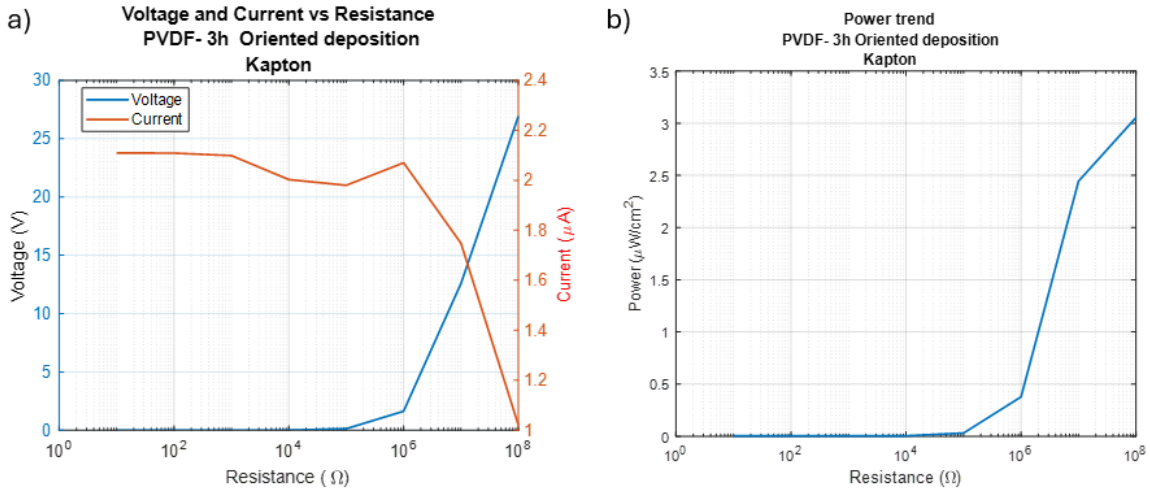

Figure 3.31 TENG output with resistors connection between kapton and PVDF sample3: a) current and voltage trend; b) power curve

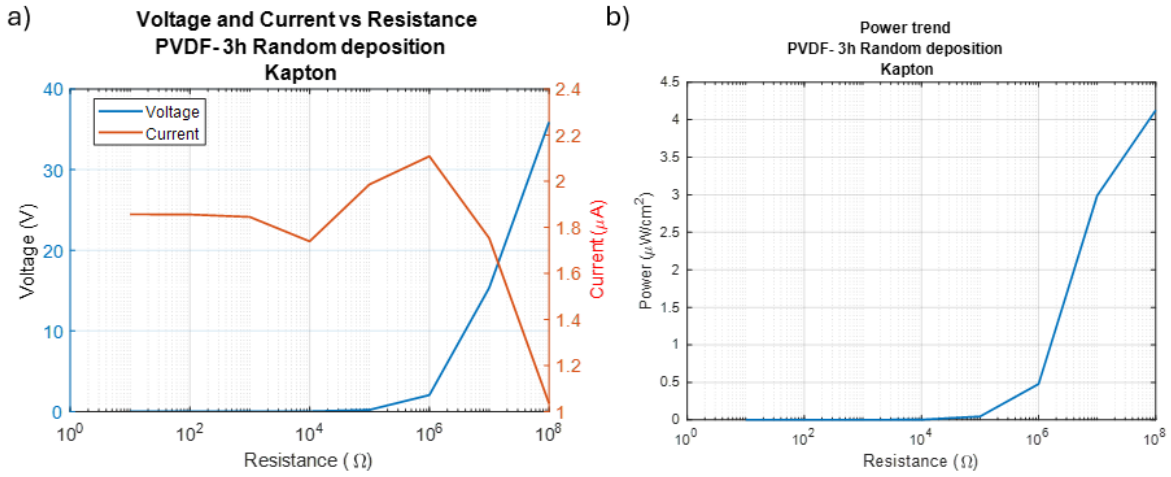

Figure 3.32 TENG output with resistors connection between kapton and PVDF sample3_random: a) current and voltage trend; b) power curve

Comparing power maximum value, we can confirm the effectiveness of random deposition samples with higher times of deposition.

Now, we will examine paper foil's results:

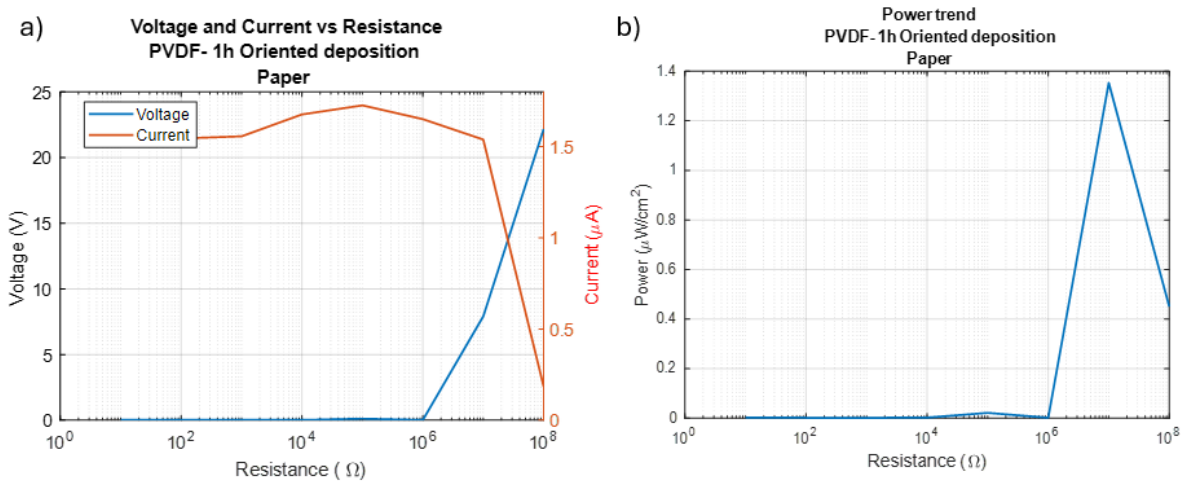

Figure 3.33 TENG output with resistors connection between paper and PVDF sample1: a) current and voltage trend; b) power curve

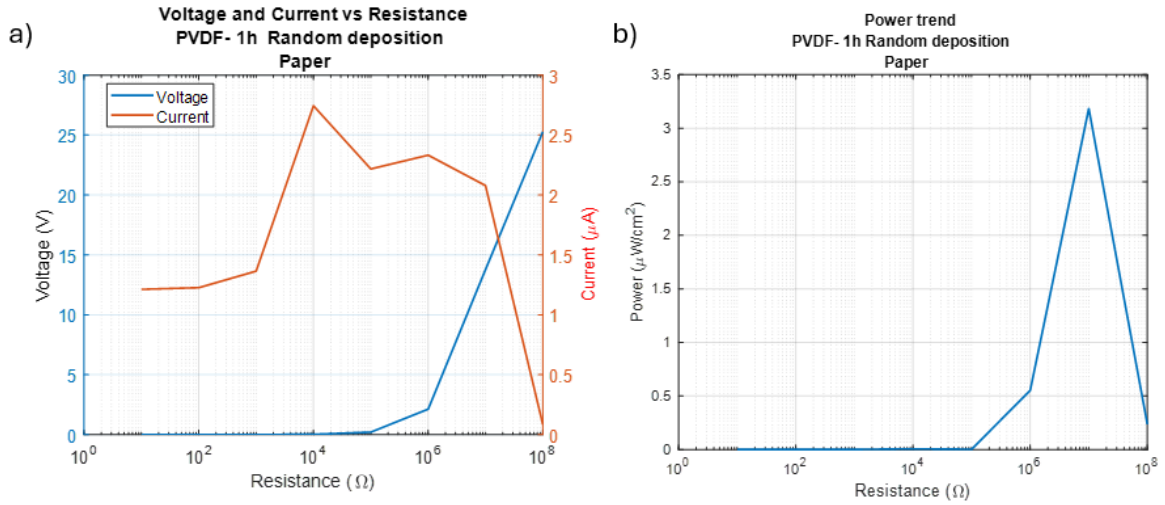

Figure 3.34 TENG output with resistors connection between paper and PVDF sample1_random: a) current and voltage trend; b) power curve

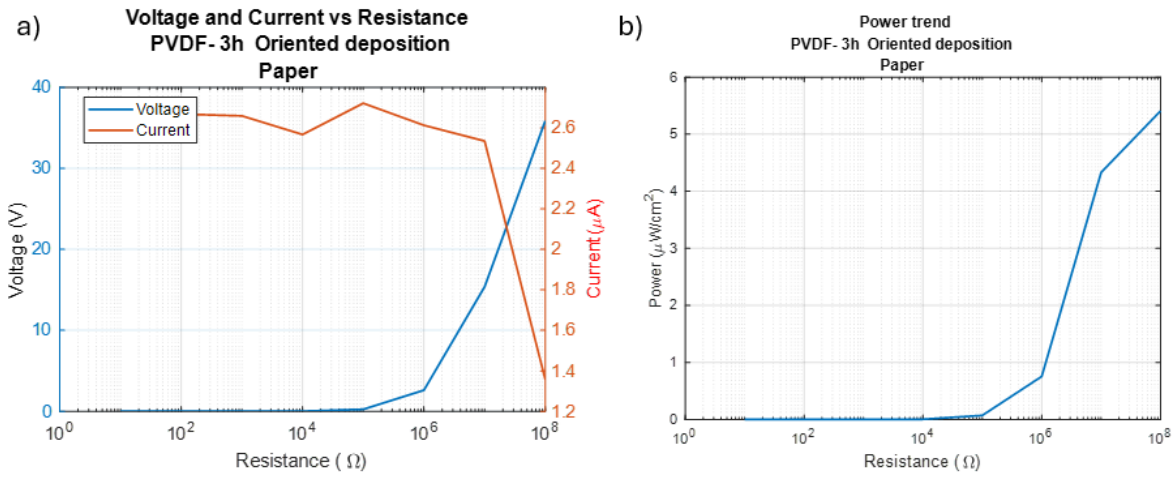

Figure 3.35 TENG output with resistors connection between paper and PVDF sample3: a) current and voltage trend; b) power curve

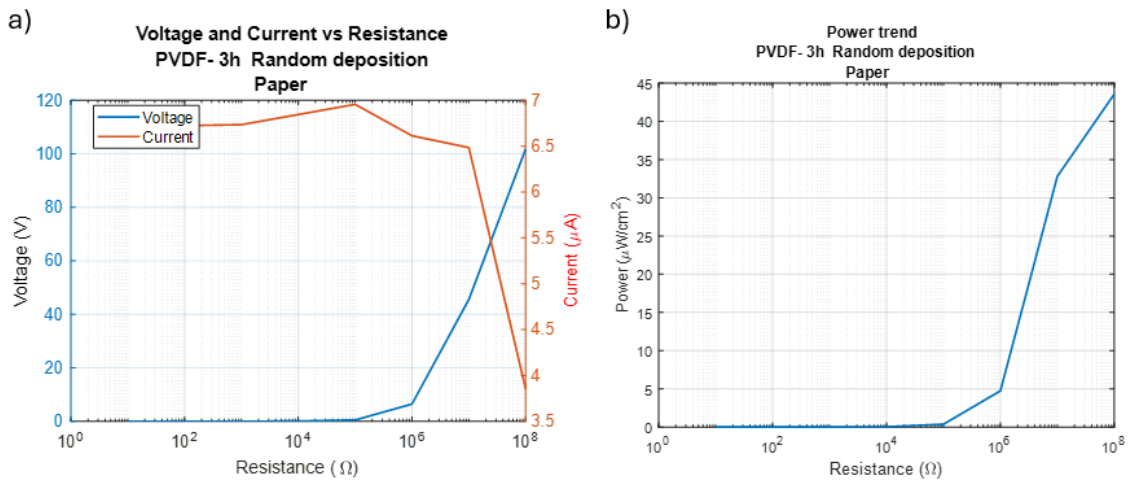

Figure 3.36 TENG output with resistors connection between paper and PVDF sample3_random: a) current and voltage trend; b) power curve

Power output for paper test with *sample3_random* PVDF are very higher. The previous analyses, however, showed a standard deviation that was too high, casting doubt on the consistency of these results.

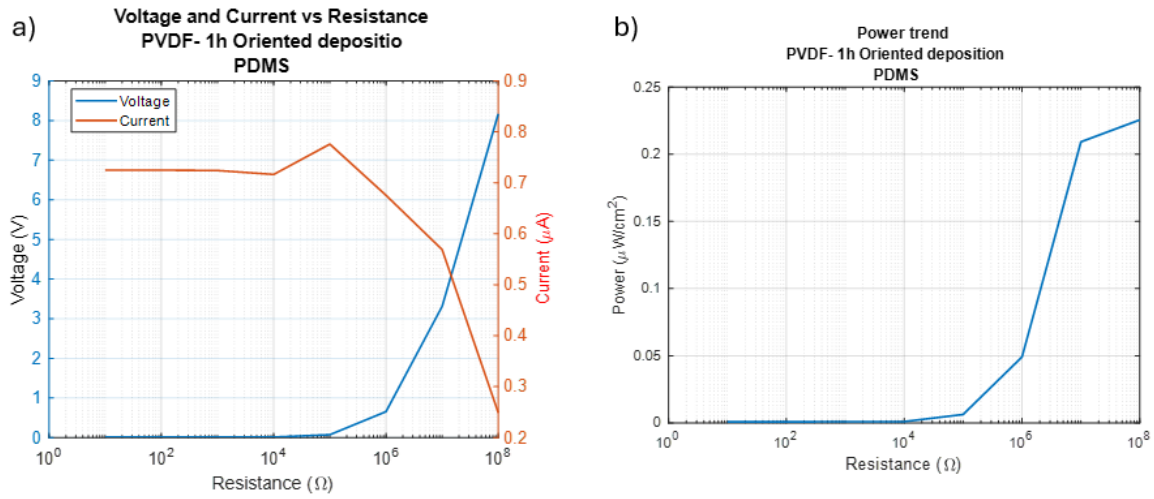

Figure 3.37 TENG output with resistors connection between PDMS and PVDF sample1: a) current and voltage trend; b) power curve

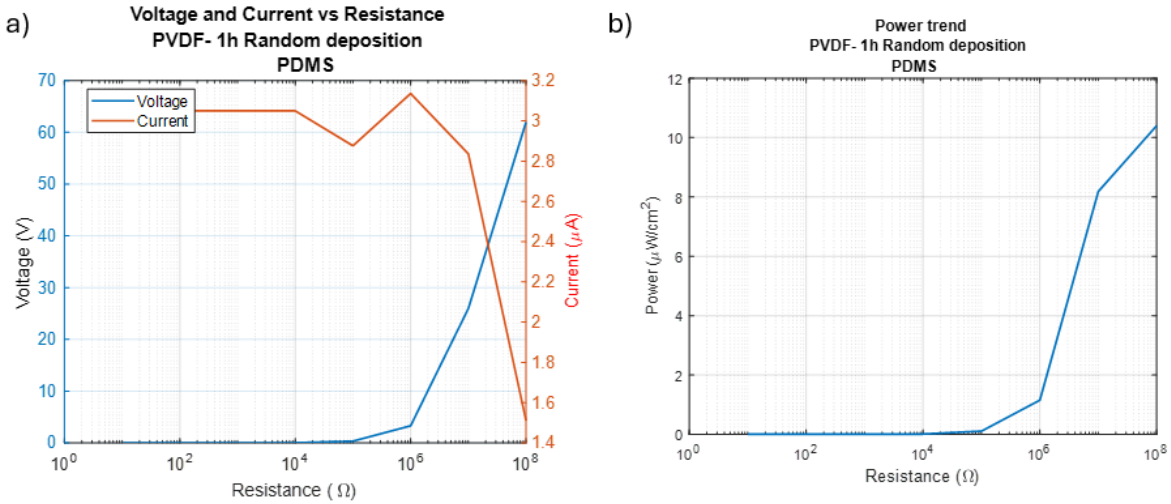

Figure 3.38 TENG output with resistors connection between PDMS and PVDF sample1_random: a) current and voltage trend; b) power curve

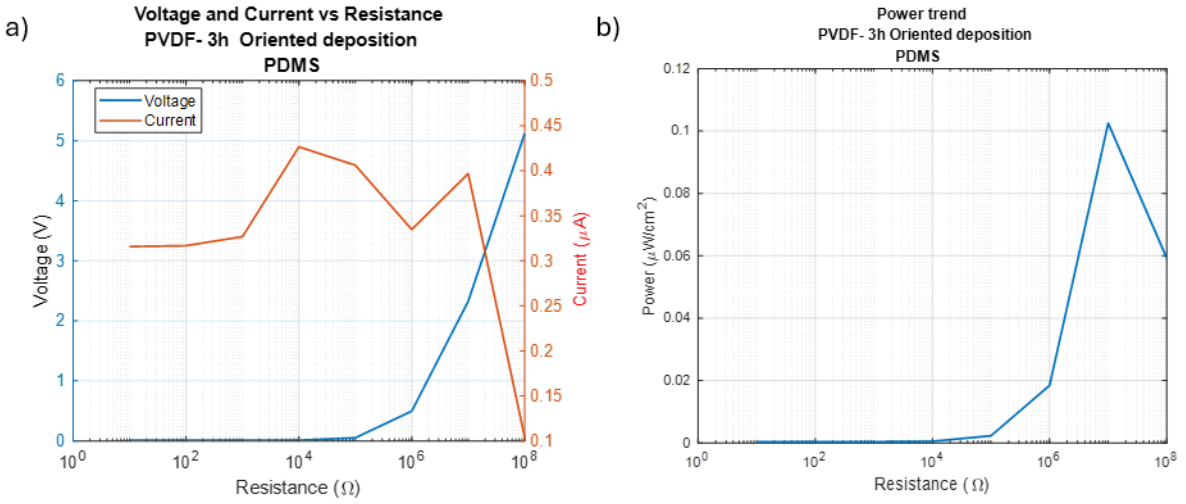

Figure 3.39 TENG output with resistors connection between PDMS and PVDF sample3: a) current and voltage trend; b) power curve

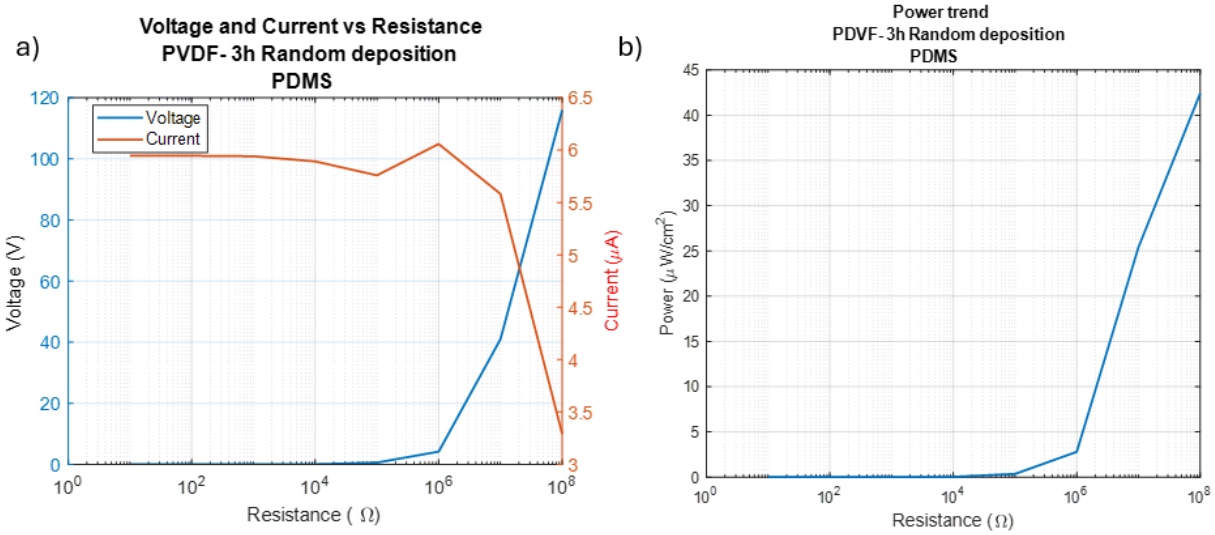

Figure 3.40 TENG output with resistors connection between PDMS and PVDF sample3_random: a) current and voltage trend; b) power curve

These latest graphs validate the promising role of PDMS as a tribomaterial within a TENG and at the same time they confirm the assessment of the PVDF fiber sample obtained with 3 hours of random deposition as the most efficient sample. We will now compare the results obtained from PET to evaluate any potential differences.

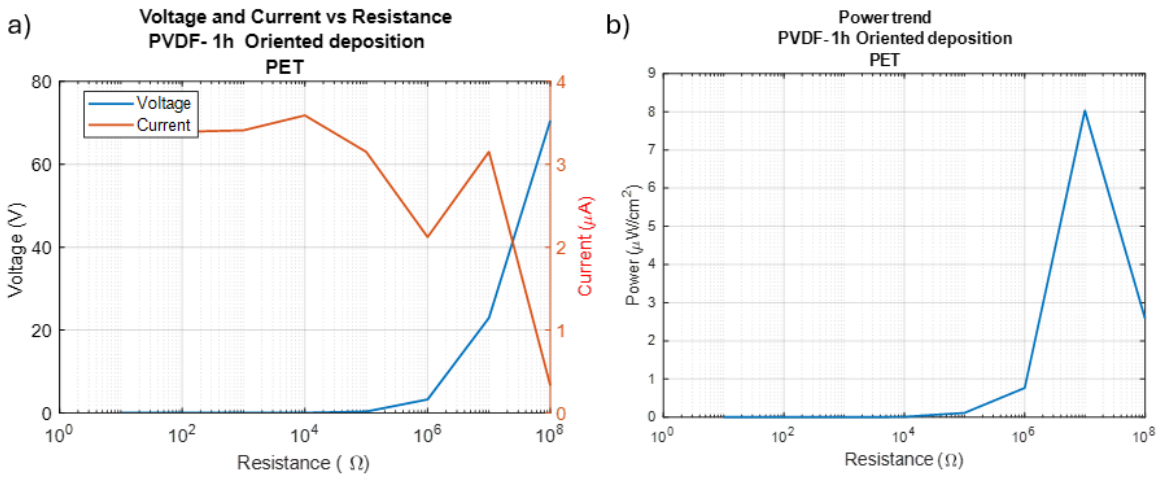

Figure 3.41 TENG output with resistors connection between PET and PVDF sample1: a) current and voltage trend; b) power curve

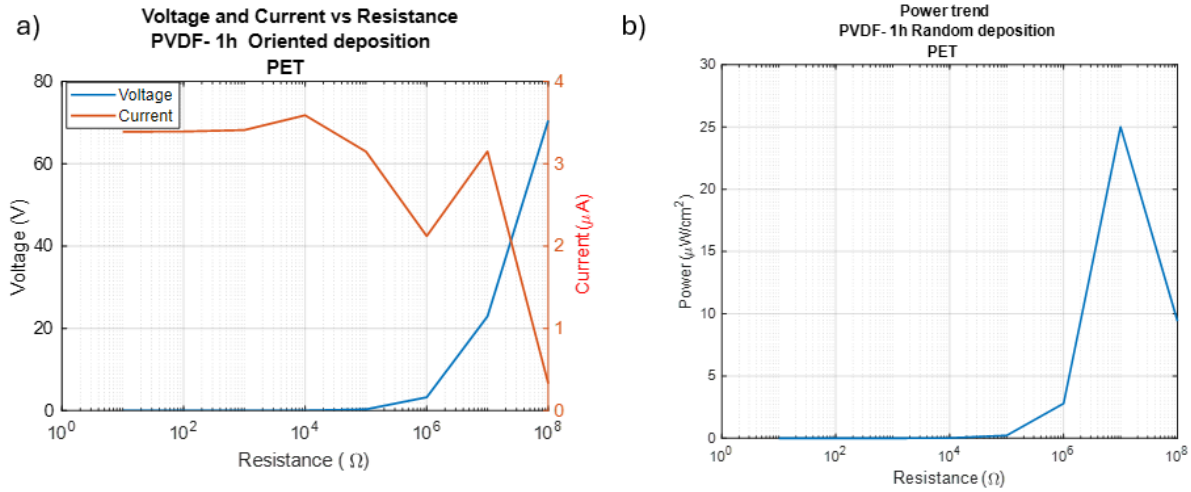

Figure 3.42 TENG output with resistors connection between PET and PVDF sample1_random: a) current and voltage trend; b) power curve

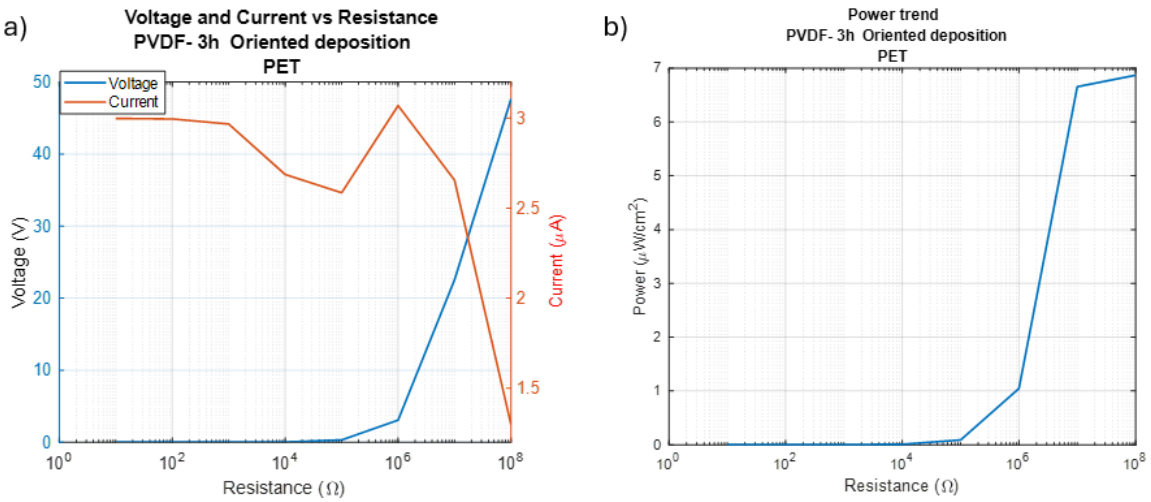

Figure 3.43 TENG output with resistors connection between PET and PVDF sample3: a) current and voltage trend; b) power curve

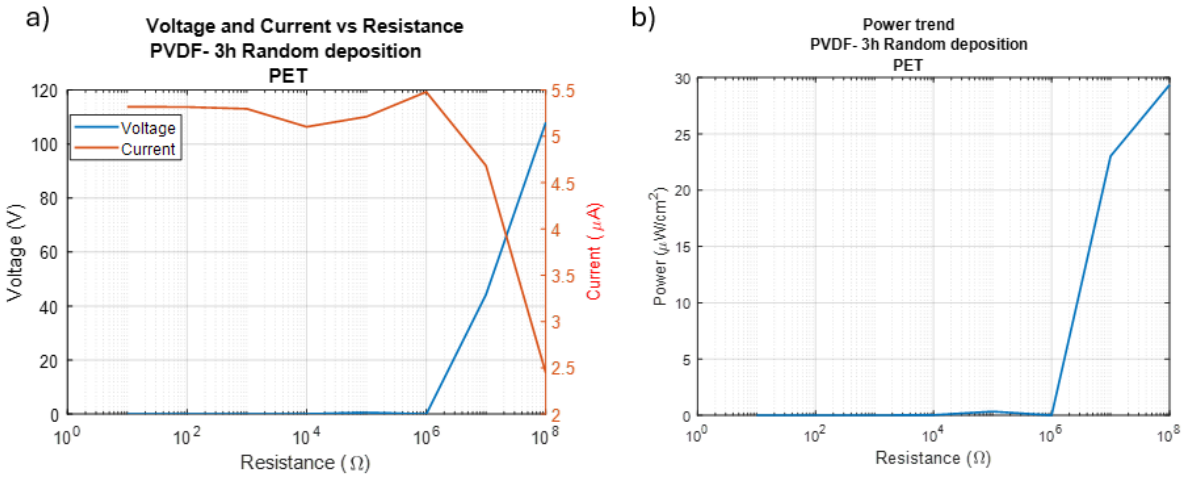

Figure 3.44 TENG output with resistors connection between PET and PVDF sample3_random: a) current and voltage trend; b) power curve

We can express the same concept for PET as we did for PDMS, affirming its role as a promising tribomaterial within a TENG system. This conclusion is supported by the comparative evaluation of its performance against other materials.
To gain a clearer understanding of the obtained values, the following tables were created, containing the maximum power values expressed in μW/cm^2 to make

this parameter more universal. These values were calculated at 5 Hz (*table 3.6*) and 7 Hz (*table 3.7*).

PVDF FIBERS MATERIALS	1H ORIENTED DEPOSITION	1H RANDOM DEPOSITION	3H ORIENTED DEPOSITION	3H RANDOM DEPOSITION
AL GRID	0.46	0.23	1.33	4.20
KAPTON	1.21	1.37	3.06	4.13
PAPER	1.35	3.18	5.40	43.58
PDMS	0.22	6.94	0.1	42.40
PET	8	25	6.90	29.30

Table 3.6 Power output values ($\mu W/cm^2$) calculated at 5 Hz for all PDVF samples

PVDF FIBERS MATERIALS	1H ORIENTED DEPOSITION	1H RANDOM DEPOSITION	3H ORIENTED DEPOSITION	3H RANDOM DEPOSITION
AL GRID	0.34	0.23	1.73	2.45
KAPTON	0.97	0.53	1.65	3.42
PAPER	1.20	3.20	1.35	30.65
PDMS	0.20	10.40	0.12	22.31
PET	18.57	18	8	48.51

Table 3.7 Power output values ($\mu W/cm^2$) calculated at 7 Hz for all PVDF samples

Additionally, in the literature, TENG performance is expressed as open-circuit voltage values and short-circuit current values. Ideally, these two cases are those obtained and discussed in the previous paragraph, where the TENG structure is directly connected to the electrometer.
In our case, however, these do not coincide. For completeness, the next tables will also include these values obtained at 5 Hz and 7 Hz and will be presented below. In particular, tables 3.8 and 3.9 will feature voltage and current at 5 Hz; tables 3.10 and 3.11 the same results but tested at 7 Hz.

V_{OC}	1H ORIENTED DEPOSITION	1H RANDOM DEPOSITION	3H ORIENTED DEPOSITION	3H RANDOM DEPOSITION
AL GRID	13.03	10.22	14.98	21.98
KAPTON	18.15	18.03	26.93	35.89
PAPER	22.17	25.28	35.87	101.87
PDMS	8.17	35.13	5.12	116
PET	70.54	46.41	47.66	108.01

Table 3.8 Voltage values (Volt) obtained in a similar open circuit condition (R = 100 MΩ)

i_{sc}	1H ORIENTED DEPOSITION	1H RANDOM DEPOSITION	3H ORIENTED DEPOSITION	3H RANDOM DEPOSITION
AL GRID	0.90	0.76	1.04	1.83
KAPTON	0.94	1.39	2.11	1.85
PAPER	1.54	1.21	2.67	6.73
PDMS	0.72	2.75	0.31	5.94
PET	3.39	3.38	3.00	5.32

Table 3.9 Current values (expressed in μA) obtained in short circuit (R = 10 Ω)

Now, we will show same values at 7 Hz; this is another way to demonstrate the similarity of the outputs with such a small frequency difference.

V_{oc}	1H ORIENTED DEPOSITION	1H RANDOM DEPOSITION	3H ORIENTED DEPOSITION	3H RANDOM DEPOSITION
AL GRID	9.70	8.74	27.66	21.90
KAPTON	17.00	11.87	25.32	30.26
PAPER	17.96	28.28	28.80	105.25
PDMS	7.50	61.98	3.75	83.90
PET	73.47	73.17	39.40	117.95

Table 3.10 Voltage values (Volt) obtained in a similar open circuit condition (R = 100 MΩ)

i_{sc}	1H ORIENTED DEPOSITION	1H RANDOM DEPOSITION	3H ORIENTED DEPOSITION	3H RANDOM DEPOSITION
AL GRID	1.17	0.56	0.99	1.63
KAPTON	0.73	1.20	1.07	2.00
PAPER	0.87	2.37	0.68	5.20
PDMS	0.64	3.05	0.49	3.38
PET	3.82	3.68	3.43	7.01

Table 3.11 Current values (expressed in μA) obtained in short circuit (R = 10 Ω)

To summarize the results obtained and characterize the performance of the tested material combinations, a triboelectric serie was created based on peak-to-peak voltage values using the random PVDF sample 3 (*figure 3.45*) in open circuit conditions at 100 MΩ. This choice is related to the higher outputs obtained with this specific sample.

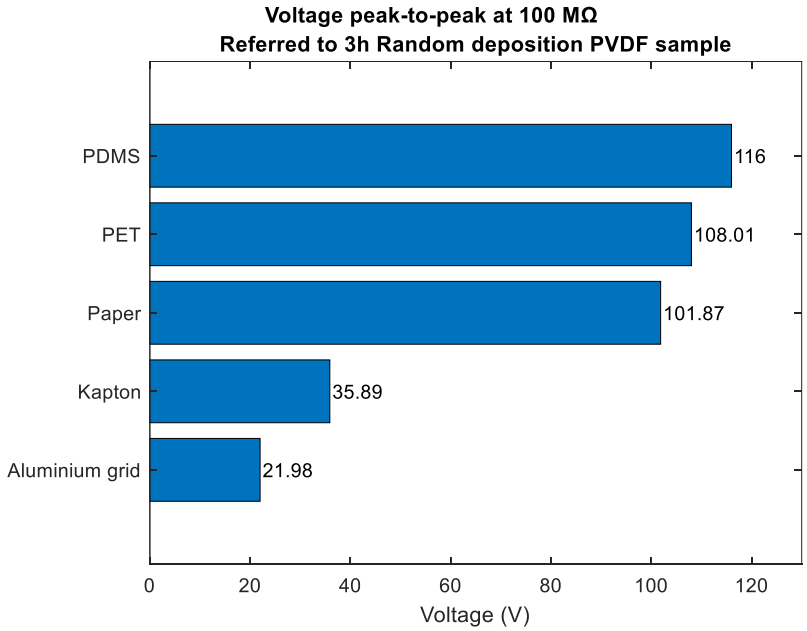

Figure 3.45 Producted triboelectric series with tested materials in open circuit conditions (R = 100 MΩ) expressed in terms of voltage peak to peak values

3.2.3 Energy output

Observing the previous graphs and tables, we can easily characterize PET and PDMS as the most promising tribomaterials.
Two structures were examined for calculating the energy that can be generated by a TENG device:

- 3 hours oriented deposition PDVF sample associated with PDMS
- 1 hour random deposition PVDF sample tested with PET

The measurements considered to define the most performant samples are the open-circuit voltage values and the closed-circuit current values obtained in the absence of connection to the resistors.
The purpose of these measurements is to connect the structure to a breadboard with a diode bridge and connect various capacitors to allow for charging. The ultimate goal is to evaluate how many LEDs can be lit with a certain amount of charge stored in the capacitor.
Next figures will show how the voltage varies with changes in the capacitance value to which the structure is connected. The connection between the samples and the electrometer for recording the measurements was maintained for about 2 hours for each sample until the voltage saturation was reached.
Figure 3.46 is about PDMS responses while, figure 3.47 exhibit PET trends.

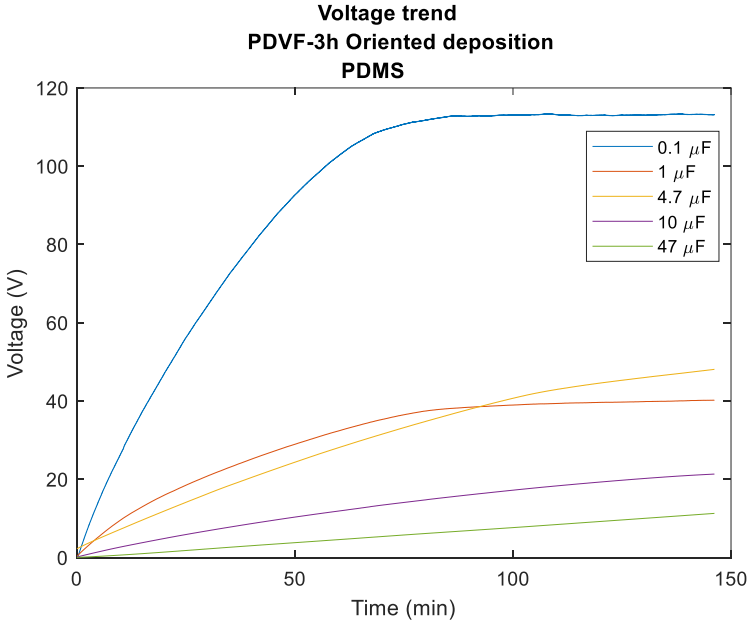

Figure 3.46 PDMS-sample3 PVDF voltage trend at various capacitor values

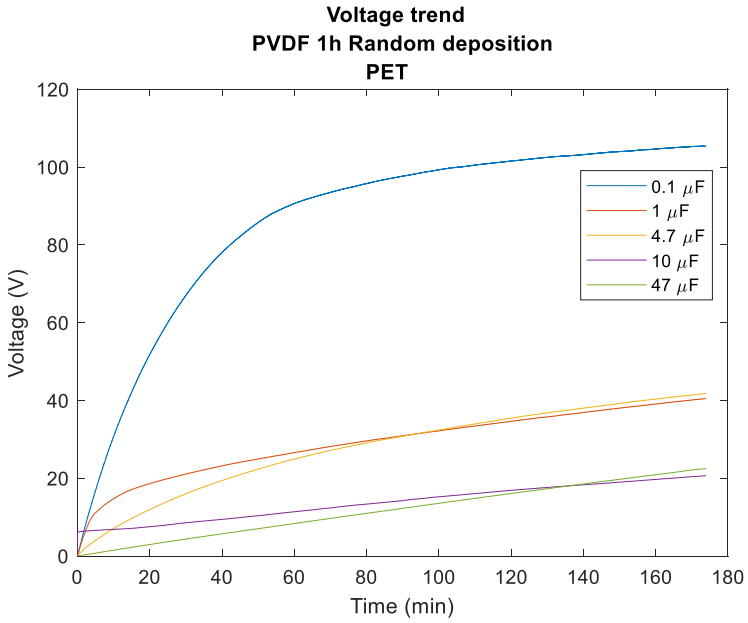

Figure 3.47 PET-sample1_random PVDF voltage trend at various capacitor values

The trend of these graphs is explained by the relationship between voltage and capacitance:

$$V = \frac{Q}{C} \tag{3.4}$$

By equation 3.3 we can also calculate the amount of charge transferred Q.
Next figures will show voltage and charge trend related to capacity values, figure 3.48 for PDMS measurements, figure 3.49 for the PET ones.

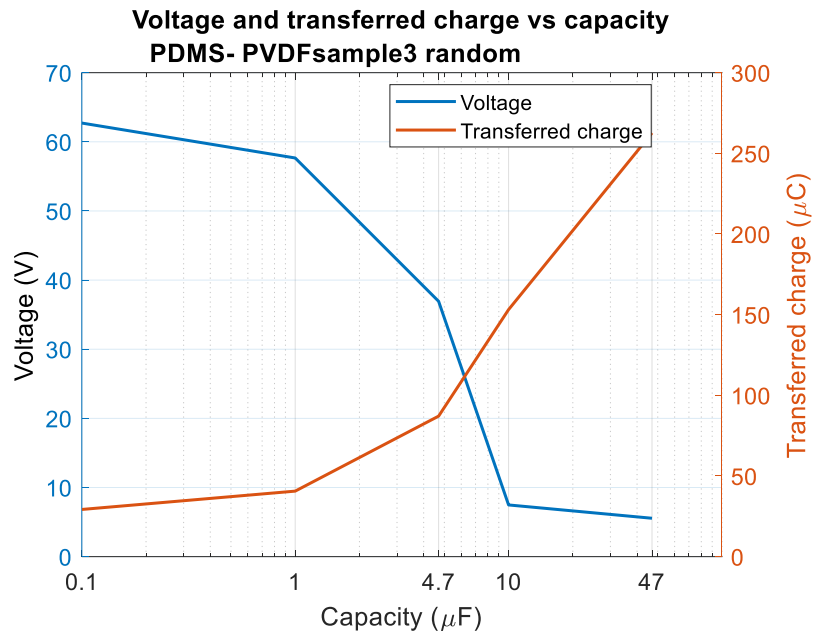

Figure 3.48 Voltage and transferred charge trends for PVDF sample3_random and PMDS at various capacitors value

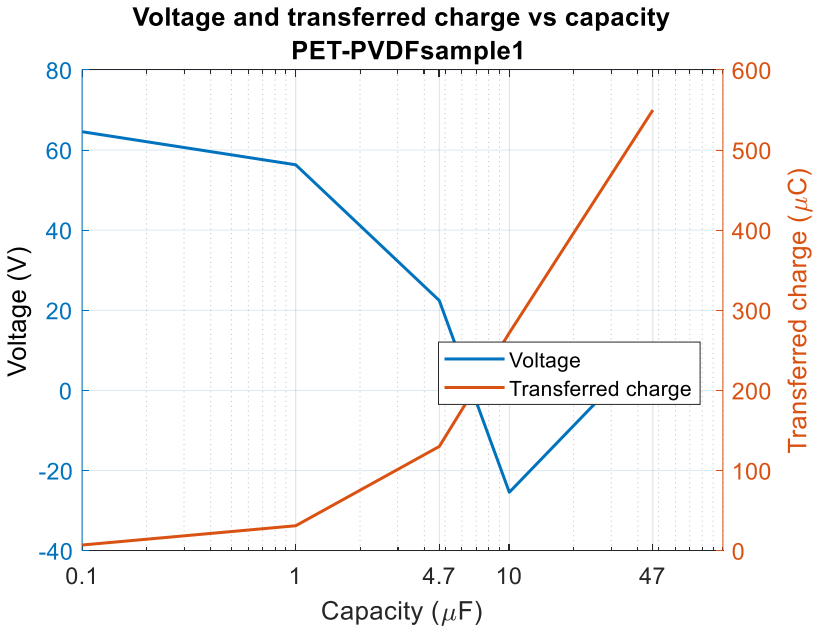

Figure 3.49 Voltage and transferred charge trends for PVDF sample1 and PET at various capacitors value

Trough the following relation we can obtain the generated energy for these two configurations:

$$E = \frac{1}{2} C V^2 \tag{3.5}$$

Figures 3.50 and 3.51 will present energy output as the capacitance increases, respectively for PDMS and PET samples.

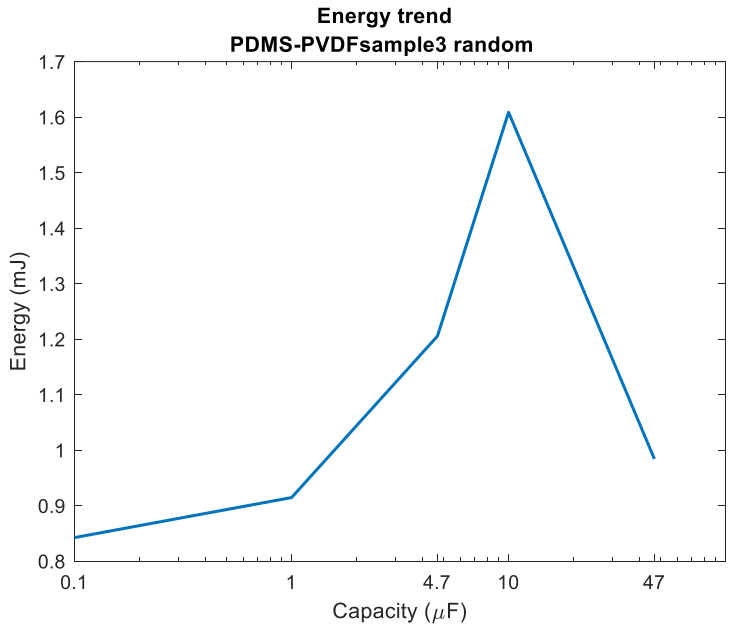

Figure 3.50 Energy output for PDMS-PVDF sample 3 random TENG calculated at various capacitor values

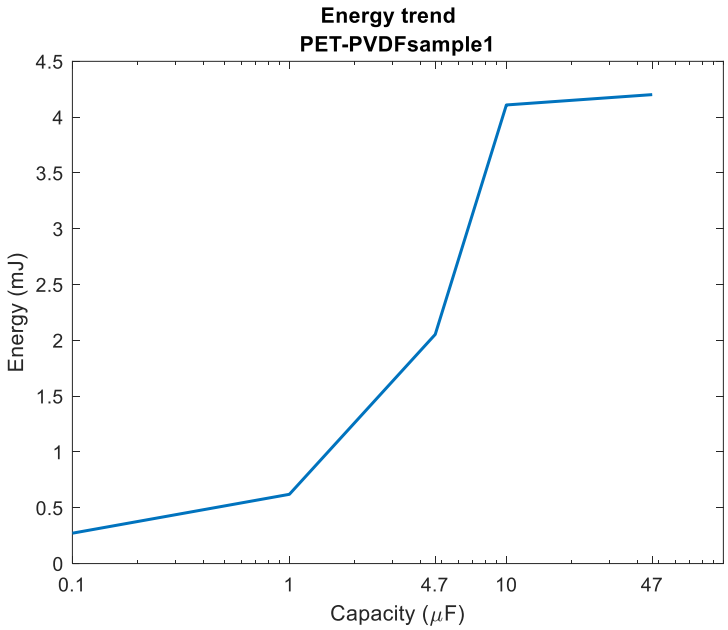

Figure 3.51 Energy output for PET-PVDF sample1 TENG calculated at various capacitor values

The energy graphs illustrate how the energy generated by the TENG device varies with different parameters, such as capacitance. These graphs are useful for understanding the relationship between energy storage and capacitance values, helping to optimize the design of energy-harvesting systems.

3.3 ARAMID SAMPLES

Triboelectric characterizations on aramid samples were performed with the same setup used for the PVDF samples. Among all the aramid samples produced with different techniques, explained in the previous chapter, those obtained through dip coating were excluded from testing due to the lack of uniformity in the coating.

Tests were conducted both on meta-ANF and para-ANF obtained by filtration and spray coating with one and two layers. The set-up parameters involve only two different frequency values (5 Hz with 10 millimeters of displacement and 7 Hz with 7 mm of displacement) based on the hypotheses formulated from tests conducted at 2 Hz on the PVDF samples.

Voltage and current trend in shown in figure 3.52 in terms of values peak to peak and tested, purely for ease of representation, on PDMS and 2 layers of para aramid nanofibers sample obtained by spray coating. Also in this case, output trends are always the same; the difference lies in the values achieved.

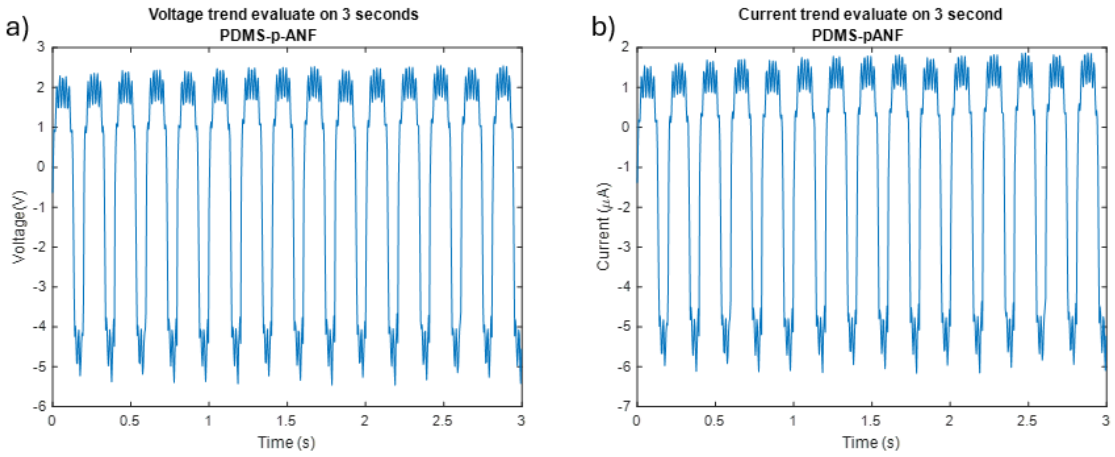

Figure 3.52 Peak to peak values obtained with PDMS and p-ANF after two layers of spray coating at 5 Hz: a) voltage; b) current

Overall, six aramid samples were tested with three different materials: PET, PDMS, and nanometric aluminum grid.
Following figures will show comparison histograms of different aramid samples relative to the other materials.
In detail, in figures 3.53 and 3.54 there is a comparison of filtration-made para and meta aramid nanofibers for, respectively, voltage and current.

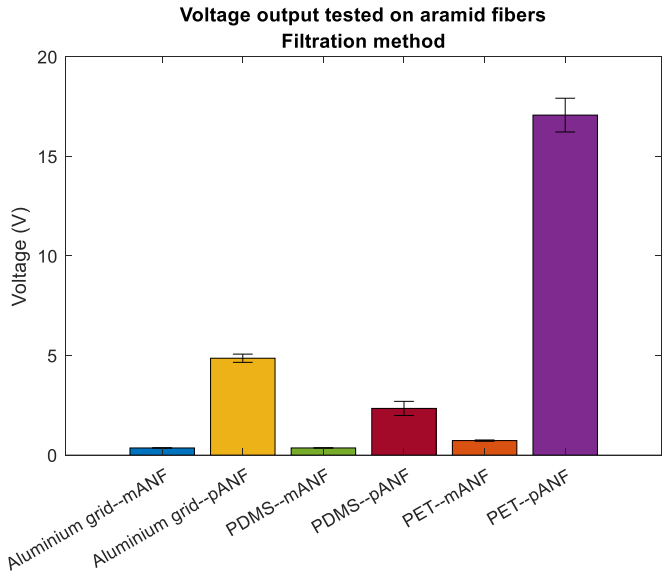

Figure 3.53 Histogram for voltage values comparison between aramid nanofibers samples obtained by filtration and aluminum grid, PET, PDMS tested at 5 Hz

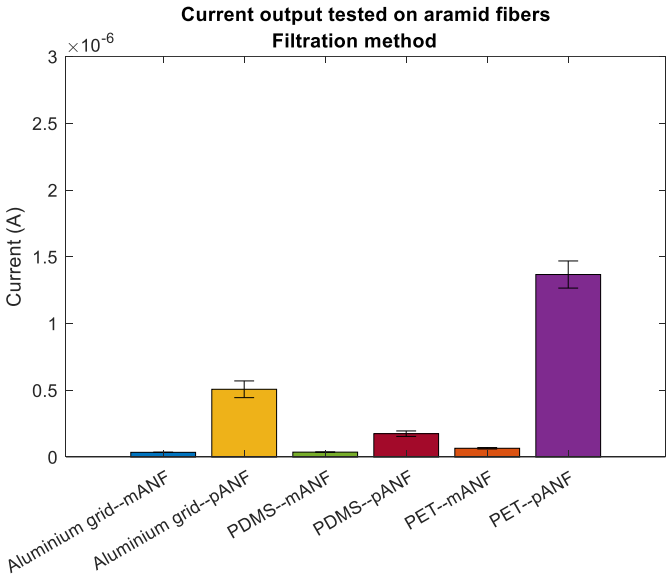

Figure 3.54 Histogram for current values comparison between aramid nanofibers samples obtained by filtration and aluminum grid, PET, PDMS tested at 5 Hz

Based on these figures we could assume that para aramid nanofibers deposited on metalized PTFE membrane through filtration present higher triboelectric properties. In particular, PET results as the most favorable material.
We know that meta and para aramid conformations differ only in atoms present in the chain. But, before attributing the increase in triboelectric properties to the different chain, further tests should be conducted on samples obtained by different methods.
The following figures (*figures 3.55 and 3.56*) will show the same histograms, but for the meta and para aramid samples obtained with spray coating (1 and 2 layers), combined with the three materials.

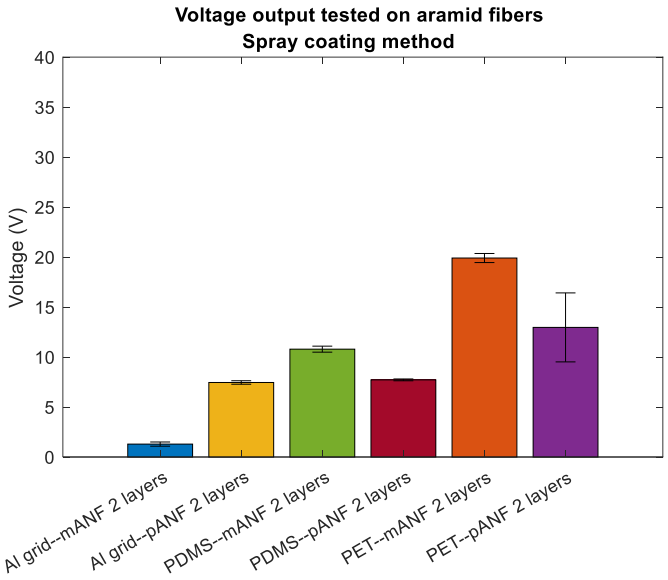

Figure 3.55 Histogram for voltage output comparison between aramid nanofibers samples obtained by spray coating and aluminum grid, PET, PDMS tested at 5 Hz

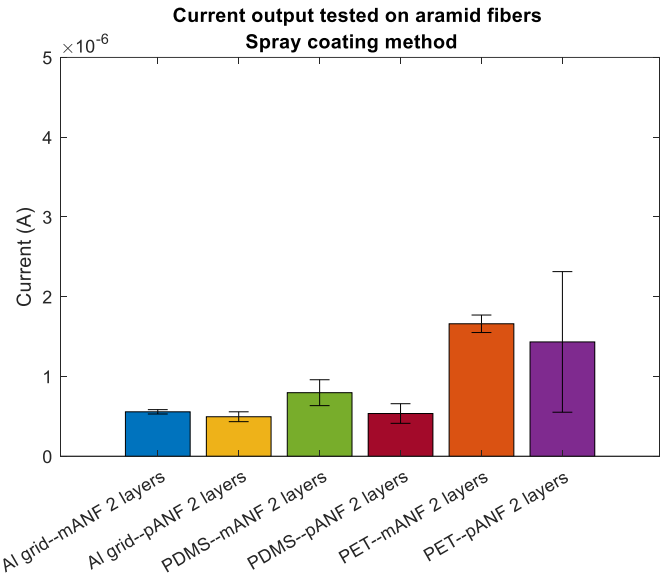

Figure 3.56 Histogram for current output comparison between aramid nanofibers samples obtained by spray coating and aluminum grid, PET, PDMS tested at 5 Hz

Also, spray coating aramid fibers results confirm good triboelectric properties of para-ANF. Despite this, in this case, we observe higher values even for the meta fiber samples. PET sample, tested with 2 layers of meta-ANF by spray coating reaches the maximum output values.

As mentioned earlier, the goal of the study is to identify the ideal material combination. In this case, the ideal aramid sample varies depending on the deposition technique used. Different deposition methods, such as spray coating, dip coating, or others, can lead to different structural properties in the aramid fibers, influencing their performance in applications like TENG ones.

Regarding filtration, para-aramid fibers provide the best results. However, looking at the last two figures with the samples obtained via spray coating, the best performance is attributed to the meta-aramid fiber sample covered with two layers. In this case, while the two-layered para-aramid fiber samples also yield good results, the high standard deviation shown in the figure reduces the reproducibility of these results. This suggests that although para-aramid fibers may offer high performance, their consistency is affected by the variability introduced during the coating process.

Next step involves evaluating the comparison between “second” materials. This comparison will help identify how the choice of second material impacts the

overall performance, particularly when combined with different types of aramid fibers, such as meta and para-aramid.
Figures 3.57 adn 3.58 will show this results for aluminum grid; figures 3.59 and 3.60 for PDMS and the last ones, figures 3.60 and 3.61 shows PET output (first one is about voltage, second one about current).

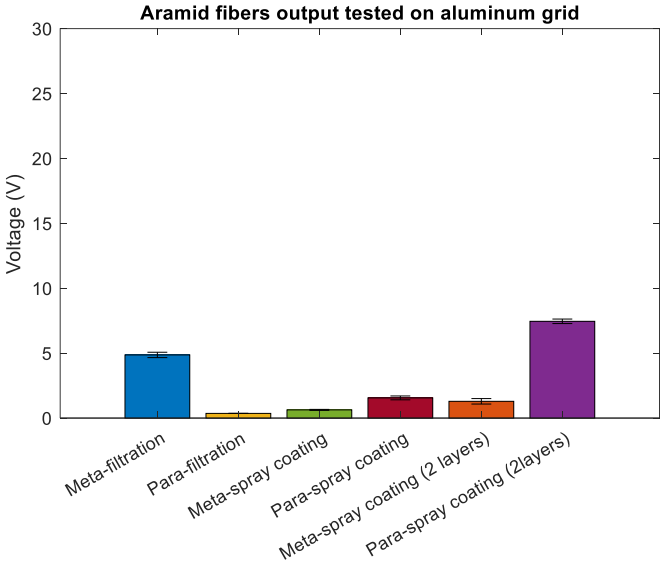

Figure 3. 57 Aluminum nanometric grid voltage ouput for all aramid samples tested at 5 Hz

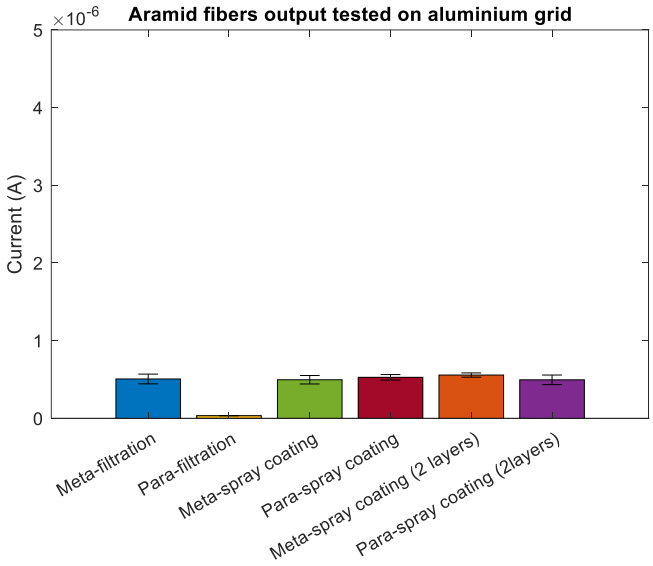

Figure 3.58 Aluminum nanometric grid current ouput for all aramid samples tested at 5 Hz

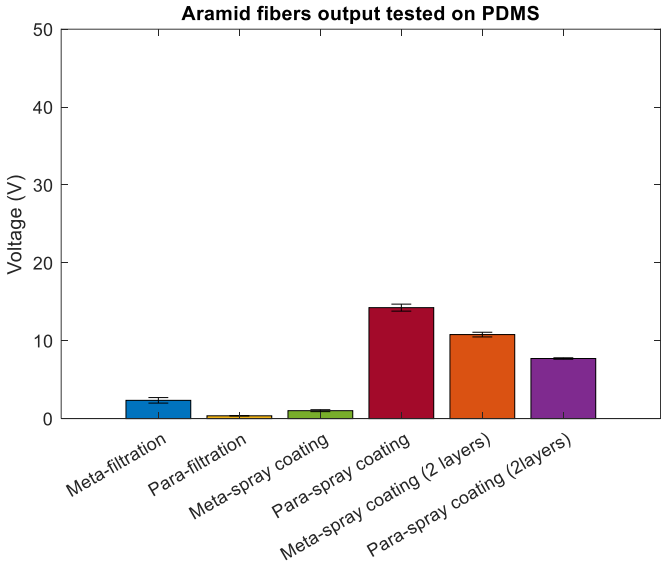

Figure 3.59 PDMS voltage ouput for all aramid samples tested at 5 Hz

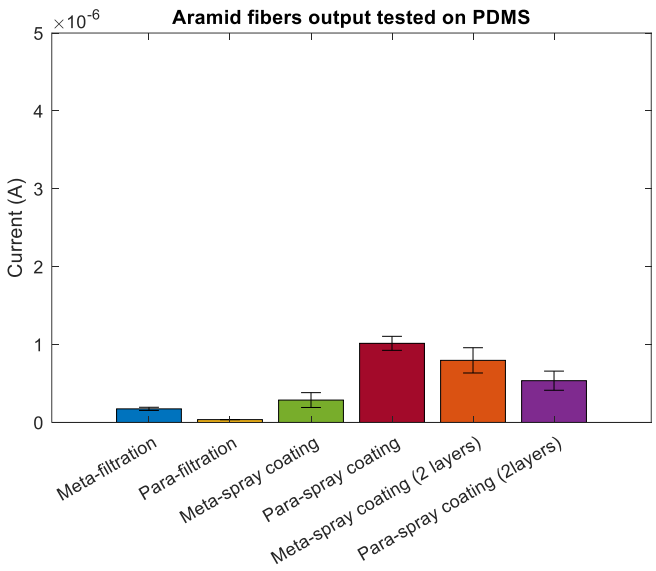

Figure 3.60 PDMS current ouput for all aramid samples tested at 5 Hz

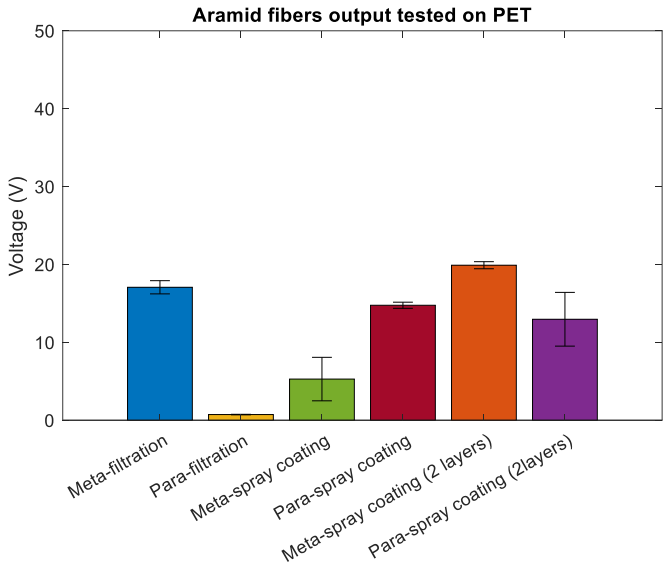

Figure 3.61 PET voltage ouput for all aramid samples tested at 5 Hz

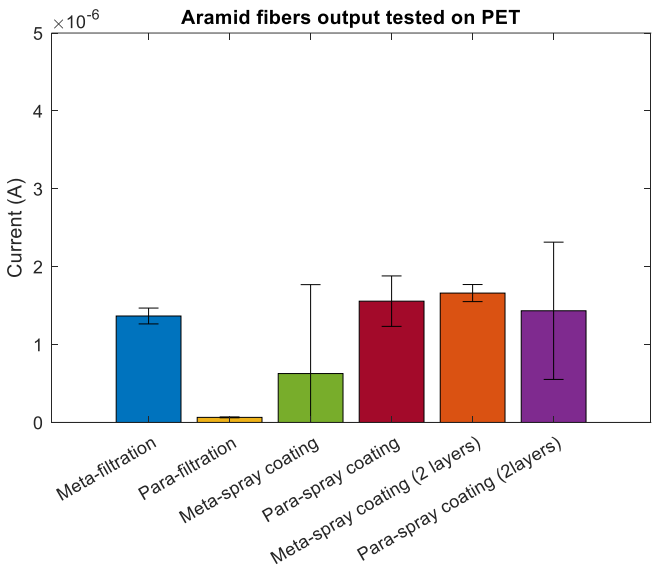

Figure 3.62 PET current ouput for all aramid samples tested at 5 Hz

At this point, having analyzed the results from the latest figures, we can assume that we reach the better results when tests are made with PET and p-ANF deposited through spray coating for two layers. But, due to the substantial standard deviation values we can consider PDMS and same p-ANF sample as the best combination.

3.4 ARAMID FIBERS AND PVDF FIBERS CHARACTERIZATIONS

In order to create an all-fiber TENG structure latest characterization involved combination between all aramid nanofibers samples with all the PVDF ones. Initially, to verify the actual deposition of fibers on the metallized PTFE membrane, tests were conducted using aramid samples obtained through filtration, combined with the previously mentioned PVDF samples. Specifically, the first tests were carried out on both para- and meta-aramid fiber samples, as well as on the untreated metallized membrane, which was used as a control (blank). The aim was to analyze the results obtained; differing results would have confirmed a surface variation and, consequently, the presence of fibers.
Figures 3.63 and 3.64 will show this comparison in a bar graph in terms of voltage (figure 3.63) and current (3.64) tested on 3 hours random deposition PVDF sample and filtration-made aramid nanofibers samples.

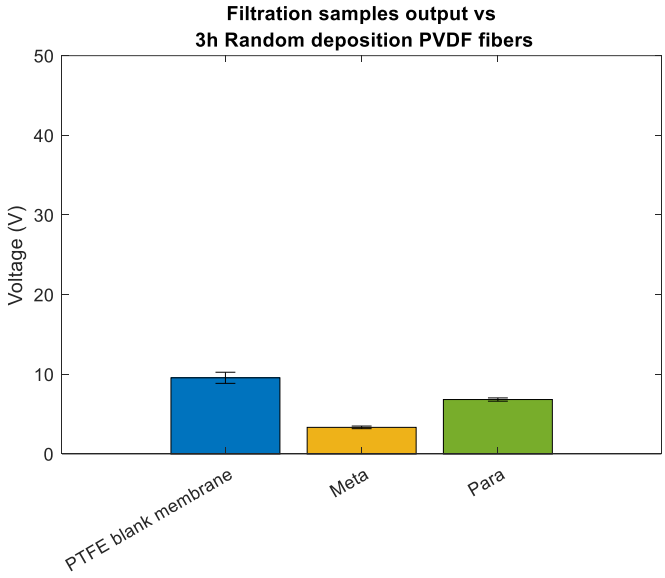

Figure 3.63 Control tests for fiber deposition. Performed on sample3_random and membranes subjected to filtration, tested at 5 Hz and under open-circuit conditions for voltage measurement

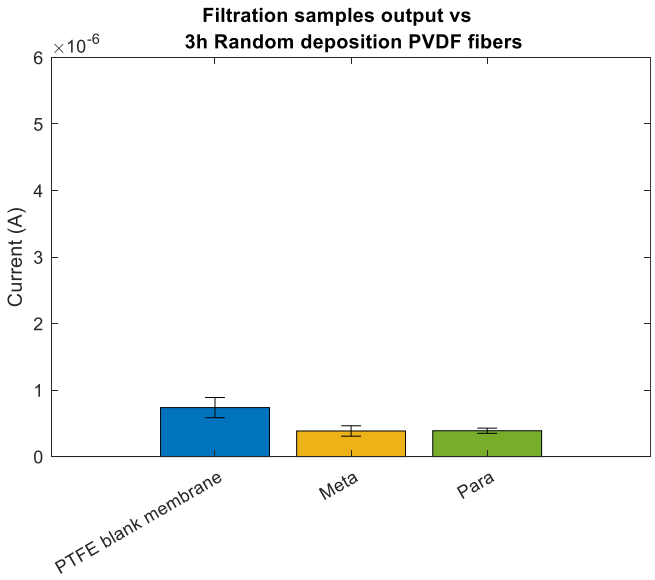

Figure 3.64 Control tests for fiber deposition. Performed on PVDF sample3_random and membranes subjected to filtration, tested at 5 Hz and under short-circuit conditions for current measurement

The values obtained, although lower than those of the control membrane, differ based on the type of fibers used (both in terms of voltage and current).
Likewise, this results are expressed as the same way as the PVDF ones. That consist on the mean of every peak to peak value and its standard deviation, calculate using the formula expressed in equation 3.
To provide further evidence, the next figures (*figure 3.65* for voltage output and *figure 3.66* for the current one) will show the same tests performed on sample3 PVDF fibers with oriented deposition.

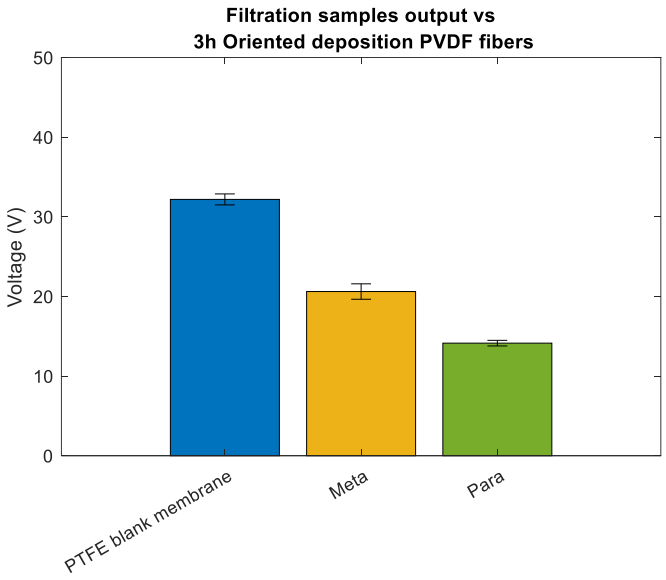

Figure 3.65 Control tests for fiber deposition. Performed on PVDF sample3 and membranes subjected to filtration, tested at 5 Hz and under open-circuit conditions for voltage measurement

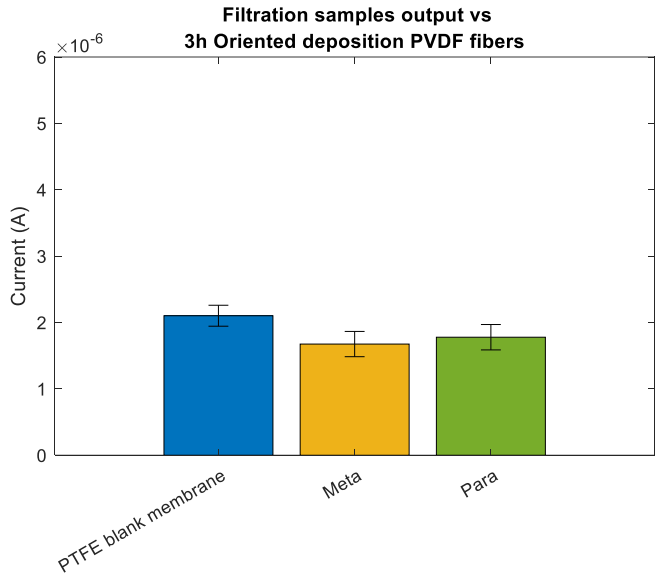

Figure 3.66 Control tests for fiber deposition. Performed on PVDF sample3 and membranes subjected to filtration, tested at 5 Hz and under short-circuit conditions for current measurement

The PVDF samples electrospun with an ordered orientation, compared to those with random orientation, generate higher triboelectric outputs when tested with other fibrous materials. To ensure this, we have to analyze and compare the results obtained with the aramid membranes produced by spray coating.
For the characterization of aramid fibers with PVDF, we also need to identify the optimal combination of materials. To achieve this, we will investigate the effect of various aramid samples as well as individual PVDF samples by comparing the peak-to-peak values achieved.
In the first four graphs (*figures from 3.67 to 3.70*)we will evaluate which of the four tested PVDF fiber morphologies is best suited for triboelectric applications with aramid.

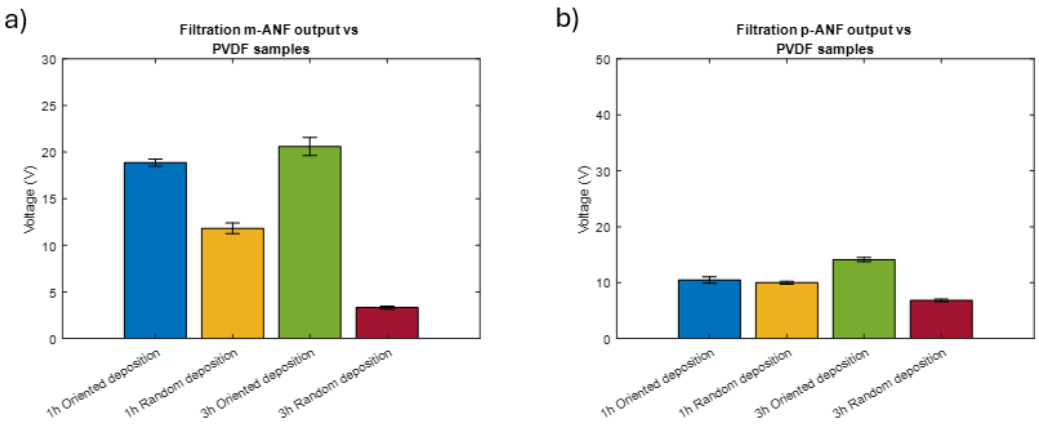

Figure 3.67 Voltage output of a) meta aramid nanofibers filtration-made; b) para aramid nanofibers filtration-made in relation to PVDF samples varying fiber morphologies at 5 Hz

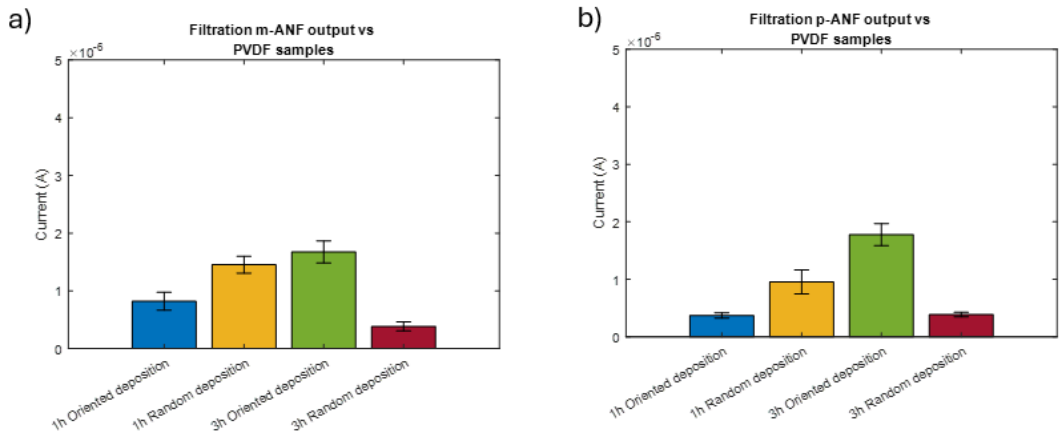

Figure 3.68 Current output of a) meta aramid nanofibers filtration-made; b) para aramid nanofibers filtration-made in relation to PVDF samples varying fiber morphologies at 5 Hz

Overall, for filtration aramid samples the best choice could be the 3 hours oriented deposition PDVF sample, both for voltage and current.
Now we will examine triboelectric properties of fiber deposited via spray coating on a copper electrode (figures 3.69)

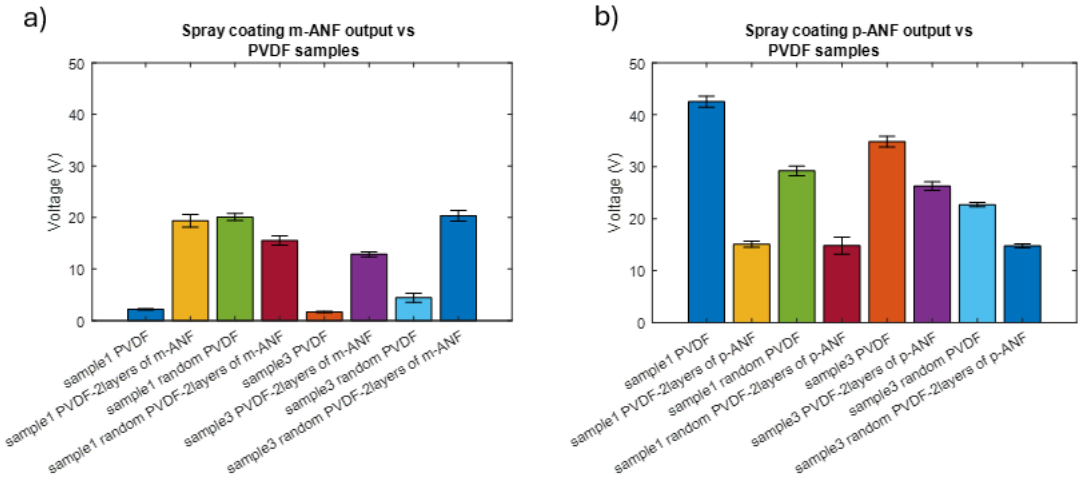

Figure 3.69 Voltage output values obtained from spray coating aramid nanofibers samples with both 1 and 2 layers of spraying at 5 Hz: a) meta-ANF; b) p-ANF. All aramid samples are referrered to all PDVF samples

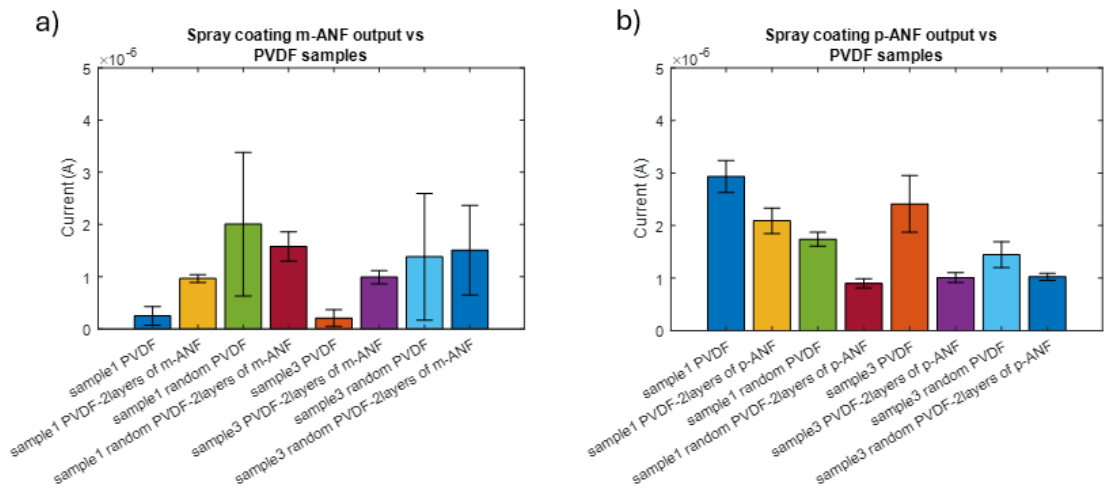

Figure 3.70 Current output values obtained from spray coating aramid nanofibers samples with both 1 and 2 layers of spraying at 5 Hz: a) meta-ANF; b) p-ANF. All aramid samples are referrered to all PDVF samples

To provide a clearer overall view of the precise output values achieved, Tables 3.1 and 3.2 will follow, containing the maximum peak-to-peak values considered for voltage and current, respectively.

PVDF samples:

Maximum V_{pp} (V)	*1h Oriented deposition*	*1h Random deposition*	*3h Oriented deposition*	*3h Random deposition*
mANF- filtration	18.87	11.82	20.60	3.33
pANF-filtration	10.46	9.97	14.12	6.83
mANF-spray coating	2.18	20.1	1.67	4.43
pANF-spray coating	42.5	29,2	34.82	22.68
mANF-spray coating (2layers)	19.37	15.54	12.86	20.35
pANF-spray coating (2layers)	15	14.8	26.26	14.76

Table 3.12 Summary of voltage output calculate between PDVF and aramid fibers tested at 5 Hz and expressed in Volt as the maximum value of every peak to peak value

PVDF samples:

Maximum i_{pp} (μA)	*1h Oriented deposition*	*1h Random deposition*	*3h Oriented deposition*	*3h Random deposition*
mANF- filtration	0.82	1.45	1.67	0.38
pANF-filtration	0.37	0.96	1.78	0.39
mANF-spray coating	0.25	2	0.21	1.38
pANF-spray coating	2.9	1.74	2.41	1.44
mANF-spray coating (2layers)	0.97	1.58	1	1.5
pANF-spray coating (2layers)	2.1	0.9	1.01	1.02

Table 3.13 Summary of current output calculate between PDVF and aramid fibers tested at 5 Hz and expressed in micro Ampere as the maximum value of every peak to peak value

As a general trend in the outputs produced, we can observe that the PVDF sample obtained with 3 hours of oriented deposition almost consistently, achieves the highest values compared to the other PVDF samples. Additionally, it can be stated that when fibers are deposited via spray coating, particularly in two distinct layers, higher values are achieved.

4 CONCLUSIONS

The aim of this work was to test the triboelectric properties of selected materials, first combined with PVDF fibers and subsequently with aramid fibers. A triboelectric series was developed to allow for a more in-depth analysis of the properties of the most promising materials (*figure 4.1*).

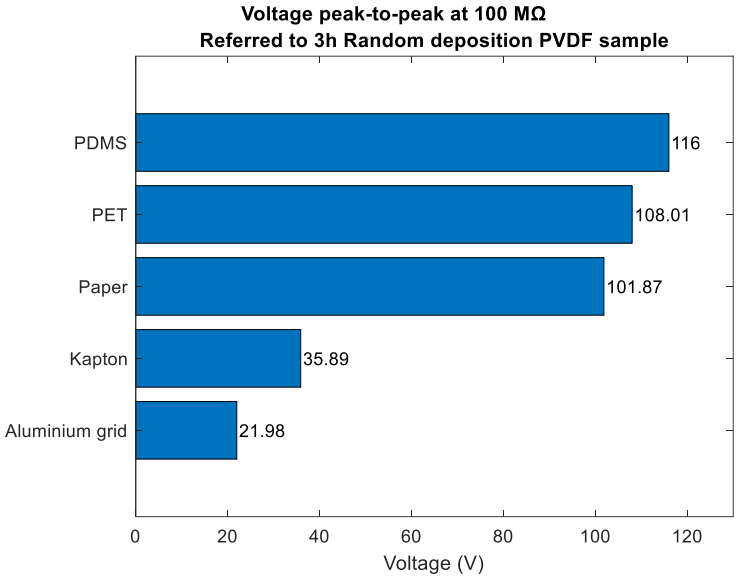

Figure 4.1 Produced triboelectric series, ordered from top to bottom, starting with the most performant material to the least performant.

PDMS and PET achieved the best results in all the tests conducted. Notably, there was a significant increase in output when these materials were combined with the PVDF fiber sample obtained through 5 hours of random deposition. Increasing the deposition time increases the amount of material present on the sample and, consequently, the quantity of beta-phase polarized PVDF, which imparts its triboelectric properties.

Referring to Table 1.1, which presents the outputs of various materials reported in the literature, we can affirm the role attributed to PDMS. The maximum power values obtained, expressed in $\mu W/cm^2$, are indeed comparable. The same can also be said for PET and for paper.

From the tests with capacitors, we highlighted the ability of our structure to charge capacitors up to a value of 47 μF, achieving energy production of up to 1.6 mJ with PDMS and 4.2 mJ in tests using PET.

The next step was to examine the triboelectric properties of aramid fibers, which are not widely discussed in the literature. This was done to analyze both the effect of a second fibrous material combined with membrane-form materials and to test the effect of an entire fiber-based structure.

Analyzing the ultimate goal of this type of nanogenerator,making them wearable, the use of Kevlar (para-aramid nanofibers) proves particularly advantageous, as it is already used in textiles as an integration material according to the literature. To summarize the results described in the previous chapter, it was indeed the para-aramid fiber samples that achieved the highest results, particularly those coated with a larger amount of fibers (2 layers of spray coating).

At this point, we can certainly affirm that, with the same active contact area (3x3 cm^2), applied force, frequency, and materials, the output values increase as the amount of fiber material deposited on the electrode (in this case, copper) increases.

The next challenges to tackle certainly involve increasing the PVDF fiber deposition times, preferably with random deposition, and exploring new fiber deposition techniques for aramid to enhance its effectiveness. One could also consider formulating new solutions that are more concentrated in order to contain a larger quantity of fibers for deposition.

5 REFERENCES

[1] E. T. Sayed *et al.*, “Renewable Energy and Energy Storage Systems,” Feb. 01, 2023, *MDPI*. doi: 10.3390/en16031415.

[2] V. A. Boicea, “Energy storage technologies: The past and the present,” *Proceedings of the IEEE*, vol. 102, no. 11, pp. 1777–1794, Nov. 2014, doi: 10.1109/JPROC.2014.2359545.

[3] J. Morgan, “5/4/2018 A Simple Explanation Of ‘The Internet Of Things’ A Simple Explanation Of ‘The Internet Of Things,’” 2014. [Online]. Available: https://www.forbes.com/sites/jacobmorgan/2014/05/13/simple-explanation-internet-things-that-anyone-can-understand/#16de090d1d09

[4] V. Leonov, T. Torfs, R. J. M. Vullers, J. Su, and C. Van Hoof, “Renewable Energy Microsystems Integrated in Maintenance-Free Wearable and Textile-Based Devices: The Capabilities and Challenges.”

[5] J. Lv, J. Chen, and P. S. Lee, “Sustainable wearable energy storage devices self-charged by human-body bioenergy,” *SusMat*, vol. 1, no. 2, pp. 285–302, Jun. 2021, doi: 10.1002/sus2.14.

[6] F. R. Fan, W. Tang, and Z. L. Wang, “Flexible Nanogenerators for Energy Harvesting and Self-Powered Electronics,” Jun. 08, 2016, *Wiley-VCH Verlag*. doi: 10.1002/adma.201504299.

[7] F. R. Fan, Z. Q. Tian, and Z. Lin Wang, “Flexible triboelectric generator,” *Nano Energy*, vol. 1, no. 2, pp. 328–334, Mar. 2012, doi: 10.1016/J.NANOEN.2012.01.004.

[8] P. Munirathinam *et al.*, “A comprehensive review on triboelectric nanogenerators based on Real-Time applications in energy harvesting and Self-Powered sensing,” *Materials Science and Engineering: B*, vol. 297, Nov. 2023, doi: 10.1016/j.mseb.2023.116762.

[9] S. Bairagi, Shahid-ul-Islam, M. Shahadat, D. M. Mulvihill, and W. Ali, “Mechanical energy harvesting and self-powered electronic applications of textile-based piezoelectric nanogenerators: A systematic review,” Jun. 15, 2023, *Elsevier Ltd*. doi: 10.1016/j.nanoen.2023.108414.

[10] Z. L. Wang, “On the first principle theory of nanogenerators from Maxwell’s equations,” *Nano Energy*, vol. 68, p. 104272, Feb. 2020, doi: 10.1016/J.NANOEN.2019.104272.

[11] Z. L. Wang, “On Maxwell’s displacement current for energy and sensors: the origin of nanogenerators,” Mar. 01, 2017, *Elsevier B.V.* doi: 10.1016/j.mattod.2016.12.001.

[12] K. Dong, X. Peng, and Z. L. Wang, “Fiber/Fabric-Based Piezoelectric and Triboelectric Nanogenerators for Flexible/Stretchable and Wearable Electronics and Artificial Intelligence,” Feb. 01, 2020, *Wiley-VCH Verlag*. doi: 10.1002/adma.201902549.

[13] S. Spiegel, “Recent advances in applied polymer science,” Jun. 20, 2018, *John Wiley and Sons Inc*. doi: 10.1002/app.46279.

[14] C. Wu, A. C. Wang, W. Ding, H. Guo, and Z. L. Wang, “Triboelectric Nanogenerator: A Foundation of the Energy for the New Era,” Jan. 03, 2019, *Wiley-VCH Verlag*. doi: 10.1002/aenm.201802906.

[15] Z. L. Wang, “Triboelectric nanogenerators as new energy technology for self-powered systems and as active mechanical and chemical sensors,” Nov. 26, 2013. doi: 10.1021/nn404614z.

[16] X. S. Zhang, M. Han, B. Kim, J. F. Bao, J. Brugger, and H. Zhang, “All-in-one self-powered flexible microsystems based on triboelectric nanogenerators,” May 01, 2018, *Elsevier Ltd*. doi: 10.1016/j.nanoen.2018.02.046.

[17] S. Matsusaka, H. Maruyama, T. Matsuyama, and M. Ghadiri, “Triboelectric charging of powders: A review,” Nov. 15, 2010. doi: 10.1016/j.ces.2010.07.005.

[18] S. Niu and Z. L. Wang, “Theoretical systems of triboelectric nanogenerators,” *Nano Energy*, vol. 14, pp. 161–192, Oct. 2014, doi: 10.1016/j.nanoen.2014.11.034.

[19] S. Niu *et al.*, “Theoretical study of contact-mode triboelectric nanogenerators as an effective power source,” *Energy Environ Sci*, vol. 6, no. 12, pp. 3576–3583, Dec. 2013, doi: 10.1039/c3ee42571a.

[20] R. D. I. G. Dharmasena *et al.*, “Triboelectric nanogenerators: Providing a fundamental framework,” *Energy Environ Sci*, vol. 10, no. 8, pp. 1801–1811, Aug. 2017, doi: 10.1039/c7ee01139c.

[21] S. Niu *et al.*, “Theory of freestanding triboelectric-layer-based nanogenerators,” *Nano Energy*, vol. 12, pp. 760–774, Mar. 2015, doi: 10.1016/j.nanoen.2015.01.013.

[22] *2016 5th International Conference on Electronic Devices, Systems and Applications (ICEDSA) : December 6-8, 2016, American University of Ras Al Khaimah (AURAK), Ras Al Khaimah, UAE*. IEEE, 2016.

[23] Z. L. Wang and A. C. Wang, “On the origin of contact-electrification,” Nov. 01, 2019, *Elsevier B.V.* doi: 10.1016/j.mattod.2019.05.016.

[24] Y. Zhou, W. Deng, J. Xu, and J. Chen, “Engineering Materials at the Nanoscale for Triboelectric Nanogenerators,” Aug. 26, 2020, *Cell Press*. doi: 10.1016/j.xcrp.2020.100142.

[25] Y. Zi, S. Niu, J. Wang, Z. Wen, W. Tang, and Z. L. Wang, “Standards and figure-of-merits for quantifying the performance of triboelectric nanogenerators,” *Nat Commun*, vol. 6, Sep. 2015, doi: 10.1038/ncomms9376.

[26] J. Shao *et al.*, “Studying about applied force and the output performance of sliding-mode triboelectric nanogenerators,” *Nano Energy*, vol. 48, pp. 292–300, Jun. 2018, doi: 10.1016/j.nanoen.2018.03.067.

[27] C. Fang *et al.*, “Overview of Power Management for Triboelectric Nanogenerators,” *Advanced Intelligent Systems*, vol. 2, no. 2, Feb. 2020, doi: 10.1002/aisy.201900129.

[28] X. Zhang, L. Chen, Y. Jiang, W. Lim, and S. Soh, “Rationalizing the Triboelectric Series of Polymers,” *Chemistry of Materials*, vol. 31, no. 5, pp. 1473–1478, Mar. 2019, doi: 10.1021/acs.chemmater.8b04526.

[29] H. Zou *et al.*, “Quantifying the triboelectric series,” *Nat Commun*, vol. 10, no. 1, Dec. 2019, doi: 10.1038/s41467-019-09461-x.

[30] P. Tofel *et al.*, “Triboelectric Response of Electrospun Stratified PVDF and PA Structures,” *Nanomaterials*, vol. 12, no. 3, Feb. 2022, doi: 10.3390/nano12030349.

[31] Z. Zhao *et al.*, “Selection rules of triboelectric materials for direct-current triboelectric nanogenerator,” *Nat Commun*, vol. 12, no. 1, Dec. 2021, doi: 10.1038/s41467-021-25046-z.

[32] J. Liu, L. Gu, N. Cui, Q. Xu, Y. Qin, and R. Yang, “Fabric-Based Triboelectric Nanogenerators,” *Research*, vol. 2019, Jan. 2019, doi: 10.34133/2019/1091632.

[33] J. Luo and Z. L. Wang, “Recent progress of triboelectric nanogenerators: From fundamental theory to practical applications,” Dec. 01, 2020, *John Wiley and Sons Inc*. doi: 10.1002/eom2.12059.

[34] Z. L. Wang, J. Chen, and L. Lin, “Progress in triboelectric nanogenerators as a new energy technology and self-powered sensors,” 2015, *Royal Society of Chemistry*. doi: 10.1039/c5ee01532d.

[35] J. Shao *et al.*, “Quantifying the power output and structural figure-of-merits of triboelectric nanogenerators in a charging system starting from the Maxwell’s displacement current,” *Nano Energy*, vol. 59, pp. 380–389, May 2019, doi: 10.1016/j.nanoen.2019.02.051.

[36] J. Shao, T. Jiang, W. Tang, X. Chen, L. Xu, and Z. L. Wang, “Structural figure-of-merits of triboelectric nanogenerators at powering loads,” *Nano Energy*, vol. 51, pp. 688–697, Sep. 2018, doi: 10.1016/j.nanoen.2018.07.032.

[37] Z. Li, M. Zhu, Q. Qiu, J. Yu, and B. Ding, “Multilayered fiber-based triboelectric nanogenerator with high performance for biomechanical energy harvesting,” *Nano Energy*, vol. 53, pp. 726–733, Nov. 2018, doi: 10.1016/j.nanoen.2018.09.039.

[38] C. K. Chung, Y. J. Huang, T. K. Wang, and Y. L. Lo, “Fiber-Based Triboelectric Nanogenerator for Mechanical Energy Harvesting and Its Application to a Human–Machine Interface,” *Sensors*, vol. 22, no. 24, Dec. 2022, doi: 10.3390/s22249632.

[39] S. S. H. Abir, M. U. K. Sadaf, S. K. Saha, A. Touhami, K. Lozano, and M. J. Uddin, “Nanofiber-Based Substrate for a Triboelectric Nanogenerator: High-Performance Flexible Energy Fiber Mats,” *ACS Appl Mater Interfaces*, vol. 13, no. 50, pp. 60401–60412, Dec. 2021, doi: 10.1021/acsami.1c17964.

[40] X. Chen *et al.*, “A wave-shaped hybrid piezoelectric and triboelectric nanogenerator based on P(VDF-TrFE) nanofibers,” *Nanoscale*, vol. 9, no. 3, pp. 1263–1270, Jan. 2017, doi: 10.1039/c6nr07781a.

[41] T. Huang, C. Wang, H. Yu, H. Wang, Q. Zhang, and M. Zhu, “Human walking-driven wearable all-fiber triboelectric nanogenerator containing electrospun polyvinylidene fluoride piezoelectric nanofibers,” *Nano Energy*, vol. 14, pp. 226–235, Nov. 2014, doi: 10.1016/j.nanoen.2015.01.038.

[42] P. Cui, K. Parida, M. F. Lin, J. Xiong, G. Cai, and P. S. Lee, “Transparent, Flexible Cellulose Nanofibril–Phosphorene Hybrid Paper as Triboelectric Nanogenerator,” *Adv Mater Interfaces*, vol. 4, no. 22, Nov. 2017, doi: 10.1002/admi.201700651.

[43] V. Singh and B. Singh, “PDMS/PVDF- MoS2 based flexible triboelectric nanogenerator for mechanical energy harvesting,” *Polymer (Guildf)*, vol. 274, May 2023, doi: 10.1016/j.polymer.2023.125910.

[44] J. Zhu *et al.*, “The d-arched piezoelectric-triboelectric hybrid nanogenerator as a self-powered vibration sensor,” *Sens Actuators A Phys*, vol. 263, pp. 317–325, Aug. 2017, doi: 10.1016/j.sna.2017.06.012.

[45] H. H. Singh and N. Khare, “Improved performance of ferroelectric nanocomposite flexible film based triboelectric nanogenerator by controlling surface morphology, polarizability, and hydrophobicity,” *Energy*, vol. 178, pp. 765–771, Jul. 2019, doi: 10.1016/j.energy.2019.04.150.

[46] D. T. K. Ong *et al.*, “High performance composition-tailored PVDF triboelectric nanogenerator enabled by low temperature-induced phase transition,” *Nano Energy*, vol. 113, Aug. 2023, doi: 10.1016/j.nanoen.2023.108555.

[47] J. P. Lee, J. W. Lee, and J. M. Baik, “The progress of PVDF as a functional material for triboelectric nanogenerators and self-powered sensors,” Oct. 20, 2018, *MDPI AG*. doi: 10.3390/mi9100532.

[48] W. Gong *et al.*, “PVDF nanofibers for body-area triboelectric generators,” Dec. 01, 2024, *Elsevier Ltd*. doi: 10.1016/j.nanoen.2024.110277.

[49] M. M. Rastegardoost, O. A. Tafreshi, Z. Saadatnia, S. Ghaffari-Mosanenzadeh, C. B. Park, and H. E. Naguib, “Porous PVDF mats with significantly enhanced dielectric properties and novel dipole arrangement for high-performance

triboelectric nanogenerators," *Appl Mater Today*, vol. 30, Feb. 2023, doi: 10.1016/j.apmt.2023.101732.

[50] T. Subbiah, G. S. Bhat, R. W. Tock, S. Parameswaran, and S. S. Ramkumar, "Electrospinning of nanofibers," *J Appl Polym Sci*, vol. 96, no. 2, pp. 557–569, Apr. 2005, doi: 10.1002/app.21481.

[51] S. Agarwal, J. H. Wendorff, and A. Greiner, "Use of electrospinning technique for biomedical applications," Dec. 08, 2008, *Elsevier BV*. doi: 10.1016/j.polymer.2008.09.014.

[52] B. Zhang, W. Wang, M. Tian, N. Ning, and L. Zhang, "Preparation of aramid nanofiber and its application in polymer reinforcement: A review," Oct. 05, 2020, *Elsevier Ltd*. doi: 10.1016/j.eurpolymj.2020.109996.

[53] A. He *et al.*, "Advanced Aramid Fibrous Materials: Fundamentals, Advances, and Beyond," Feb. 01, 2024, *Springer*. doi: 10.1007/s42765-023-00332-1.

[54] M. de Magistris and G. Miano, "Circuiti a-dinamici lineari," in *Circuiti*, Springer Milan, 2016, pp. 159–212. doi: 10.1007/978-88-470-5770-8_4.

[55] C. K. . Alexander and M. N. O. . Sadiku, *Fundamentals of electric circuits*. McGraw-hill Education, 2017.

[56] P. C. Sen, "Electric Motor Drives and Control-Past, Present, and Future," 1990.

[57] "DIODE BRIDGE RECTIFIER".

[58] J. Huang, Y. Hao, M. Zhao, W. Li, F. Huang, and Q. Wei, "All-Fiber-Structured Triboelectric Nanogenerator via One-Pot Electrospinning for Self-Powered Wearable Sensors," *ACS Applied Materials and Interfaces* , vol. 13, no. 21, pp. 24774–24784, Jun. 2021, doi: 10.1021/acsami.1c03894.

[59] N. Capitello RELATORE and P. Tenti, "FACOLTÀ DI INGEGNERIA LAUREA TRIENNALE IN INGEGNERIA MECCATRONICA SUPERCONDENSATORI Tecnologie e applicazioni".